

# Baryonic Distributions in Galaxy Dark Matter Haloes I: New Observations of Neutral and Ionized Gas Kinematics

Emily E. Richards,<sup>1\*</sup> L. van Zee,<sup>1†</sup> K. L. Barnes,<sup>1</sup> S. Staudaher,<sup>2</sup> D. A. Dale,<sup>2</sup> T. T. Braun,<sup>1</sup> D. C. Wavle,<sup>1</sup> J. J. Dalcanton,<sup>3</sup> J. S. Bullock<sup>4</sup> and R. Chandar<sup>5</sup>

<sup>1</sup>*Indiana University, 727 East 3rd Street, Swain West 318, Bloomington, IN 47405, USA*

<sup>2</sup>*University of Wyoming, 1000 E. University, Dept 3905, Laramie, WY 82071, USA*

<sup>3</sup>*University of Washington, Box 351580, U.W., Seattle, WA 98195, USA*

<sup>4</sup>*University of California, Irvine, Department of Physics & Astronomy, 4129 Frederick Reines Hall, Irvine, CA 92697, USA*

<sup>5</sup>*University of Toledo, 2801 West Bancroft Street, Toledo, OH 43606, USA*

Accepted XXX. Received YYY; in original form ZZZ

## ABSTRACT

We present a combination of new and archival neutral hydrogen (HI) observations and new ionized gas spectroscopic observations for sixteen galaxies in the statistically representative EDGES kinematic sample. HI rotation curves are derived from new and archival radio synthesis observations from the Very Large Array (VLA) as well as processed data products from the Westerbork Radio Synthesis Telescope (WSRT). The HI rotation curves are supplemented with optical spectroscopic integral field unit (IFU) observations using SparsePak on the WIYN 3.5 m telescope to constrain the central ionized gas kinematics in twelve galaxies. The full rotation curves of each galaxy are decomposed into baryonic and dark matter halo components using  $3.6\mu\text{m}$  images from the *Spitzer Space Telescope* for the stellar content, the neutral hydrogen data for the atomic gas component, and, when available, CO data from the literature for the molecular gas component. Differences in the inferred distribution of mass are illustrated under fixed stellar mass-to-light ratio (M/L) and maximum disc/bulge assumptions in the rotation curve decomposition.

**Key words:** galaxies: kinematics and dynamics – galaxies: structure

## 1 INTRODUCTION

The past three decades have led to many advances in our understanding of galaxy rotation curves and a staggering accumulation of observational data. Radio synthesis observations of the 21 cm line of neutral hydrogen have historically been and continue to be the primary method for tracing the outer gravitational potential of galaxies (e.g. Bosma 1981b; Begeman et al. 1991; Broeils 1992; Sanders 1996; Verheijen & Sancisi 2001; Walter et al. 2008; van der Hulst et al. 2001; McGaugh 2012). The advent of integral field spectroscopic (IFS) data has further improved our ability to measure galaxy kinematics, especially in the central regions (e.g. Cappellari et al. 2011; Bundy et al. 2015; García-Lorenzo et al. 2015). Using galaxy kinematics to decompose the rotation curves has long been a primary method for investigating the mass components of galaxies (e.g. Bosma 1978; Rubin et al. 1982; Persic et al. 1996). The dynamically inferred missing matter from these

early observations is now part of the  $\Lambda$ CDM cosmology, which provides a strong framework within which one can trace the evolution of small perturbations in the early universe to the diverse range of morphological types found in nearby galaxies (e.g. Springel et al. 2006; Martig et al. 2012; Aumer & White 2013).

Although progress is being made in producing realistic galaxies at  $z = 0$  in  $\Lambda$ CDM simulations (e.g. Crain et al. 2015), well known tensions between the models and observations still exist. For example, there is a persistent discrepancy between the diversity of rotation curves in observed galaxies for a given maximum rotation velocity,  $V_{\text{max}}$ , and the little variation seen in simulated galaxies with the same  $V_{\text{max}}$ . Low mass dwarf galaxies, in particular, typically have much lower circular velocities in the inner regions than expected from  $\Lambda$ CDM, leading to a significant mass deficit (Oman et al. 2015). Rotation curve decomposition analysis continues to be a powerful observational tool for constraining theoretical predictions of the distribution of mass on galaxy scales.

Despite the mountain of kinematic observations, there are still challenges in constraining and interpreting the dis-

\* E-mail: er7@indiana.edu

† E-mail: lvanee@indiana.edu

tributions of mass components in galaxies. The stellar mass, in particular, is difficult to estimate due to uncertainties in mass-to-light ratio (M/L) leading to the use of maximum disc fits to rotation curves (van Albada & Sancisi 1986) despite evidence which suggests discs are submaximal (e.g. Courteau & Rix 1999; Bershadsky et al. 2011). Much attention has been given to determining the stellar M/L so that the degeneracy between the scaling of the stellar contribution and dark matter halo model in rotation curve decomposition analysis may be broken. There is relatively good consensus among different methods estimating the stellar M/L at  $3.6\mu\text{m}$ , which suggest a M/L of about 0.5 (e.g. Eskew et al. 2012; McGaugh & Schombert 2015a; Lelli et al. 2016). Estimates of the stellar M/L in the K-band result in a larger range of values between  $\sim 0.3$ - $0.6$ , depending on the method used (e.g. den Heijer et al. 2015; Martinsson et al. 2013; Just et al. 2015). Even with constraints on the stellar M/L, uncertainties in the distance estimates still hinder our ability to accurately resolve the true baryonic contribution in the context of rotation curve decomposition analysis (see Section 2.1).

These challenges can cause considerable uncertainties in the results of individual galaxies. Therefore, it is ideal to interpret such results in the context of a larger statistical sample. We utilize a statistical sample of about 40 nearby galaxies defined from the Extended Disk Galaxy Explore Science (EDGES) Survey (van Zee et al. 2012) in an effort to investigate the distribution of mass in galaxies in the context of galaxy formation and evolution. Data for the EDGES Survey includes deep  $3.6\mu\text{m}$  observations from the *Spitzer Space Telescope* of 92 galaxies spanning a wide range of morphology (S0 to Im), luminosity ( $-14 > M_B > -21$ ) and environment (cluster, group and isolated). Galaxies in EDGES were selected to have distances between 2 – 20 Mpc and include the Ursa Major cluster, but exclude Virgo. We have defined a kinematic sub-sample from EDGES which includes all galaxies that have intermediate inclination angles (between  $30^\circ$  and  $68^\circ$ ) estimated from optical axial ratios so that both accurate rotation curves and surface density profiles may be determined. The complete kinematic sample preserves the unbiased representative nature of the full EDGES sample allowing us to investigate correlations between the distribution of baryonic and non-baryonic matter in a statistical manner.

In this study, we are presenting galaxies in the kinematic sample for which we have new HI radio synthesis observations from the VLA and new ionized gas kinematics from the SparsePak IFU on the WIYN 3.5 m telescope. The observational data products are discussed in Section 2. Rotation curve decomposition results are shown in Section 3. Section 4 provides a discussion of the main results which are summarized in Section 5. Finally, notes on the individual galaxies are provided in Appendix A.

## 2 OBSERVATIONAL DATA

In this paper, we present new and archival HI synthesis observations and new spectroscopic IFU observations from SparsePak on the WIYN 3.5 m telescope to constrain the neutral and ionized gas kinematics in sixteen galaxies. We use additional multiwavelength observations to probe the

stellar and gas content, including deep near-infrared (NIR) images taken at  $3.6\mu\text{m}$  from the *Spitzer Space Telescope* to trace the extended stellar populations. Moderate depth optical broadband *B* and *R* and narrowband H $\alpha$  provide information about the dominant stellar populations and star formation activity. Finally, archival molecular gas observations complement the HI to better estimate the total gas content in the galaxies. Tables 1, 2 and 3 provide a summary of observed, corrected and radial properties derived from this multifrequency dataset. All reported magnitudes are calculated using the Vega system. A discussion of distance estimates used in the present study is given below in addition to brief summaries of the data acquisition and processing.

### 2.1 Distance Estimates

Many of the forthcoming results, including the primary results from the mass decomposition analysis, depend on the adopted distance to each galaxy. For the mass decomposition, an accurate determination of the total baryon content in galaxies requires an accurate distance so that the mass surface densities are scaled correctly when they are converted into circular rotational velocities. Uncertainty in the distance is often absorbed into the uncertainty of the stellar M/L, particularly for more massive galaxies where the total baryon mass is dominated by the stellar component. In order to be able to compare the distribution of mass in galaxies at fixed stellar M/L, we must rely on relatively accurate distance estimates to remove at least some of this uncertainty.

For nearby galaxies, we cannot rely on Hubble flow distance estimates, as their peculiar velocities may be large relative to their systemic velocities. Therefore, we are limited to using independent distance estimates derived from methods such as Type Ia supernovae (SNIa) and surface brightness fluctuations (SBF). Six galaxies in the present study have distance estimates from these more robust independent methods (see Table 2). For the remaining 10 galaxies we adopt the Luminous Tully-Fisher Relation (LTFR) from McGaugh & Schombert (2015b), so that the galaxies are on a consistent distance scale. The sample from which the LTFR was derived is a better match to the kinematic sample than other Tully-Fisher samples (e.g. Sorce et al. 2014). It also does not introduce as much circularity into the analysis as the baryonic Tully-Fisher relation (BTFR; McGaugh et al. 2000) since it uses luminosity at  $3.6\mu\text{m}$  (Section 2.5) rather than baryonic mass and is, therefore, independent of stellar M/L.

Fig. 1 shows the LTFR for this sample along with the placement of the independent and Hubble flow distance estimates for comparison. The mean offset is  $\sim 0.3$  dex with the largest differences between distance estimates being on the order of  $\sim 0.6$ - $0.7$  dex for NGC 3998 and NGC 3992. This is likely due to the greatest limitation of the LTFR distance estimates, which is the ability to define  $V_{\text{flat}}$ . In general,  $V_{\text{flat}}$  was chosen from an intermediate to outer radial range free from warps (Section 3.1).  $V_{\text{flat}}$  was additionally calculated following the method of Lelli et al. (2016) which uses a simple automated algorithm to calculate the mean of the outermost rotation curve points until it is no longer flat to within  $\sim 5\%$ . The  $V_{\text{flat}}$  values calculated in this manner are

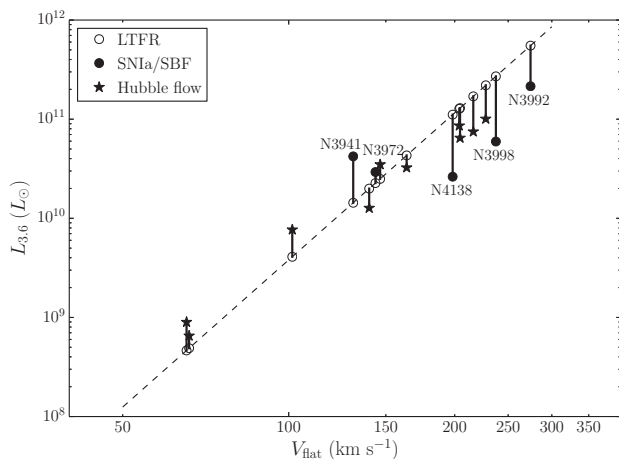


**Figure 1.** Luminous Tully-Fisher Relation at  $3.6\mu\text{m}$  from McGaugh & Schombert (2015b) (dashed line) used to define distances to galaxies in the present sample with no independent distance estimate from the literature (see text for details). Open circles indicate where the galaxies in this sample lie on the LTFR (with the exception of UGC 07639) given their estimated  $V_{\text{flat}}$ . The filled circles show where the galaxies with independent distance estimates from the literature would lie on this plot using their SNIa (NGC 3972 and NGC 3992) or SBF (NGC 3941, NGC 3998 and NGC 4138) distances. Filled stars show where the Hubble flow distances would lie for comparison.

in excellent agreement with the estimated values reported in Table 2, except for the cases of NGC 3941, NGC 3992 and NGC 5055 where we have chosen to adopt a more interior value for  $V_{\text{flat}}$  to avoid the influence of possible warps. An accurate rotation curve was not able to be derived from UGC 07639 (see Section A12), so it is not included in Fig. 1. It is important to note that the galaxies which show the largest discrepancy between the two distance estimates are the galaxies which have the most trustworthy independent distances and the least trustworthy determinations of  $V_{\text{flat}}$ .

## 2.2 New and Archival HI Observations

Radio synthesis observations using the 21 cm line of HI were obtained with the VLA<sup>1</sup> in C configuration in 2013 July - September for eight galaxies in the kinematic sample of the EDGES survey. All eight galaxies targeted for new observations either did not have archival HI synthesis observations or the existing data were not adequate for rotation curve decomposition analysis. A complete analysis of one of these galaxies, NGC 5005, is published in Richards et al. (2015). In the current study, we present the new HI data for the seven remaining galaxies.

The VLA data had an initial frequency resolution of  $7.8125 \text{ kHz channel}^{-1}$  ( $1.65 \text{ km s}^{-1} \text{ channel}^{-1}$ ). The standard flux calibrator 3C286 was observed at least once during every observing block, and a phase calibrator was observed approximately every 40 minutes, so that the data may be

flux and phase calibrated. Galaxies were scheduled in one, two, or four hour observing blocks during nighttime or early evening.

The data were loaded into AIPS<sup>2</sup> and processed following the methods outlined in Richards et al. (2015). Solar RFI was flagged on all channels simultaneously, but was mostly not a problem. Three data cubes were created for each galaxy with different Robust weighting parameters for varying spatial resolution and a channel averaging of 3 for a resulting velocity resolution of  $\sim 5 \text{ km s}^{-1} \text{ channel}^{-1}$ . When necessary, a lower velocity resolution cube ( $15 \text{ km s}^{-1} \text{ channel}^{-1}$ ) was created to probe the lowest column density of HI gas. Synthesis imaging parameters for the relevant datacubes for each galaxy are presented in Table 4. NGC 4389, UGC 07639, and UGC 08839 each had one hour blocks that were discarded due to RFI issues. The time on source given in Table 4 does not include these blocks. Many of the galaxies' observing blocks were scheduled at similar local sidereal times on different nights resulting in a beam that is not round. This is especially true for NGC 5608.

In addition to the new VLA observations, eight of the galaxies for which we acquired ionized gas kinematics (see Section 2.3) have archival HI observations adequate for rotation curve decomposition analysis. We used the processed data products from the Westerbork Survey of HI in Spiral Galaxies (WHISP; van der Hulst et al. 2001) for the galaxies NGC 3726 and NGC 4051. We also used processed data for NGC 4138, which is published in Jore et al. (1996). We pulled NGC 3675, NGC 3953, NGC 3992, NGC 5033, and NGC 5055 from the VLA archive and processed following standard practice. All except NGC 3992 were processed in AIPS. Since NGC 3992 was observed during the EVLA transition, the observations were processed in CASA (McMullin et al. 2007). As is evident in Fig. A5, the bandpass of the archival VLA data was not large enough to encompass the full frequency range of HI emission in NGC 3953. Processed data for NGC 3953 is available from WHISP, but the observations are low signal-to-noise (S/N) due to the fact that NGC 3953 is detected outside WSRT's primary beam half-power width. The kinematics were easier to constrain in the complete half of the archival VLA data than in the low S/N WHISP data (see Section A5 for more detail).

<sup>1</sup> The Very Large Array is operated by the National Radio Astronomy Observatory, which is a facility of the National Science Foundation operated under cooperative agreement by Associated Universities, Inc.

<sup>2</sup> The Astronomical Image Processing System (AIPS) has been developed by the NRAO.

**Table 1.** Observed Properties

Galaxy	Morphological <sup>a</sup> Type	$m_B$	$m_R$	$m_{3.6}$	$\log_{10}(\text{H}\alpha \text{ flux})$ (erg s <sup>-1</sup> cm <sup>-2</sup> )	Equivalent Width (Å)	HI flux (Jy km s <sup>-1</sup> )	$W_{20}$ (km s <sup>-1</sup> )	CO flux <sup>b</sup> (Jy km s <sup>-1</sup> )	CO flux <sup>c</sup> Reference
NGC 3486	SABc	11.14±0.03	10.20±0.03	7.67±0.01	-11.16±0.31	38.2±3.3	147±29	268	57±1	1
NGC 3675	SAB	11.04±0.02	9.57±0.02	6.50±0.01	-11.49±0.14	8.62±0.44	57.9±11.6	442	1440±280	2
NGC 3726	SABc	11.11±0.02	10.02±0.02	7.44±0.01	-11.25±0.13	23.8±0.9	90.6±18.1	288	720±180	2,3
NGC 3941	SB0	11.45±0.02	9.97±0.02	7.18±0.01	-12.26±0.06	1.93±0.05	14.3±2.9	285	–	4
NGC 3953	SBbc	11.08±0.02	9.71±0.02	6.73±0.01	-11.20±0.03	8.76±0.20	39.3±0.8 <sup>d</sup>	442 <sup>d</sup>	1790±450	2,3
NGC 3972	SABc	13.14±0.02	11.94±0.02	9.17±0.02	-12.16±0.13	17.2±0.8	16.3±3.3	283	...	...
NGC 3992	SBbc	10.94±0.02	9.57±0.02	6.77±0.01	-11.45±0.12	9.87±0.22	75.5±15.1	484	–	3
NGC 3998	SA0	11.64±0.02	10.09±0.02	7.16±0.01	-11.88±0.07	6.29±0.25	8.85±1.77	592	–	4
NGC 4051	SABbc	11.08±0.02	9.94±0.02	7.07±0.01	-11.18±0.09	27.1±1.4	39.4±7.9	265	740±140	2,3
NGC 4138	SA0	12.29±0.02	10.82±0.02	7.96±0.01	-11.93±0.09	9.05±0.36	20.6±0.3 <sup>e</sup>	340 <sup>e</sup>	100±30	2
NGC 4389	SBbc	12.64±0.02	11.46±0.02	8.77±0.02	-11.82±0.06	24.7±0.5	6.96±1.39	192	...	...
UGC 07639	Im	14.32±0.02	13.44±0.02	11.42±0.05	-13.36±0.14	4.10±0.25	2.54±0.51	66.4	...	...
NGC 5033	SAC	11.01±0.02	9.73±0.02	6.60±0.01	-11.17±0.11	21.3±0.5	213±43	489	2469±258	3
NGC 5055	SABc	9.44±0.02	8.14±0.02	5.36±0.01	-10.67±0.12	15.6±0.8	454±91	407	3812±276	3
UGC 08839	Im	16.04±0.02	15.21±0.02	13.19±0.10	-13.61±0.18	11.4±1.1	26.9±5.4	117	...	...
NGC 5608	Im	13.96±0.02	13.23±0.02	11.23±0.04	-12.56±0.16	22.2±1.5	12.6±2.5	131	...	...

*Note.* – The apparent magnitudes are measured values and are not corrected for extinction. The reported apparent magnitudes and  $\log_{10}(\text{H}\alpha \text{ flux})$  are measured within  $R_{25}$ .

<sup>a</sup> RC3; de Vaucouleurs et al. (1991)

<sup>b</sup> – not detected; ... not observed

<sup>c</sup> CO flux references: (1) CARMA STING (Rui Xue, private communication); (2) FCRAO (Young et al. 1995); (3) BIMA SONG (Helfer et al. 2003); (4) ATLAS<sup>3D</sup> (Young et al. 2011)

<sup>d</sup> Integrated HI flux and  $W_{20}$  values from Verheijen & Sancisi (2001).

<sup>e</sup> Integrated HI flux and  $W_{20}$  values from Jore et al. (1996).

**Table 2.** Distance and Extinction Corrected Properties

Galaxy	$V_{\text{flat}}$ (km s <sup>-1</sup> )	Distance (Mpc)	Distance <sup>a</sup> Reference	$A_B$ <sup>b</sup>	$M_B$	$(B-R)_0$	$(B-3.6)_0$	$(R-3.6)_0$	SFR <sup>c</sup> (M <sub>☉</sub> yr <sup>-1</sup> )	Total Stellar <sup>d</sup> Mass (10 <sup>9</sup> M <sub>☉</sub> )	Total HI Mass (10 <sup>9</sup> M <sub>☉</sub> )	Total H <sub>2</sub> Mass (10 <sup>9</sup> M <sub>☉</sub> )
NGC 3486	139.9	10.6	1	0.078	-19.16±0.03	0.91±0.04	3.39±0.03	2.48±0.03	0.50±0.36	9.94±1.99	3.90±0.78	0.05±0.001
NGC 3675	204.5	15.3	1	0.071	-20.10±0.02	1.44±0.03	4.47±0.02	3.03±0.02	0.49±0.16	64.9±13.0	3.19±0.64	2.64±0.51
NGC 3726	146.5	10.5	1	0.060	-19.13±0.02	1.07±0.03	3.61±0.02	2.54±0.02	0.40±0.12	12.5±2.5	2.35±0.47	0.62±0.16
NGC 3941	130.9	12.2	2	0.076	-19.14±0.02	1.45±0.03	4.19±0.02	2.74±0.02	0.05±0.007	21.1±4.2	0.50±0.10	–
NGC 3953	227.7	22.7	1	0.109	-20.88±0.02	1.33±0.03	4.24±0.02	2.92±0.02	2.1±0.1	109±22	4.77±0.95	7.24±1.82
NGC 3972	143.7	25.2	3	0.051	-19.02±0.02	1.18±0.03	3.92±0.03	2.74±0.03	0.28±0.08	14.6±2.9	2.44±0.49	–
NGC 3992	274.5	22.7	4	0.106	-21.04±0.02	1.33±0.03	4.06±0.02	2.74±0.02	1.2±0.3	107±21	9.17±1.83	–
NGC 3998	237.5	14.1	2	0.059	-19.40±0.02	1.53±0.03	4.42±0.02	2.89±0.02	0.17±0.03	29.7±5.9	0.41±0.08	–
NGC 4051	163.6	11.7	1	0.047	-19.39±0.02	1.12±0.03	3.96±0.02	2.84±0.02	0.58±0.12	21.6±4.3	1.27±0.25	0.79±0.15
NGC 4138	198.3	13.8	2	0.051	-18.54±0.02	1.45±0.03	4.28±0.02	2.83±0.02	0.14±0.03	13.1±2.6	0.92±0.18	0.15±0.04
NGC 4389	101.5	7.7	1	0.053	-17.00±0.02	1.16±0.03	3.82±0.03	2.66±0.03	0.06±0.01	2.03±0.41	0.10±0.02	–
UGC 07639	19.2	7.1	5	0.042	-15.34±0.02	0.86±0.03	2.86±0.05	1.99±0.05	0.001±0.0005	0.22±0.04	0.03±0.01	–
NGC 5033	216.1	18.8	1	0.042	-20.56±0.02	1.26±0.03	4.37±0.02	3.11±0.02	1.5±0.4	84.6±16.9	17.7±3.5	6.85±0.72
NGC 5055	203.9	9.1	1	0.064	-20.60±0.02	1.27±0.03	4.02±0.02	2.74±0.02	1.1±0.3	63.2±12.6	8.86±1.77	2.48±0.18
UGC 08839	66.0	11.1	1	0.090	-15.68±0.02	0.79±0.03	2.76±0.10	1.97±0.10	0.002±0.001	0.25±0.05	0.78±0.16	–
NGC 5608	65.3	7.5	1	0.034	-15.75±0.02	0.72±0.03	2.70±0.04	1.98±0.04	0.01±0.004	0.23±0.05	0.17±0.03	–

*Note.* –  $M_B$  and colours are extinction corrected. The extinction correction for the NIR is assumed to be negligible. The  $M_B$  value also includes a small correction based on an extrapolation of the observed stellar disc. Colours are measured within  $R_{25}$ .

<sup>a</sup> Distance references: (1) Distances determined using the LTFR at 3.6 $\mu$ m from [McGaugh & Schombert \(2015b\)](#):  $\log_{10} L_{3.6} = (-0.28 \pm 0.36) + (4.93 \pm 0.17) \log_{10} V_{\text{flat}}$ . (2) SBF ([Tonry et al. 2001](#)); (3) SNIa ([Maguire et al. 2012](#)); (4) SNIa ([Parodi et al. 2000](#)); (5) SBF ([Rekola et al. 2005](#))

<sup>b</sup> As calculated by [Schlafly & Finkbeiner \(2011\)](#).

<sup>c</sup> Measured within  $R_{25}$  and calculated using the calibration given in [Kennicutt & Evans \(2012\)](#).

<sup>d</sup> Calculated using  $M/L_{3.6} = 0.5 \pm 0.1$ .



### 2.3 WIYN SparsePak

Many of the large barred spiral galaxies in the kinematic sample lack detectable neutral hydrogen in their centres (e.g. NGC 3992; Fig. A7). This is likely caused by a phase change from atomic to molecular gas or bar-driven transport of gas to the centre where it is concentrated, and in some cases, consumed by nuclear star formation (Sheth et al. 2005). The desire to recover kinematic information in the centres of such galaxies motivated us to acquire optical IFS observations of the ionized gas. Further, even the non-barred galaxies which have detectable HI in their centres benefit from the improved spatial resolution that the IFS data provide. Thus, the only galaxies not targeted for SparsePak observations are irregular type galaxies which have little or no ionized gas emission visible in the narrowband H $\alpha$  images.

We present ionized gas velocity fields for the central regions of twelve galaxies obtained using the SparsePak IFU (Bershady et al. 2004) on the WIYN 3.5 m telescope in 2014 April, 2015 March, and 2015 April. The SparsePak IFU is composed of eighty-two 5'' diameter fibers arranged in a fixed 70''  $\times$  70'' square. Observations were acquired using the same setup as described in Richards et al. (2015) with a wavelength range from 6480 Å to 6890 Å and a resulting velocity resolution of 13.9 km s<sup>-1</sup> pixel<sup>-1</sup>. Typical integration times ranged from 3 $\times$ 480s for galaxies dominated by bright star forming regions to 3 $\times$ 1200s for galaxies dominated by diffuse ionized gas.

As discussed in Richards et al. (2015), the SparsePak array was aligned on the sky with a position angle of 0° for simplicity and consistency between galaxies. We used a three pointing dither pattern to spatially fill in gaps between fibers. We took three exposures for each dither pointing to be able to detect faint diffuse ionized gas, not just bright star forming regions. We used additional pointings when necessary to cover the full extent of the central regions on the sky. NGC 3992 required three separate pointings with dithers and NGC 5055 required two. Observations of blank sky were also taken to remove sky line contamination more accurately, as all of the galaxies are much more extended than the SparsePak field-of-view (See Fig. 2).

The SparsePak data were processed using standard tasks in the HYDRA package within IRAF<sup>3</sup> following the same procedure as described in Richards et al. (2015). The data were bias-subtracted and flattened, and the IRAF task DOHYDRA was used to fit and extract apertures from the IFU data. The spectra were wavelength calibrated using a wavelength solution created from ThAr lamp observations. The three exposures for each dither pointing were cleaned of cosmic rays. The individual images were sky subtracted using a separate sky pointing scaled to the strength of the 6577 Å sky line, which is close to the redshifted H $\alpha$  and [NII]  $\lambda$ 6584 lines in some fibers. The cleaned, sky subtracted images were averaged together to increase S/N and then flux calibrated using observations of spectrophotometric standards from Oke (1990). Although the skies were merely transparent, not photometric, we apply a flux calibration to

remove instrumental signatures and to permit measurement of relative line strengths.

Relative line strengths of [NII]  $\lambda$ 6584 to H $\alpha$  were measured from Gaussian fits to the emission lines for the central fiber's spectrum and integrated spectrum for each galaxy to reveal the nature of the dominant ionizing source. The integrated spectrum for each galaxy was corrected for rotation using the Doppler shift of the centroid of the H $\alpha$  emission line in each galaxy's spectra. With the exception of the S0 galaxies NGC 3941 and NGC 3998, the integrated spectra show [NII]  $\lambda$ 6584/H $\alpha$  values with a median of 0.5, indicative of thermal emission processes most likely due to star formation activity (Baldwin et al. 1981). We additionally find relatively narrow full width half maximum (FWHM) values on the order of 80 km s<sup>-1</sup> for these integrated spectra. All of the galaxies presented in this study with the exception of NGC 3726, NGC 4051, NGC 4389 and NGC 5055 show large [NII]  $\lambda$ 6584/H $\alpha$  values, ranging between 2 and 4.5, as well as broad FWHM values on the order of 100-350 km s<sup>-1</sup> in the spectra of their central fibers. This is not unexpected given that NGC 3486, NGC 3941, NGC 4051, NGC 4138 and NGC 5033 are classified as Seyferts, NGC 3675, NGC 3953, NGC 3992 and NGC 5055 have been classified as transition objects, and NGC 3998 is classified as low-ionization nuclear emission-line region (LINER) by Ho et al. (1997).

The flux calibrated, sky subtracted spectra were cross-correlated with a template emission line spectrum to extract the luminosity weighted mean recessional velocity at every position using the IRAF task FXCOR. To minimize systematic effects, the cross-correlation analysis uses a high S/N template spectrum from within each galaxy. This results in robust measures of the relative velocity offset for each fiber. Spectra with broad or double-peaked emission line profiles resulted in broad cross-correlation peaks that were nonetheless of high significance and had a well-defined centroid. The velocity values from FXCOR were then placed into a grid that mapped the SparsePak fiber locations. To fill in the missing spacings, the velocity field was then interpolated using the average value from the nearest eight pixels. Fig. 3 displays the resulting ionized gas velocity fields for the twelve galaxies.

### 2.4 Archival CO

When available, archival molecular gas observations of CO are used to supplement the HI surface density measurements. Archival CO data from the BIMA Survey of Nearby Galaxies (BIMA SONG; Helfer et al. 2003) were acquired to supplement the HI observations of NGC 5033 and NGC 5055. The BIMA SONG CO intensity maps have a typical spatial resolution of about 6.0 arcsec and are mapped in red contours in Figs. A13 and A14. More detailed maps can be found in Helfer et al. (2003). NGC 3992 is in BIMA SONG, but was not detected in CO line emission. It was formally detected in one pointing with the KPNO 12 m, but the molecular gas component for NGC 3992 is not included in the present study due to lack of information about the spatial distribution. Surface density measurements from the FCRAO Extragalactic CO Survey (Young et al. 1995) were used to estimate the molecular gas distribution in NGC 3675, NGC 3726, NGC 3953, NGC 4051 and NGC 4138. A CO intensity map of NGC 3486 was ac-

<sup>3</sup> IRAF is distributed by NOAO, which is operated by the Association of Universities for Research in Astronomy, Inc., under cooperative agreement with the National Science Foundation.

**Table 3.** Radial Properties

Galaxy	$h_R^a$		$D_{25}^b$		$D_{HI}^c$		$C_{28}^d$	$\log_{10}(\text{EW})$ gradient	$(B - R)$ gradient
	(arcsec)	(kpc)	(arcsec)	(kpc)	(arcsec)	(kpc)		(arcmin $^{-1}$ )	(arcmin $^{-1}$ )
NGC 3486	39.0	2.00	371	19.1	640	32.9	3.6	-0.15	-0.19
NGC 3675	54.1	4.01	346	25.7	600	44.5	3.9	-0.37	-0.01
NGC 3726	38.8	1.98	351	17.8	511	26.0	2.3	0.22	-0.12
NGC 3941	25.4	1.50	184	10.9	408	24.1	4.8	-0.15	-0.05
NGC 3953	39.1	4.30	371	40.9	400 <sup>e</sup>	44.0	3.4	-0.06	-0.09
NGC 3972	25.0	3.05	202	24.7	216	26.4	4.4	-0.15	-0.24
NGC 3992	47.6	5.24	411	45.3	705	77.6	2.9	0.02	-0.05
NGC 3998	35.9	2.45	180	12.3	282	19.3	5.9	-0.24	-0.16
NGC 4051	39.7	2.25	314	17.8	271	15.3	5.8	-0.18	0.02
NGC 4138	21.6	1.45	157	10.5	258	17.3	4.5	-1.41	0.08
NGC 4389	21.7	0.81	149	5.58	153	5.71	2.2	-0.90	0.04
UGC 07639	29.8	1.03	118	4.06	105	3.61	3.5	-2.35	0.38
NGC 5033	61.4	5.60	541	49.3	960	87.5	5.6	0.10	-0.22
NGC 5055	110	4.85	805	35.5	1950	86.0	4.3	-0.07	-0.02
UGC 08839	34.1	1.84	68.4	3.68	340	18.3	3.2	-0.26	-0.14
NGC 5608	22.1	0.80	142	5.18	201	7.31	3.0	0.62	-0.35

<sup>a</sup> Total average disc scale length measured at  $3.6\mu\text{m}$ .<sup>b</sup> Measured at 25 mag arcsec $^{-2}$  in  $B$ .<sup>c</sup> Measured at  $10^{20}$  atoms cm $^{-2}$ .<sup>d</sup> Calculated as  $5\log_{10}(R_{80}/R_{20})$ , where  $R_{20}$  is the radius which contains 20 per cent and  $R_{80}$  is the radius which contains 80 per cent of the total luminosity as measured from ellipse photometry (e.g. [Kent 1985](#)).<sup>e</sup> From [Verheijen & Sancisi \(2001\)](#).**Table 4.** HI Synthesis Image Parameters

Galaxy	Telescope/ Project Code	Time On Source (hours)	Image Name	Velocity Resolution (km s $^{-1}$ )	Robust Weighting	Beam Size (arcsec)	Beam Position Angle (deg)	Noise (mJy beam $^{-1}$ )
NGC 3486	VLA	6.6	low	5.0	5	25.5 $\times$ 17.7	55.8	0.47
	13A-107		high	5.0	-0.5	16.4 $\times$ 13.4	71.5	0.65
NGC 3675	VLA	5.1	medium	10.3	0.5	21.2 $\times$ 18.1	83.3	0.53
	AP225		high	10.3	-0.5	16.1 $\times$ 14.4	84.4	0.64
NGC 3726	WSRT	12.0	30'' smooth	4.1	–	30.0 $\times$ 30.0	0.0	3.83
	WHISP		full res.	4.1	–	15.8 $\times$ 11.8	0.0	3.07
NGC 3941	VLA	6.5	low	5.0	5	21.9 $\times$ 18.6	58.2	0.46
	13A-107		medium	5.0	0.5	17.6 $\times$ 15.2	71.8	0.51
NGC 3953	VLA	1.2	medium	5.2	0.5	49.9 $\times$ 47.1	-68.5	1.31
	AV237		high	5.2	-0.5	44.3 $\times$ 42.6	-72.7	1.44
NGC 3992	VLA	5.1	low	3.3	5	32.3 $\times$ 17.5	107	0.94
	10B-207		high	3.3	-0.5	20.2 $\times$ 12.7	89.2	1.33
NGC 3998/	VLA	6.7	spectral binned	14.9	5	31.0 $\times$ 21.0	68.9	0.32
NGC 3972	13A-107		low	5.0	5	29.9 $\times$ 18.3	73.6	0.50
NGC 4051	WSRT	12.0	30'' smooth	4.1	–	29.5 $\times$ 29.0	0.0	2.80
	WHISP		full res.	4.1	–	14.3 $\times$ 10.2	0.0	2.49
NGC 4138	VLA/AB678	5.6	low	5.2	5	18.5 $\times$ 20.8	75.0	0.55
NGC 4389	VLA	5.1	low	5.0	5	30.3 $\times$ 17.8	68.6	0.60
	13A-107		high	5.0	-0.5	19.8 $\times$ 12.3	75.9	0.70
UGC 07639	VLA	5.8	low	5.0	5	17.9 $\times$ 17.6	-27.4	0.46
	13A-107		high	5.0	-0.5	14.2 $\times$ 12.4	-45.6	0.60
NGC 5033	VLA	14.0	medium	20.7	0.5	21.1 $\times$ 19.9	80.5	0.26
	AP270		high	20.7	-0.5	15.9 $\times$ 14.6	-89.9	0.32
NGC 5055	VLA	9.2	taper	10.3	5	39.5 $\times$ 36.5	22.2	0.30
	AT172,AT185		high	10.3	-0.5	9.4 $\times$ 8.1	46.9	0.44
UGC 08839	VLA	5.9	low	5.0	5	36.4 $\times$ 17.2	52.0	0.47
	13A-107		high	5.0	-0.5	20.7 $\times$ 13.0	55.5	0.62
NGC5608	VLA	6.9	low	5.0	5	33.6 $\times$ 18.1	64.0	0.59
	13A-107		high	5.0	-0.5	18.3 $\times$ 12.7	68.1	0.73

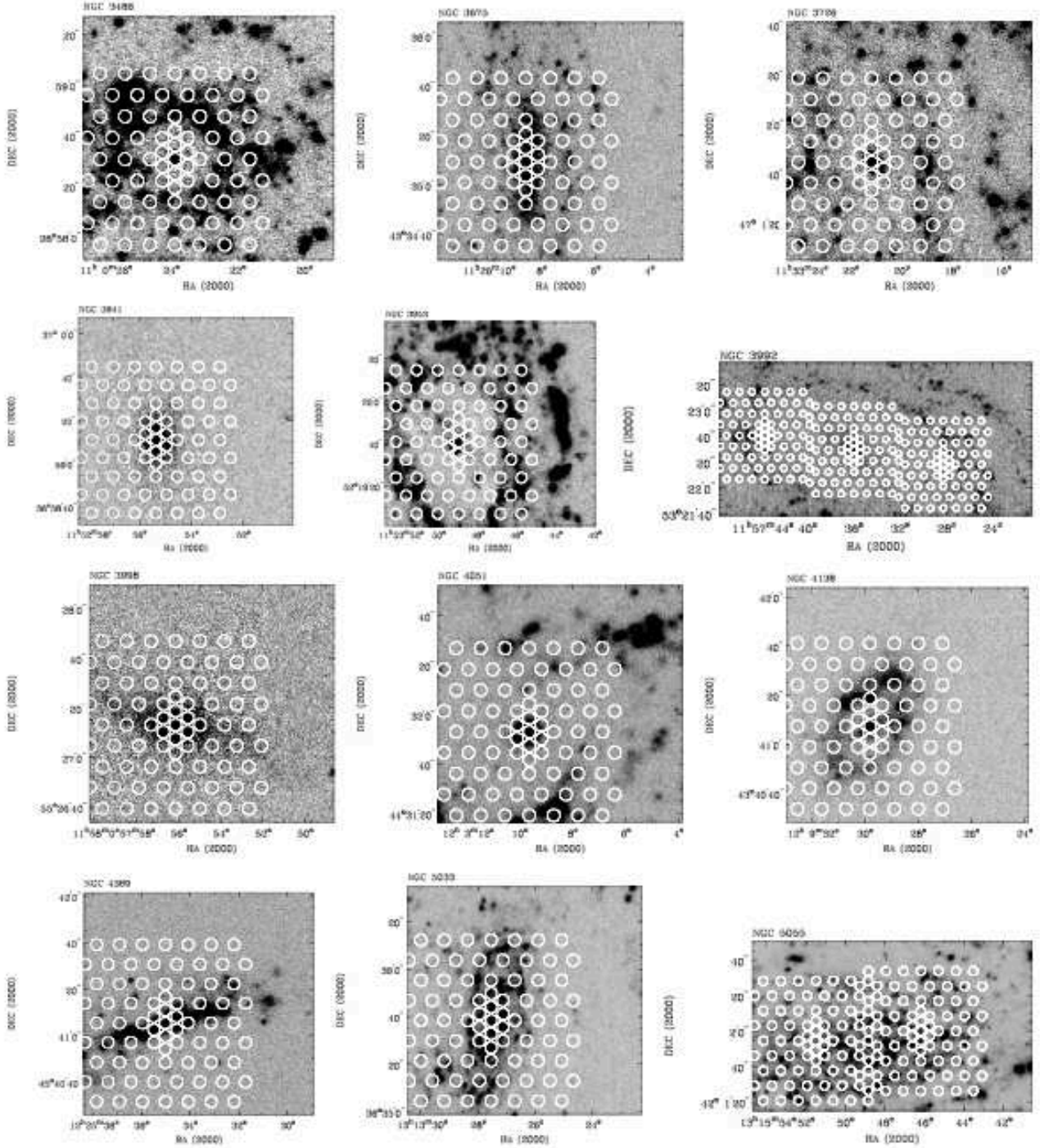


**Figure 2.** SparsePak fiber footprints for one pointing (dithers not shown) overlaid on the narrowband H $\alpha$  images. Fibers designated as 'sky' are just outside the field-of-view.



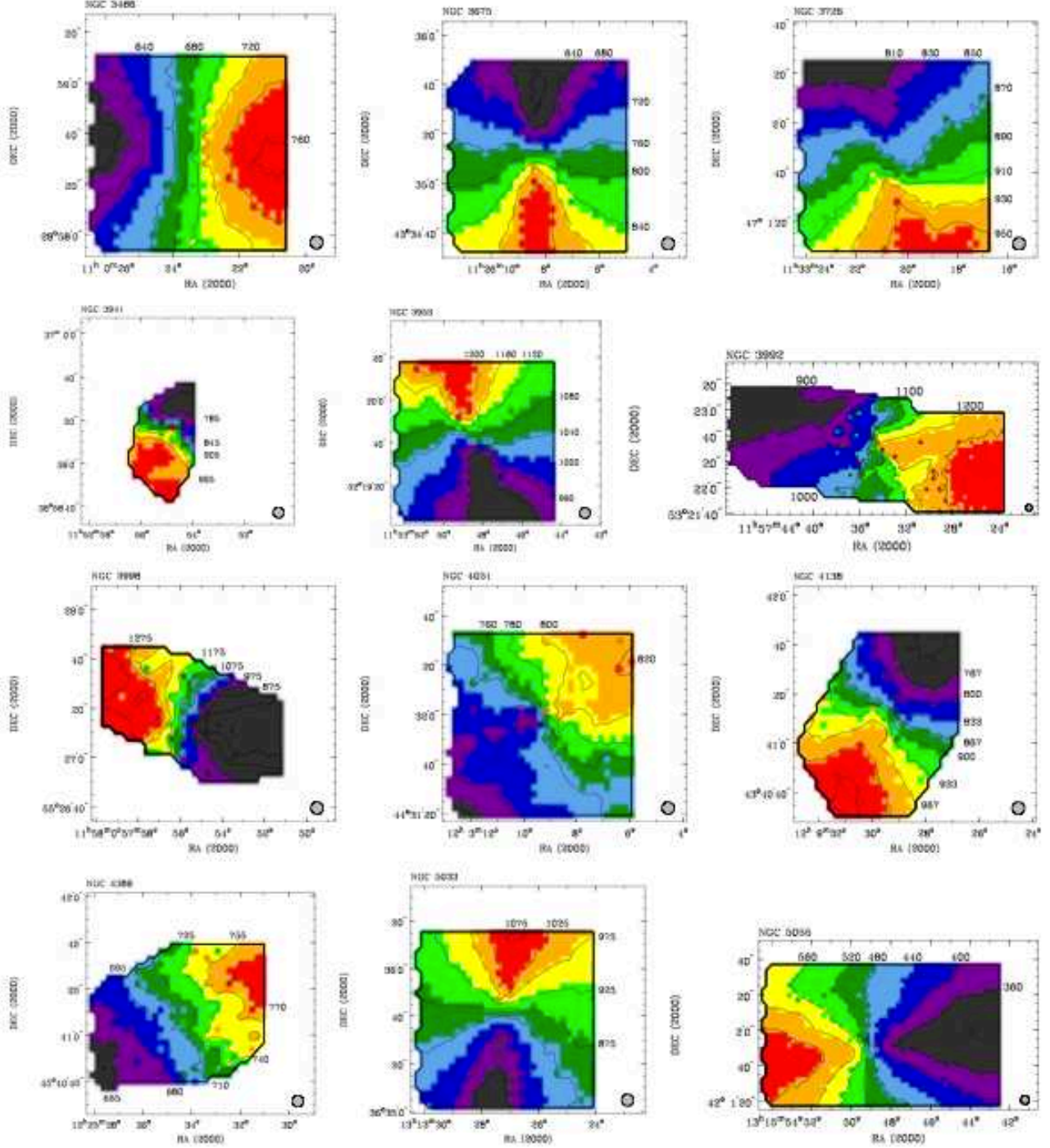


Figure 3. Ionized gas velocity fields from the SparsePak data.

quired from the CARMA STING survey (Rui Xue, private communication). NGC 3941 and NGC 3998 were observed as part of ATLAS<sup>3D</sup> (Young et al. 2011), but were not formally detected above  $3\sigma$ . The three dwarf irregular galaxies in this sample, UGC 07639, UGC 08839, and NGC 5608, as well as NGC 4389 have no CO observations available in the literature.

## 2.5 Spitzer 3.6 $\mu$ m Data

In this analysis, we take advantage of 3.6 $\mu$ m imaging observations from the Infrared Array Camera (IRAC) on the *Spitzer Space Telescope* to provide an unbiased census of the underlying stellar populations in galaxies. Specifically, the 3.6 $\mu$ m images are relatively insensitive to radial changes in M/L that might be introduced by either internal dust obscuration or changes in the dominant stellar population. The M/L ratio at 3.6 $\mu$ m is nearly independent of star formation history (e.g. Li et al. 2007; Meidt et al. 2014; Röck et al. 2015), and emission at 3.6 $\mu$ m is predominantly stellar and not greatly affected by PAH emission at 3.3 $\mu$ m (Meidt et al. 2012). This allows many of the uncertainties associated with the stellar mass distribution to be minimized.

The 3.6 $\mu$ m imaging observations were acquired in 2011–2013 as part of *Spitzer's* Cycle 8. Observations of each galaxy were conducted in a grid-like mapping pattern of dithered pointings to cover a total area 5 times the optical radius  $R_{25}$ . Each pixel in the resulting map has a total exposure time of 1800 s, which provides a sensitivity of a few  $\times 0.01$   $M_{\odot}$   $\text{pc}^{-2}$ . After standard processing, the individual pointings were combined into maps using the MOsaicker and Point source EXtractor (MOPEX) software. Images were drizzled to improve the resolution from the native pixel scale of 1.2 arcsec pixel<sup>-1</sup> to 0.75 arcsec pixel<sup>-1</sup> (Fazio et al. 2004). The maps were fit for a first order sky subtraction to remove any gradient in the sky level. Foreground stars were replaced by interpolated values based on nearest neighbor intensities.

Aperture photometry on the 3.6 $\mu$ m images was carried out using the GALPHOT<sup>4</sup> package for IRAF following the analysis steps in Richards et al. (2015). Concentric, con-eccentric ellipses were used to measure surface magnitudes and the integrated magnitude at  $R_{25}$  (Section 2.6), which is given in Table 1. No foreground extinction correction was used for the NIR since the expected value is negligible in these high galactic latitude fields. The total stellar mass presented in Table 2 was determined from the total stellar luminosity at 3.6 $\mu$ m using a M/L of  $0.5 \pm 0.1$ . The luminosity was calculated from the absolute magnitude at 3.6 $\mu$ m, which includes a correction based on an extrapolation of the 3.6 $\mu$ m surface brightness on the order of 0.01–0.03 mag. The ellipse photometry was also used to estimate the concentration of light using radii containing 20 per cent and 80 per cent of the total luminosity. The values were estimated using the curve of growth, following the method and definition in Kent (1985) (see Table 3). In this definition, values of  $C_{28}$  range from 2 to 5, where disc-dominated galaxies

have values between 3 and 4, elliptical or spheroidal systems have values  $> 4$ , and galaxies with low central surface brightness or low internal velocity dispersions have values  $< 3$  (Conselice 2003). As expected from their classifications (Table 1), most of the galaxies in this sample roughly follow the concentration trends. However, NGC 3998, NGC 4051 and NGC 5033 have abnormally high  $C_{28}$  values. This could be related to nuclear activity as NGC 3998 is classified as a LINER and NGC 4051 and NGC 5033 are classified as Seyferts (Ho et al. 1997). In these cases, the nuclear activity causes the central few pixels in the images to be unusually bright, skewing the luminosity-weighted concentration measurement to higher values.

## 2.6 Optical Data

While the *Spitzer* 3.6 $\mu$ m images give robust estimates of the total stellar distribution in galaxies, we turn to optical imaging to provide insight into the dominant stellar populations. In particular, comparison of broadband  $B$  and  $R$  images reveal changes in age or metallicity while narrowband  $H\alpha$  images provide information about current star formation activity. Optical imaging observations were taken with the WIYN 0.9 m telescope at Kitt Peak National Observatory in 2013–2015 with the Half Degree Imager (HDI) and S2KB imager. Narrowband imaging was done using a filter with FWHM of 60 Å centered at a wavelength of 6580 Å. A filter with similar FWHM and slightly offset central wavelength was used for continuum subtraction. The  $H\alpha$  images were taken with total exposure times of  $2 \times 20$  min in the 6580 Å filter, and 20 min in the narrowband continuum filter. Broadband imaging was done with three exposures of 900 s and 300 s with the  $B$  and  $R$  filters, respectively. Additional short exposures were acquired when necessary to replace saturated pixels in the cores of bright galaxies. The optical images were reduced and analysed with IRAF following the steps listed in Richards et al. (2015).

Similar to the 3.6 $\mu$ m image analysis, aperture photometry using concentric, con-eccentric ellipses was carried out to derive surface brightness magnitudes for the  $B$ - and  $R$ -band images for each galaxy. Table 1 gives measured integrated magnitudes derived from the aperture photometry. The integrated apparent magnitudes tabulated here are measured at the radius at which the  $B$ -band surface brightness equals 25 mag arcsec<sup>-2</sup> ( $R_{25}$ ) and are not corrected for foreground extinction. The absolute  $B$ -band magnitude listed in Table 2 has been corrected for extinction (Schlafly & Finkbeiner 2011) and includes a correction based on an extrapolation of the  $B$ -band surface brightness profile. Integrated colours tabulated in Table 2 are also measured at  $R_{25}$  and have been extinction corrected.

Aperture photometry was performed on the  $H\alpha$  images to measure  $H\alpha$  fluxes and derive equivalent widths (EW). The current total star formation rate (SFR) is derived from the  $H\alpha$  flux measured at  $R_{25}$  using the calibration given in Kennicutt & Evans (2012). The reported SFRs have not been corrected for [NII]  $\lambda 6584$  flux which falls within the narrowband filter. In some galaxies, the [NII]  $\lambda 6584$  line may be a large contributor to the total measured flux (e.g. Section 2.3). This is most likely the case for NGC 3941 and NGC 3998, whose integrated spectra show dominant [NII]  $\lambda 6584$  lines. In other galaxies (i.e. NGC 5005;

<sup>4</sup> GALPHOT is a collection of scripts in the IRAF STSDAS environment first developed by W. Freudling and J. J. Salzer. The current version has been further enhanced by members of the Cornell Extragalactic Group and is maintained by M. P. Haynes.

Richards et al. 2015), internal extinction may play a larger role. Therefore, the SFRs in Table 2 should be taken as indicative only. The EW of the H $\alpha$  emission line is used as a tracer of the specific star formation rate. It is calculated by dividing the H $\alpha$  flux by the continuum flux density measured from the H $\alpha$  narrowband continuum filter. It, therefore, serves as an indicator of the strength of the current SFR relative to the past average SFR. A larger EW value would indicate a larger current SFR relative to the continuum, or past average star formation.

Radial profiles were additionally created to examine the surface brightness profiles as well as gradients in colour and EW. Table 3 gives estimates of the EW gradient and  $B - R$  colour gradient from a linear fit to the radial profiles. Often, the radial trends in these profiles are not linear, but the sign of the value reported in Table 3 provides a rough picture of the star formation history and changes in the dominant stellar population. A negative gradient in  $B - R$  colour is indicative of a transition from redder in the bulge-dominated nuclear region to bluer in the disc where most of the recent star formation is occurring, as is expected for spiral galaxies (e.g. Markarian et al. 1965). A corresponding EW gradient would have a positive sign with higher EW values at larger radii in the disc where there is more current star formation relative to past star formation. Interesting features of each galaxy's surface brightness profile, colour and EW gradients are described in more detail in Section A.

### 3 RESULTS

In this section, we focus on the galaxy kinematics and rotation curve decomposition analysis. Neutral and ionized gas rotation curves are shown in Fig. 4, and kinematic properties are summarized in Table 5. Rotation curve decompositions are shown in Fig. 5 and results of the decomposition are given in Table 6.

#### 3.1 Neutral and Ionized Gas Kinematics

Data products from both new and archival HI observations were analysed using standard tools distributed as part of the GIPSY software package (van der Hulst et al. 1992). Integrated intensity maps and intensity-weighted mean velocity fields were extracted from the data cubes following the process outlined in Richards et al. (2015).

Rotation curves for each galaxy were derived by fitting a series of concentric tilted rings to the HI velocity fields and SparsePak ionized gas velocity fields separately (GIPSY task ROTCUR). The ring centre coordinates ( $x_0$ ,  $y_0$ ), systemic velocity ( $V_{\text{sys}}$ ), inclination angle ( $i$ ), position angle (P.A.), and rotation velocity ( $V_{\text{rot}}$ ) were iteratively fit following the method detailed in Richards et al. (2015). The expansion velocity was always fixed to zero. Initially, the rings were allowed to vary in position and inclination angle as a function of radius to account for warps. Then, a smoothly varying or constant distribution in  $i$  and P.A. was adopted to derive the underlying bulk rotation and prevent spurious second-order effects in the rotation curve. The final azimuthally averaged rotation curve was derived with all other ring parameters fixed. Fig. 4 shows the rotation curve results for each galaxy in this sample.

As in Richards et al. (2015), uncertainties in the neutral gas rotational velocities are estimated to be a combination of non-circular thermal gas motions and inclination errors. Uncertainties due to thermal gas motions were estimated to be 10 per cent of the average velocity dispersion values as measured from a velocity dispersion map created from the highest usable resolution HI data. Uncertainty due to kinematic asymmetries was also taken into account by assuming an error equal to 0.25 times the absolute difference between the circular velocities of the approaching and receding sides (de Blok et al. 2008). Uncertainty of the inclination angle is typically on the order of  $\pm 5^\circ$ , which translates to 5-20 per cent error on the circular velocity. This is the dominant source of uncertainty in the rotation velocities. For this reason, only uncertainties due to inclination angle errors were calculated for the ionized gas rotational velocities.

There is generally good agreement between the neutral and ionized gas kinematics when they overlap. However, there are a few cases where the ionized gas peaks at larger rotational velocities than is seen in the HI (e.g. NGC 3675 and NGC 3998 in Fig. 4). These discrepancies can usually be explained through a combination of beam smearing in the HI and effects of non-circular motions on the ionized gas from nuclear activity. In the cases of NGC 3675, NGC 5033 and NGC 5055, the largest discrepancy between the ionized and neutral gas rotation curves occurs within about two resolution elements of the HI observations. The lower spatial resolution of the HI data has the effect of making the inner slope of the rotation curve appear shallower with lower rotational velocities. A discussion of how the uncertainty in the central rotational velocities affects the derived distribution of mass is given below.

#### 3.2 Rotation Curve Decompositions

We use the method of rotation curve decomposition to uncover the distribution of baryonic and non-baryonic mass in galaxies (e.g. de Blok et al. 2008). Estimates of stellar and gas distributions are used in conjunction with the rotation curve derived from the neutral and ionized gas kinematics to constrain the distribution of dark matter as a function of radius (e.g. de Blok & Bosma 2002).

Total gas mass and stellar light surface density profiles are used to calculate the contributions from gas and stars to the overall rotation curve. The atomic mass surface density was measured from the HI integrated intensity maps for every galaxy. The molecular mass surface density was measured in the same way when integrated CO intensity maps were available or was interpolated from individual pointings. A CO/H $_2$  conversion factor of  $2 \times 10^{20} \text{ cm}^{-2} (\text{K km s}^{-1})$  was assumed when calculating molecular gas mass. The atomic and molecular gas distributions were derived separately and then added together to create a total gas mass surface density distribution. The total gas mass was multiplied by a factor of 1.4 to account for primordial helium.

The GIPSY task ROTMOD was used to calculate model rotation curves for both the gas and stars as described in Richards et al. (2015). For the gas, an infinitely thin disc is assumed. Model rotation curves for the stellar distributions were derived from the  $3.6\mu\text{m}$  light surface density profiles. In most cases, this light could be well described as a disc distribution only. The disc potential was constructed assuming



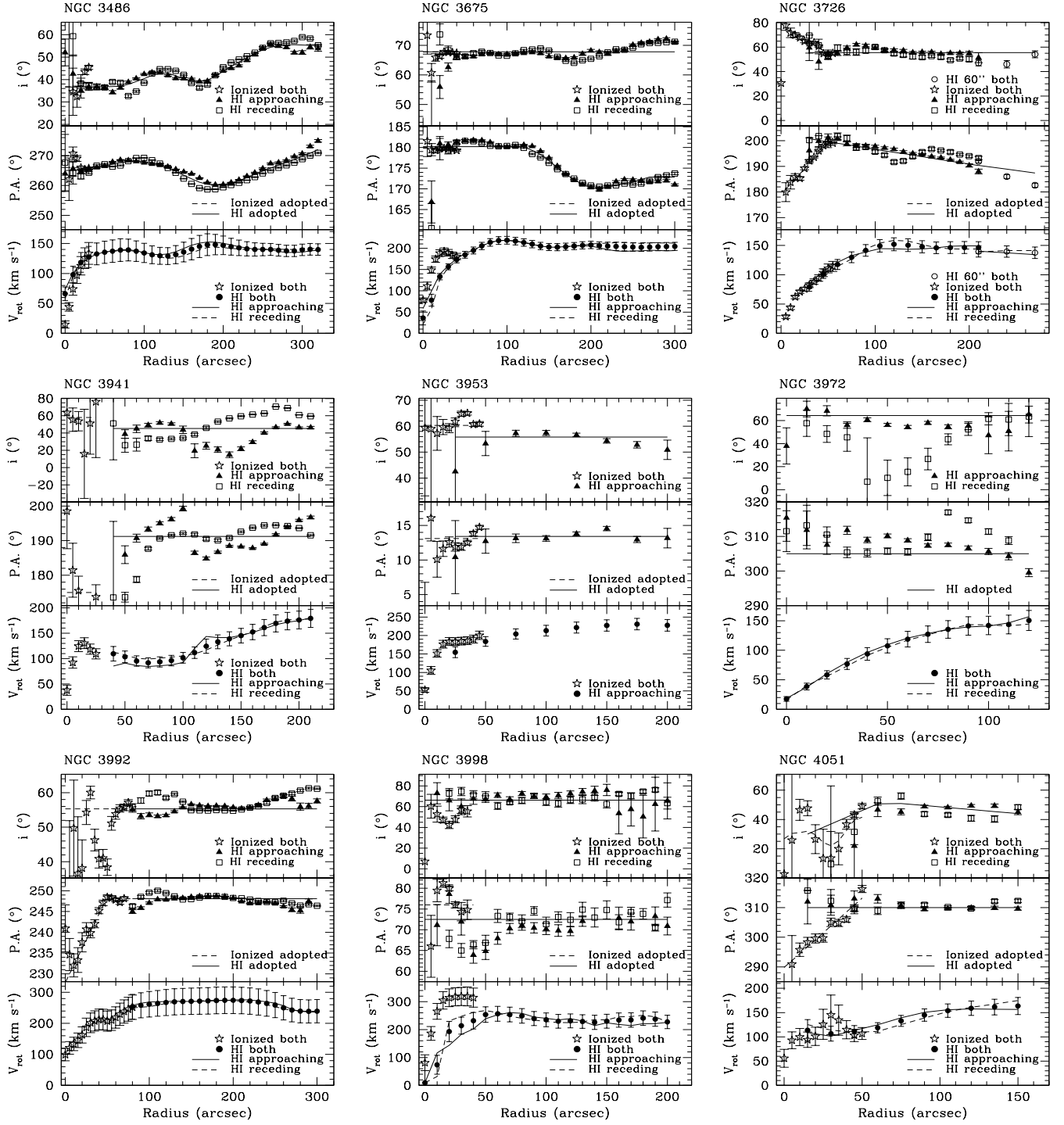


**Figure 4.** Rotation curves for VLA HI and SparsePak ionized gas derived from tilted rings using the GIPSY task ROTCUR. The panels for each galaxy include the inclination angle (top), position angle (middle) and circular rotation velocity (bottom). Inclination and position angle fits to the approaching (*filled triangles*) and receding (*open squares*) sides and the adopted fits to both sides (*solid line*) are derived from the HI velocity field. Both sides of the ionized gas velocity field are fit at the same time (*open stars*). The *dashed line* shows the adopted ionized gas fits. Circular rotational velocities for the HI (*filled circles*) and SparsePak ionized gas (*open stars*) are derived using the adopted inclination and position angles at each radius. The *dotted* and *dash-dotted* lines show the separate circular rotational velocities derived for the approaching and receding sides of the HI velocity field, respectively, using the same adopted inclination and position angles.



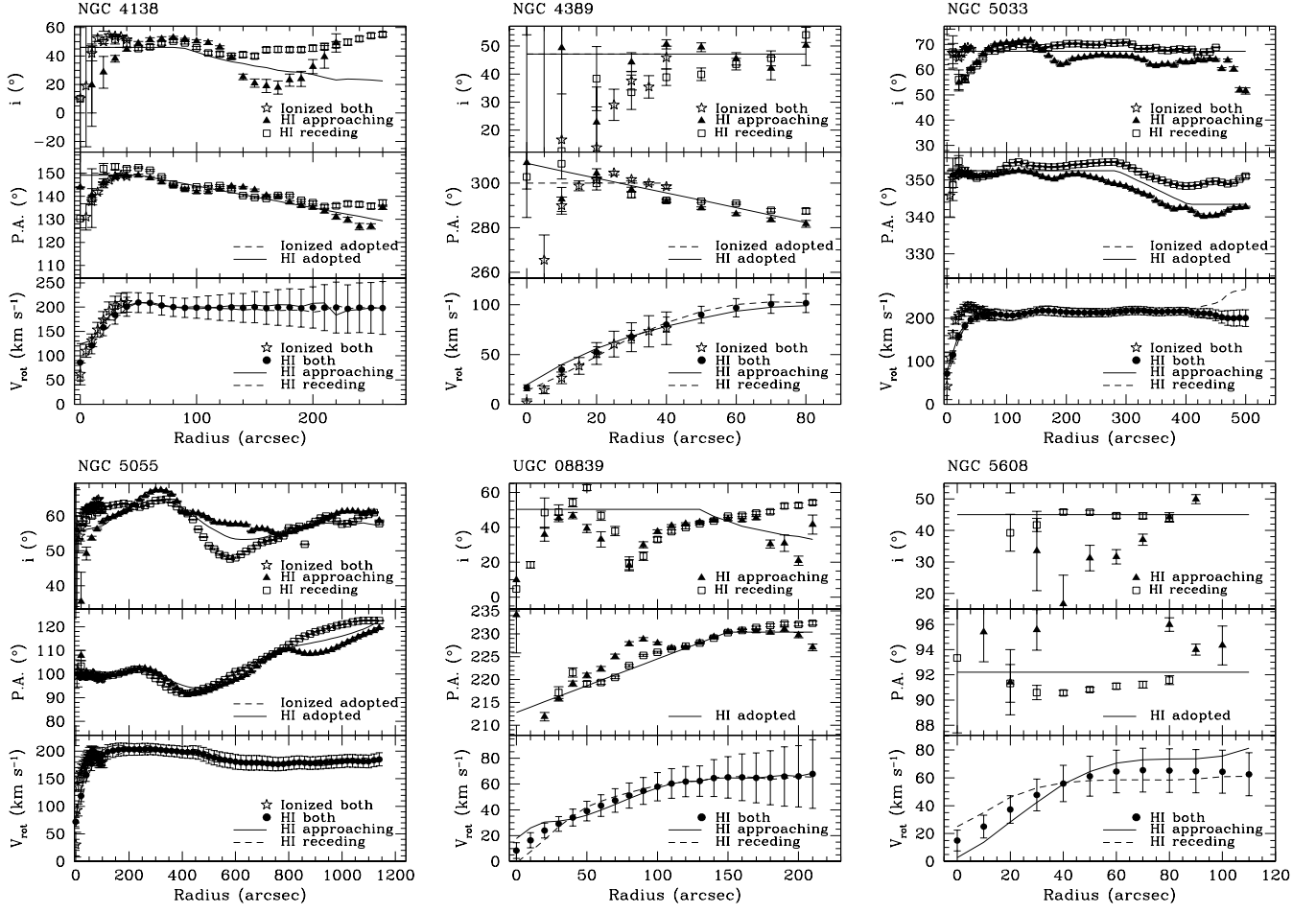


Figure 4. Continued.

Table 5. Kinematic Properties

Galaxy	Kinematic centre		Systemic velocity	Adopted <sup>†</sup>	Adopted <sup>†</sup>
	RA	Dec	(km s <sup>-1</sup> )	position angle	inclination angle
	(J2000)	(J2000)		(deg)	(deg)
NGC 3486	11:00:23.82	+28:58:31.2	678	266	36.8
NGC 3675	11:26:08.54	+43:35:11.1	763	176	67.8
NGC 3726	11:33:20.78	+47:01:47.8	864	195	55.5
NGC 3941	11:52:55.36	+36:59:11.0	934	191	45.4
NGC 3953	11:53:48.99	+52:19:34.6	1050	13.4	55.8
NGC 3972	11:55:45.69	+55:19:18.6	845	305	64.4
NGC 3992	11:57:35.94	+53:22:28.0	1049	248	55.3
NGC 3998	11:57:56.16	+55:27:08.3	1062	72.5	66.3
NGC 4051	12:03:09.85	+44:31:53.4	704	310	44.6
NGC 4138	12:09:29.75	+43:41:07.6	888	141	36.0
NGC 4389	12:25:34.93	+45:41:03.5	731	296	47.1
UGC 07639	12:29:52.69	+47:31:48.3	378	96.0	52.5
NGC 5033	13:13:27.44	+36:35:38.3	875	350	67.3
NGC 5055	13:15:49.14	+42:01:44.1	512	106	58.5
UGC 08839	13:55:25.41	+17:47:46.3	966	230	46.1
NGC 5608	14:23:18.54	+41:46:35.2	670	92.0	45.0

<sup>†</sup> Average value reported when adopted value varies with radius.

a vertical mass density distribution of  $\text{sech}^2(z/z_0)$ , where  $z_0 = 2h_R/q$ . The oblateness parameter,  $q$ , is calculated using the fiducial relation derived in [Bershady et al. \(2010\)](#):

$$\log(q) = 0.367 \log(h_R/\text{kpc}) + 0.708. \quad (1)$$

However, for NGC 3953, NGC 5033 and NGC 5055, the bulge component was a non-negligible contributor to the distribution of the stellar mass. In those cases, model rotation curves were derived separately for the bulge and disc, based on a decomposition of the  $3.6\mu\text{m}$  image. A spherical distribution was assumed for the bulge model rotational velocities.

As briefly described in Section 3.1, it can be challenging to trace the central gravitational potential in galaxies with other dynamical contributions from bars or active nuclei. This is an issue for the rotation curve decomposition when the stellar disc/bulge is assumed to contribute maximally. In this assumption, the total mass of the stellar content is set by scaling it such that the inner dynamics can be fully described by the gravitational influence of the baryons, without the need for dark matter. This breaks the degeneracy between the unknown absolute contribution from the stars and the contribution from dark matter to the total mass of the galaxy by setting an upper limit on the baryon content. However, if the inner rotational velocities are being affected by dynamics other than the gravitational potential, then the stellar contribution is essentially being scaled arbitrarily to something that does not depend on the mass. This problem is avoided when the stellar disc/bulge M/L is fixed in the decomposition analysis.

Rotation curve decomposition results for each galaxy are shown in Fig. 5. Circular rotation velocities for the total gas, stellar bulge and stellar disc were summed in quadrature and subtracted from the observed rotation curve. The stellar bulge and disc M/L ratios were assumed to be constant with radius and fixed at 0.5 with a  $\pm 0.1$  allowed variance to take into account distance uncertainties (See Section 2.1). Both the bulge and disc were fixed to the same M/L value. A spherical pseudo-isothermal dark matter halo model was fit to the residuals (e.g. [Ostriker & Caldwell 1979](#); [Kent 1986](#)). The halo parameters  $R_C$  and  $V_H$ , where  $R_C$  is the halo core radius and  $V_H$  is the maximum velocity of the halo, were left as free parameters to be fit during the decomposition.

An interactive, iterative approach was used to determine a reasonable fit for each galaxy. The same intermediate radial range free from the influence of warps in the outer rotation curves which was used to determine  $V_{\text{flat}}$  was used to determine the fit in the decomposition. Table 6 lists the dark matter halo parameters fit in the decomposition. We do not try to model warps in the outer rotation curves where it cannot be confirmed that the rotational velocities are tracing the circular speed of the gravitational potential. The errors given for the fixed M/L derived  $M_{\text{bary}}/M_{\text{tot}}$  at  $2.2h_R$  and  $R_{\text{trans}}$  values are the computed average range of possible values assuming a  $\pm 0.1$  difference in M/L.

For comparison, a decomposition was additionally performed for each galaxy assuming the stellar disc and bulge contribute maximally to the inner observed rotation curve on top of the contribution from the gas. A separate maximal M/L value was fit for the disc and bulge when both components are present. The maximum disc/bulge M/L values and dark matter halo parameters for these fits are also listed in

Table 6. Based on the evidence for the stellar M/L at  $3.6\mu\text{m}$   $\sim 0.5$  (e.g. [Eskew et al. 2012](#); [McGaugh & Schombert 2015a](#); [Lelli et al. 2016](#)), the fixed M/L decompositions appear to offer more astrophysically plausible results. It is important to note, however, that without additional constraints on the true baryonic contribution, it is not possible to distinguish either the maximal disc/bulge or fixed M/L decomposition as the correct result. The magnitude of the differences between these two decompositions is explored in Section 4.

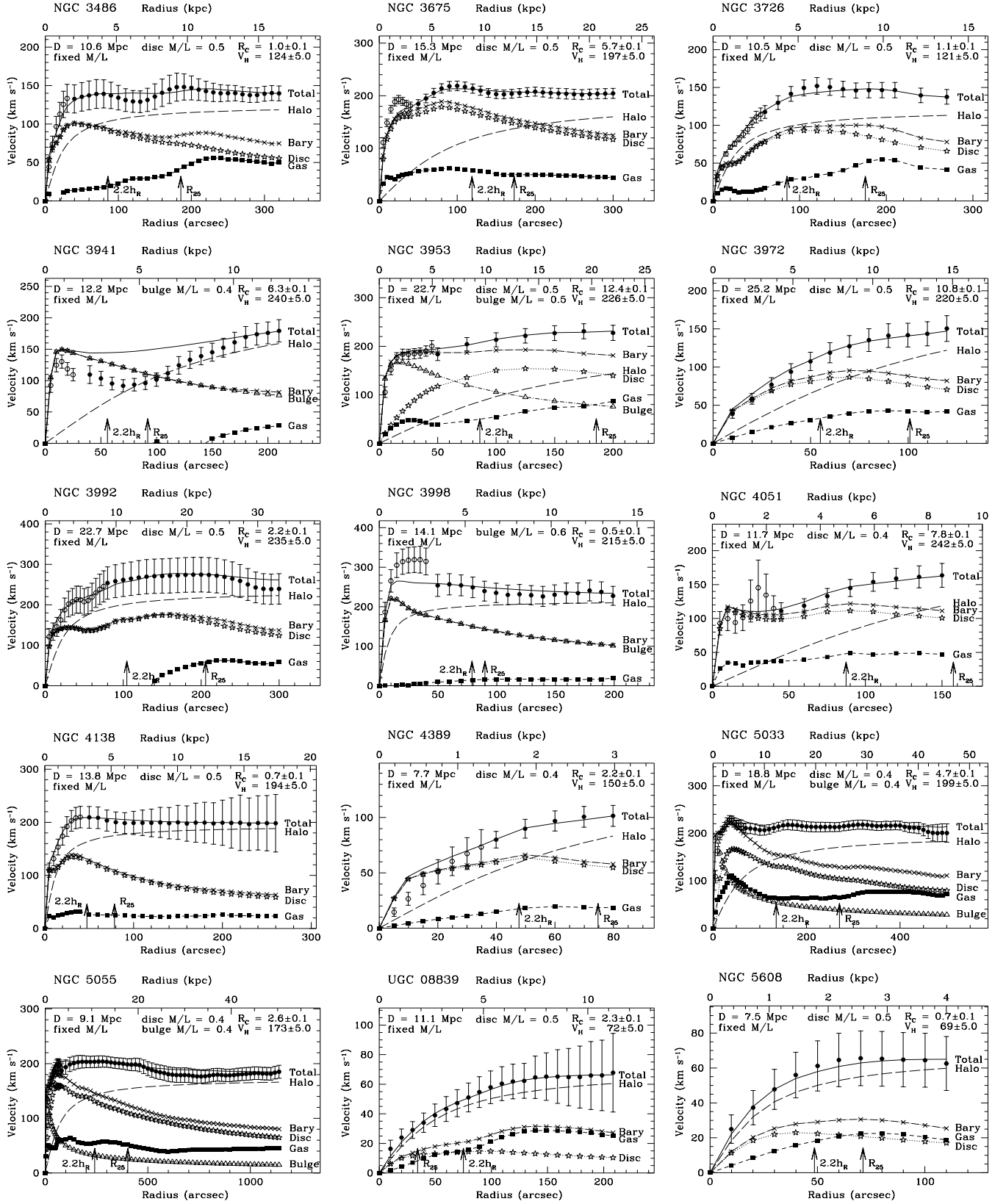


**Figure 5.** Rotation curve decompositions assuming a fixed stellar disc/bulge  $M/L = 0.5 \pm 0.1$  for each galaxy. The total gas (filled squares), stellar bulge (open triangles), stellar disc (open stars), and dark matter halo model (dashed line) components are added in quadrature to achieve the best overall fit to the observed rotation curve. Open circles represent circular rotation velocities derived from the ionized gas (SparsePak) observations and the filled circles are from the HI observations. Adding the baryonic components in quadrature without the dark matter results in the crosses.

**Table 6.** Rotation Curve Decomposition Results

Galaxy	Dynamical <sup>a</sup> Mass ( $10^{10} M_{\odot}$ )	M/L <sub>disc</sub> , M/L <sub>bulge</sub>		$R_C$ (kpc)		$V_H$ (km s <sup>-1</sup> )		$M_{\text{bary}}/M_{\text{tot}}$ <sup>b</sup> (at $2.2h_R$ )		$R_{\text{trans}}$ <sup>c</sup> (kpc)		$(h_R)$	
		fixed	max	fixed	max	fixed	max	fixed	max	fixed	max	fixed	max
NGC 3486	7.48±0.04	0.5, –	1.0, –	1.0±0.1	7.9±0.1	124±5	158±5	0.46±0.08	0.82	3.4±2.9	13.7	1.7±1.4	6.8
NGC 3675	21.6±0.1	0.5, –	0.7, –	5.7±0.1	16.8±0.1	197±5	268±5	0.69±0.12	0.88	15.1±3.7	21.1	3.8±0.9	5.3
NGC 3726	6.05±0.03	0.5, –	1.1, –	1.1±0.1	12.7±0.1	121±5	181±5	0.46±0.09	0.95	1.1±0.4	>13.7	0.5±2	>7.0
NGC 3941	9.28±0.09	–, 0.4	–, 0.3	6.3±0.1	7.5±0.1	240±5	266±5	1.7±0.4	1.3	7.8±0.9	7.0	5.2±0.6	4.7
NGC 3953	26.5±0.1	0.5, 0.5	0.7, 0.5	12.4±0.1	20.0±0.1	226±5	231±5	0.82±0.15	0.94	>22.0	>22.0	>5.1	>5.1
NGC 3972	7.71±0.10	0.5, –	0.6, –	10.8±0.1	9.8±0.1	220±5	199±5	0.63±0.11	0.73	9.6±1.7	10.7	3.1±0.6	3.5
NGC 3992	44.0±1.1	0.5, –	0.8, –	2.2±0.1	3.0±0.1	235±5	198±5	0.39±0.08	0.62	3.5±1.8	31.9	0.67±0.34	6.1
NGC 3998	16.4±0.2	–, 0.6	–, 1.4	0.5±0.1	13.3±0.1	215±5	386±5	0.36±0.06	0.84	1.1±0.2	11.7	0.44±0.09	4.8
NGC 4051	5.30±0.06	0.4, –	0.5, –	7.8±0.1	6.7±0.1	242±5	205±5	0.72±0.15	0.84	≥7.8	>8.5	≥3.5	>3.8
NGC 4138	15.9±1.2	0.5, –	1.1, –	0.7±0.1	3.8±0.1	194±5	213±5	0.39±0.07	0.85	1.7±0.9	7.1	1.2±0.6	4.9
NGC 4389	0.71±0.01	0.4, –	0.1, –	1.8±0.1	1.3±0.1	133±5	135±5	0.55±0.13	0.23	2.0±0.4	0.7	2.5±0.4	0.8
NGC 5033	42.6±0.4	0.4, 0.4	0.4, 0.4	4.7±0.1	3.7±0.1	199±5	194±5	0.53±0.11	0.50	13.6±5.6	12.3	2.4±1.0	2.2
NGC 5055	40.1±0.2	0.4, 0.4	0.5, 0.4	2.6±0.1	5.1±0.1	173±5	177±5	0.51±0.11	0.64	11.2±4.9	16.8	2.3±1.0	3.5
UGC 08839	1.20±0.18	0.5, –	3.0, –	2.3±0.1	5.6±0.1	72±5	85±5	0.18±0.02	0.59	<0.5	6.0	<0.3	3.3
NGC 5608	0.36±0.02	0.5, –	1.8, –	0.7±0.1	1.5±0.1	69±5	71±5	0.23±0.03	0.59	<0.4	2.3	<0.5	2.8

<sup>a</sup> Calculated using the last measured rotation curve point.<sup>b</sup> Relative baryonic contribution to the total observed gravitational potential measured at 2.2 times the average disc radial scale length,  $h_R$ .<sup>c</sup> The radius at which the gravitational potential transitions from baryon-dominated to dark matter-dominated (where  $M_{\text{bary}}/M_{\text{tot}} = 0.5$ ) expressed in kpc and in terms of disc radial scale lengths ( $h_R$ ) measured at  $3.6\mu\text{m}$ .



#### 4 DISCUSSION

With rotation curve decompositions in hand, we examine how strongly the inferred distribution of mass is altered between fixed M/L and maximal disc/bulge assumptions. Fig. 6 shows the radial distribution of  $V_{\text{bary}}^2/V_{\text{tot}}^2$ , as determined from the model gas and star rotation curves and total observed rotation curve. The true quantity being traced is the baryonic contribution to the total potential of the galaxy, which is equivalent to the ratio of baryonic mass to total mass in the limit of spherical distributions, so it is denoted as  $M_{\text{bary}}/M_{\text{tot}}$ . The radial extent of each galaxy is scaled by its average disc scale length measured at  $3.6\mu\text{m}$ . The galaxies are separated by  $V_{\text{flat}}$  to distinguish the more massive spiral galaxies from the less massive dwarf galaxies. The top panel in Fig. 6 shows the baryon mass fraction distribution derived from the maximum stellar disc/bulge decompositions. The bottom panel displays the baryon mass fraction distribution results from the fixed M/L =  $0.5 \pm 0.1$  decompositions shown in Fig. 5. Note that  $\log_{10}(M_{\text{bary}}/M_{\text{tot}})$  ratios greater than zero occur when the estimated total baryonic contribution (the rotation curve labelled ‘Bary’ in Fig. 5) over-estimates the observed rotational velocities in the centre. There is no noticeable difference in the distribution of baryonic to total mass for galaxies of different  $V_{\text{flat}}$ , or baryonic mass, except for the lowest mass galaxies when a fixed M/L is used. A similar result was found for the THINGS sample (de Blok et al. 2008).

Dashed lines demarcating  $M_{\text{bary}}/M_{\text{tot}} = 0.5$  and  $2.2h_R$  have been added to each plot of Fig. 6 to exemplify the differences between the two versions of the mass decomposition. By design, the baryon mass fraction at  $2.2h_R$  is higher in the maximum disc/bulge decompositions with a mean and standard deviation of  $0.75 \pm 0.24$ , and with most galaxies having baryon mass fractions greater than 0.5. This can also be seen in the left panel of Fig. 7 where all but one galaxy lies at or above  $M_{\text{bary}}/M_{\text{tot}} = 0.5$  for the maximum disc/bulge results. All but two galaxies have baryon mass fractions at  $2.2h_R$  in their fixed M/L decompositions which are the same or less than the maximum disc/bulge results. The two exceptions are NGC 3941 and NGC 4389, both of which are likely cases where the rotation curves are not tracing the gravitational potential of the galaxy (see Sections A4 and A11). The baryon mass fractions at  $2.2h_R$  for the fixed M/L decompositions have a mean and standard deviation of  $0.57 \pm 0.35$ , or  $0.49 \pm 0.19$  if NGC 3941 and NGC 4389 are excluded. On average, the fixed M/L baryon mass fraction results are lower by  $0.3 \pm 0.1 M_{\text{bary}}/M_{\text{tot}}$  at  $2.2h_R$  than the maximum disc/bulge results. The ratio between the maximum disc/bulge and fixed M/L baryon mass fraction results scale directly with the ratio of M/L, assuming stellar mass is the dominant contributor to the total baryonic mass component at  $2.2h_R$ .

Another consequence of maximizing the baryonic contribution to the observed rotation curve in the maximum disc/bulge scenario is that it pushes the baryon to dark matter-dominated transition to a larger radius. The right panel of Fig. 7 compares the transition radius,  $R_{\text{trans}}$ , normalized by disc scale length for each galaxy from the fixed M/L and maximum disc/bulge decompositions. Although the standard deviations of the normalized  $R_{\text{trans}}$  values are similar in each case, the median value of the maximum

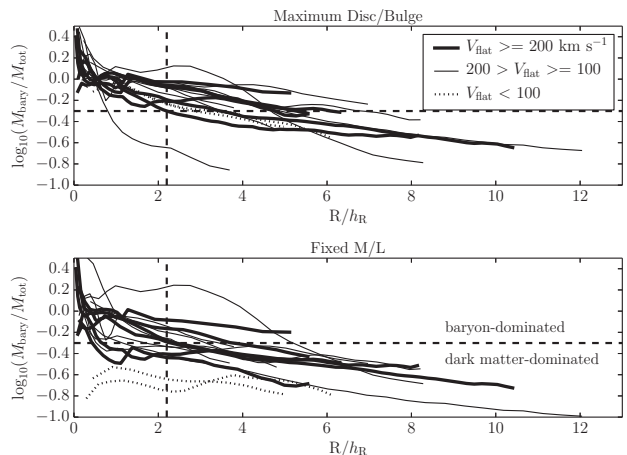


**Figure 6.** Radial distribution of the mass in baryonic matter to total mass in each galaxy. The radius of each galaxy has been scaled by its average disc scale length measured at  $3.6\mu\text{m}$ . The most massive galaxies, as indicated by large  $V_{\text{flat}}$  through the BTFR (McGaugh et al. 2000), are plotted with a thick solid line, intermediate mass with a thin solid line, and the lowest mass galaxies are plotted with a dotted line. *Top:* Baryon mass fraction distribution from the results of the maximum stellar disc/bulge decompositions. *Bottom:* Baryon mass fraction distribution from the results of the fixed stellar M/L =  $0.5 \pm 0.1$  decompositions. The horizontal dashed line in each plot denotes where the mass fraction transitions from being baryon-dominated to dark matter-dominated (where  $M_{\text{bary}}/M_{\text{tot}} = 0.5$ ). The vertical dashed line marks the location of  $2.2h_R$ .

disc/bulge results is double the median value from the fixed M/L results. Understanding how  $R_{\text{trans}}$  scales with M/L is not as simple as for the baryon mass fraction. The shape of the rotation curves can affect the exact location of  $R_{\text{trans}}$  causing some galaxies to have lower  $R_{\text{trans}}$  in the fixed M/L results than would be expected from the difference in the M/L assumptions.

Figs. 6 and 7 illustrate the magnitude of the effects the assumed stellar M/L has on the distribution of mass derived from rotation curve decomposition. Even with this relatively small subset of galaxies from the complete EDGES kinematic sample, it is apparent that comparisons between the distribution of baryonic and non-baryonic matter derived in this manner will need to address the dependence on assumed M/L. In the future, we will apply the methods used in the present study to the complete EDGES kinematic sample to explore correlations between the distribution of dark matter and structural properties of the stellar disc. This will include an investigation of how the results change using an astrophysically-motivated fixed M/L and an extreme upper limit from the maximum disc/bulge M/L. Comparison to the distributions of the various mass components from cosmological hydrodynamical simulations (e.g. Schaye et al. 2015) will provide further insight into how baryons form and evolve inside dark matter haloes.

#### 5 CONCLUSION

We have presented new and archival HI synthesis observations from the VLA and WSRT and new IFS observations

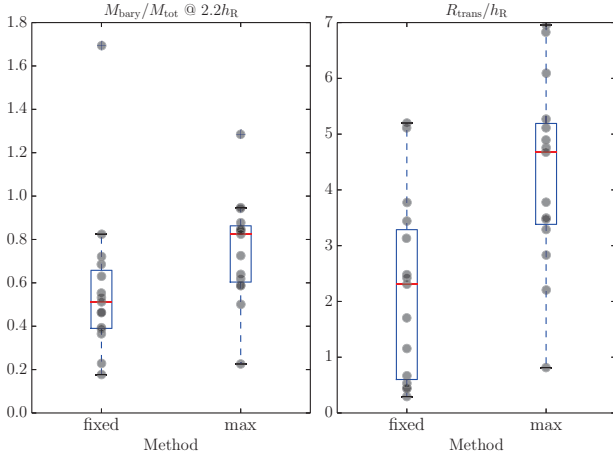


**Figure 7.** *Left:* Boxplot comparison of  $M_{\text{bary}}/M_{\text{tot}}$  at  $2.2h_{\text{R}}$  from the fixed M/L and maximum disc/bulge decompositions. The median of the results assuming a fixed M/L =  $0.5 \pm 0.1$  is 0.51, while the median for the maximum disc/bulge results is 0.82. The large outlier with a non-physical baryon mass fraction  $> 1$  is NGC 3941 whose up-bending rotation curve is likely not tracing the gravitational potential of the galaxy. *Right:* Boxplot comparison of  $R_{\text{trans}}/h_{\text{R}}$  from the fixed M/L and maximum bulge/disc decompositions. Upper and lower limits on  $R_{\text{trans}}$  are included to illustrate the range of the data. The median  $R_{\text{trans}}/h_{\text{R}}$  values for the fixed M/L and maximum disc/bulge results are 2.3 and 4.7, respectively.

from SparsePak on the WIYN 3.5 m telescope to constrain the neutral and ionized gas kinematics in sixteen galaxies. We additionally include *Spitzer*  $3.6\mu\text{m}$  images to trace the extended stellar populations, as well as optical broadband  $B$  and  $R$  and narrowband  $\text{H}\alpha$  from the WIYN 0.9 m telescope to measure properties of the dominant stellar populations. This multiwavelength dataset was used to carry out rotation curve decomposition analysis and to illustrate how the assumed stellar M/L effects the inferred distribution of mass. The main results are summarized below.

(i) New HI radio synthesis observations were obtained with the VLA in C configuration for eight galaxies, seven of which are presented in this study, to derive extended rotation curves from the neutral gas kinematics. Parameters of the resulting data cubes are provided in Table 4. In addition, new SparsePak IFS observations were acquired for twelve galaxies to use the ionized gas kinematics to constrain the rotational velocities in the central regions. Ionized gas velocity fields and combined HI and ionized gas rotation curves are presented in Fig. 3 and Fig. 4, respectively. Kinematic properties are presented in Table 5.

(ii) The ionized and neutral gas rotation curves were decomposed using model rotation curves to estimate the stellar and gas contributions to observed dynamics. The contributions from the neutral and molecular gas were determined from mass surface density measurements from HI synthesis and archival CO data. The stellar bulge and disc contributions were derived from surface brightness measurements using the *Spitzer*  $3.6\mu\text{m}$  images. The distribution of dark matter was estimated by fitting a spherical pseudo-isothermal halo model. Rotation curve decomposition results using fixed

stellar disc and bulge M/L =  $0.5 \pm 0.1$  are presented in Fig. 5 and summarized in Table 6.

(iii) Rotation curve decompositions assuming maximum contribution from the stellar disc and bulge were carried out for comparison. Results from these decompositions are presented in Table 6. We used the rotation curve decompositions for each galaxy to investigate how the baryon mass fraction is distributed as a function of radius (Fig. 6) under the fixed M/L and maximum disc/bulge assumptions. The magnitude of the differences between the two methods can readily be seen in Fig. 7. By definition, the maximum disc/bulge method results in higher baryon mass fractions measured at  $2.2$  disc scale lengths and larger transition radii. The degree to which these values change is directly related to how large the difference is in assumed M/L.

## ACKNOWLEDGEMENTS

The authors acknowledge the referee for many helpful suggestions on improving this manuscript. The authors thank J.M. van der Hulst and Martha P. Haynes for providing HI data cubes and moment maps of archival data. The authors acknowledge observational and technical support from the National Radio Astronomy Observatory (NRAO). We acknowledge use of the WIYN 0.9 m telescope operated by WIYN Inc. on behalf of a Consortium of ten partner Universities and Organizations, and the WIYN 3.5 m telescope. The WIYN Observatory is a joint facility of the University of Wisconsin-Madison, Indiana University, the National Optical Astronomy Observatory and the University of Missouri. This work is based on observations made with the *Spitzer Space Telescope*, which is operated by the Jet Propulsion Laboratory, California Institute of Technology under a contract with NASA. EER acknowledges support from the Provost's Travel Award for Women in Science, a professional development fund supported through the Office of the Provost at Indiana University Bloomington, and the Indiana Space Grant Consortium. LvZ recognizes support from the Helena Kluyver Female Visitor programme at ASTRON during which some of this analysis was completed. This research has made use of the NASA/IPAC Extragalactic Database (NED) which is operated by the Jet Propulsion Laboratory, California Institute of Technology, under contract with the National Aeronautics and Space Administration.

## REFERENCES

- Aumer M., White S. D. M., 2013, *MNRAS*, 428, 1055
- Baldwin J. A., Phillips M. M., Terlevich R., 1981, *PASP*, 93, 5
- Begeman K. G., Broeils A. H., Sanders R. H., 1991, *MNRAS*, 249, 523
- Bershady M. A., Andersen D. R., Harker J., Ramsey L. W., Verheijen M. A. W., 2004, *PASP*, 116, 565
- Bershady M. A., Verheijen M. A. W., Westfall K. B., Andersen D. R., Swaters R. A., Martinsson T., 2010, *ApJ*, 716, 234
- Bershady M. A., Martinsson T. P. K., Verheijen M. A. W., Westfall K. B., Andersen D. R., Swaters R. A., 2011, *ApJ*, 739, L47
- Blais-Ouellette S., Amram P., Carignan C., Swaters R., 2004, *A&A*, 420, 147

- Bosma A., 1978, PhD thesis, PhD Thesis, Groningen Univ., (1978)
- Bosma A., 1981a, *AJ*, 86, 1791
- Bosma A., 1981b, *AJ*, 86, 1825
- Bottema R., Verheijen M. A. W., 2002, *A&A*, 388, 793
- Broeils A. H., 1992, PhD thesis, PhD thesis, Univ. Groningen, (1992)
- Broeils A. H., van Woerden H., 1994, *A&AS*, 107, 129
- Bundy K., et al., 2015, *ApJ*, 798, 7
- Cappellari M., et al., 2011, *MNRAS*, 413, 813
- Conselice C. J., 2003, *ApJS*, 147, 1
- Courteau S., Rix H.-W., 1999, *ApJ*, 513, 561
- Crain R. A., et al., 2015, *MNRAS*, 450, 1937
- Dicaire I., et al., 2008, *MNRAS*, 385, 553
- Eskew M., Zaritsky D., Meidt S., 2012, *AJ*, 143, 139
- Fabricius M. H., Saglia R. P., Fisher D. B., Drory N., Bender R., Hopp U., 2012, *ApJ*, 754, 67
- Fazio G. G., et al., 2004, *ApJS*, 154, 10
- Fisher D., 1997, *AJ*, 113, 950
- García-Lorenzo B., et al., 2015, *A&A*, 573, A59
- Helfer T. T., Thornley M. D., Regan M. W., Wong T., Sheth K., Vogel S. N., Blitz L., Bock D. C.-J., 2003, *ApJS*, 145, 259
- Hernandez O., Carignan C., Amram P., Chemin L., Daigle O., 2005, *MNRAS*, 360, 1201
- Ho L. C., Filippenko A. V., Sargent W. L. W., Peng C. Y., 1997, *ApJS*, 112, 391
- Jansen R. A., Franx M., Fabricant D., Caldwell N., 2000, *ApJS*, 126, 271
- Jore K. P., Broeils A. H., Haynes M. P., 1996, *AJ*, 112, 438
- Just A., Fuchs B., Jahreiß H., Flynn C., Dettbarn C., Rybizki J., 2015, *MNRAS*, 451, 149
- Karachentsev I. D., Makarov D. A., 1996, *AJ*, 111, 794
- Karachentsev I. D., Makarov D. I., Huchtmeier W. K., 1999, *A&AS*, 139, 97
- Kennicutt R. C., Evans N. J., 2012, *ARA&A*, 50, 531
- Kent S. M., 1985, *ApJS*, 59, 115
- Kent S. M., 1986, *AJ*, 91, 1301
- Laurikainen E., Salo H., Buta R., 2005, *MNRAS*, 362, 1319
- Lelli F., McGaugh S. S., Schombert J. M., 2016, *ApJ*, 816, L14
- Li H.-N., Wu H., Cao C., Zhu Y.-N., 2007, *AJ*, 134, 1315
- Maguire K., et al., 2012, *MNRAS*, 426, 2359
- Makarova L., Karachentsev I., Takalo L. O., Heinaemaeki P., Valtonen M., 1998, *A&AS*, 128, 459
- Markarian B. E., Oganessian E. Y., Arakelian S. N., 1965, *Astrofizika*, 1, 38
- Márquez I., Masegosa J., Moles M., Varela J., Bettoni D., Galletta G., 2002, *A&A*, 393, 389
- Martig M., Bournaud F., Croton D. J., Dekel A., Teyssier R., 2012, *ApJ*, 756, 26
- Martinsson T. P. K., Verheijen M. A. W., Westfall K. B., Bershadsky M. A., Andersen D. R., Swaters R. A., 2013, *A&A*, 557, A131
- McGaugh S. S., 2012, *AJ*, 143, 40
- McGaugh S. S., Schombert J. M., 2015a, *ApJ*, 802, 18
- McGaugh S. S., Schombert J. M., 2015b, *ApJ*, 802, 18
- McGaugh S. S., Schombert J. M., Bothun G. D., de Blok W. J. G., 2000, *ApJ*, 533, L99
- McMullin J. P., Waters B., Schiebel D., Young W., Golap K., 2007, in Shaw R. A., Hill F., Bell D. J., eds, *Astronomical Society of the Pacific Conference Series Vol. 376, Astronomical Data Analysis Software and Systems XVI*. p. 127
- Meidt S. E., et al., 2012, *ApJ*, 744, 17
- Meidt S. E., et al., 2014, *ApJ*, 788, 144
- Möllenhoff C., Heidt J., 2001, *A&A*, 368, 16
- Oke J. B., 1990, *AJ*, 99, 1621
- Oman K. A., et al., 2015, *MNRAS*, 452, 3650
- Ostriker J. P., Caldwell J. A. R., 1979, in Burton W. B., ed., *IAU Symposium Vol. 84, The Large-Scale Characteristics of the Galaxy*. pp 441–448
- Parodi B. R., Saha A., Sandage A., Tammann G. A., 2000, *ApJ*, 540, 634
- Persic M., Salucci P., Stel F., 1996, *MNRAS*, 281, 27
- Rekola R., Jerjen H., Flynn C., 2005, *A&A*, 437, 823
- Richards E. E., et al., 2015, *MNRAS*, 449, 3981
- Röck B., Vazdekis A., Peletier R. F., Knapen J. H., Falcón-Barroso J., 2015, *MNRAS*, 449, 2853
- Rubin V. C., Ford Jr. W. K., Thonnard N., Burstein D., 1982, *ApJ*, 261, 439
- Sanders R. H., 1996, *ApJ*, 473, 117
- Schaye J., et al., 2015, *MNRAS*, 446, 521
- Schlafly E. F., Finkbeiner D. P., 2011, *ApJ*, 737, 103
- Schneider S. E., Thuan T. X., Magri C., Wadiak J. E., 1990, *ApJS*, 72, 245
- Serra P., et al., 2012, *MNRAS*, 422, 1835
- Sheth K., Vogel S. N., Regan M. W., Thornley M. D., Teuben P. J., 2005, *ApJ*, 632, 217
- Sorce J. G., Tully R. B., Courtois H. M., Jarrett T. H., Neill J. D., Shaya E. J., 2014, *MNRAS*, 444, 527
- Spano M., Marcelin M., Amram P., Carignan C., Epinat B., Hernandez O., 2008, *MNRAS*, 383, 297
- Spekkens K., Sellwood J. A., 2007, *ApJ*, 664, 204
- Springel V., Frenk C. S., White S. D. M., 2006, *Nature*, 440, 1137
- Thean A. H. C., Mundell C. G., Pedlar A., Nicholson R. A., 1997, *MNRAS*, 290, 15
- Thornley M. D., Mundy L. G., 1997, *ApJ*, 484, 202
- Tonry J. L., Dressler A., Blakeslee J. P., Ajhar E. A., Fletcher A. B., Luppino G. A., Metzger M. R., Moore C. B., 2001, *ApJ*, 546, 681
- Verheijen M. A. W., 1997, PhD thesis, University of Groningen
- Verheijen M. A. W., Sancisi R., 2001, *A&A*, 370, 765
- Walter F., Brinks E., de Blok W. J. G., Bigiel F., Kennicutt Jr. R. C., Thornley M. D., Leroy A., 2008, *AJ*, 136, 2563
- Wong T., et al., 2013, *ApJ*, 777, L4
- Young J. S., et al., 1995, *ApJS*, 98, 219
- Young L. M., et al., 2011, *MNRAS*, 414, 940
- de Blok W. J. G., Bosma A., 2002, *A&A*, 385, 816
- de Blok W. J. G., Walter F., Brinks E., Trachternach C., Oh S.-H., Kennicutt Jr. R. C., 2008, *AJ*, 136, 2648
- de Vaucouleurs G., de Vaucouleurs A., Corwin Jr. H. G., Buta R. J., Paturel G., Fouqué P., 1991, *Third Reference Catalogue of Bright Galaxies*. Springer-Verlag, Berlin
- den Heijer M., et al., 2015, *A&A*, 581, A98
- van Albada T. S., Sancisi R., 1986, *Philosophical Transactions of the Royal Society of London Series A*, 320, 447
- van Zee L., Dale D. A., Barnes K. L., Staudaher S., Calzetti D., Dalcanton J. J., Bullock J. S., Chandar R., 2012, in *American Astronomical Society Meeting Abstracts* 220. p. 433.08
- van der Hulst J. M., Terlouw J. P., Begeman K. G., Zwitser W., Roelfsema P. R., 1992, in Worrall D. M., Biemesderfer C., Barnes J., eds, *Astronomical Society of the Pacific Conference Series Vol. 25, Astronomical Data Analysis Software and Systems I*. p. 131
- van der Hulst J. M., van Albada T. S., Sancisi R., 2001, in Hibbard J. E., Rupen M., van Gorkom J. H., eds, *Astronomical Society of the Pacific Conference Series Vol. 240, Gas and Galaxy Evolution*. p. 451
- van der Kruit P. C., Bosma A., 1978, *A&AS*, 34, 259

## APPENDIX A: NOTES ON INDIVIDUAL GALAXIES

In this section, we introduce each galaxy in the study and provide a brief description of notable attributes. Comparison



to other observations and analyses are discussed when available. Figs. A1-A16 present a summary of the observational data for each galaxy.

### A1 NGC 3486

New VLA HI observations of the SABc galaxy NGC 3486 presented in Fig. A1 show stream-like features extending from the northwest and southeast sides of the HI disc. These features are low column-density, but appear to follow the rotation curve of the disc. There is no obvious nearby companion or signature of a recent merger. In the central region, the HI mass surface density shows a depression in the central 40 arcsec, then remains constant before decreasing exponentially at  $\sim 180$  arcsec. The molecular gas distribution is confined to the central 40 arcsec, but is only dominant within 6 arcsec, as inferred from a CO map from the CARMA STING survey.

The neutral gas velocity field of NGC 3486 displays outer S-shaped contours characteristic of kinematic warps caused by a change in position and/or inclination angle (e.g. M83; Bosma 1981b). In the case of NGC 3486, kinematic models with a changing position and inclination angle best match this outer warp. The ionized gas velocity field reveals solid-body rotation in the inner 30 arcsec (Fig. 3). The outer HI rotation curve between 100-200 arcsec displays a wiggle likely due to the warp noted in the velocity field (Fig. 4). Broeils & van Woerden (1994) observed NGC 3486 with the WSRT and noted similar structure in its position-velocity diagram.

The stellar light in NGC 3486 is mostly disc-dominated, with a slight contribution from both a bulge and bar component. There is some evidence of a small downbending in the NIR surface brightness profile at the  $R_{25}$ , which also corresponds to a drop in  $\log_{10}(\text{EW})$ . The radial trend in  $\log_{10}(\text{EW})$  is inversely correlated with the  $B - R$  colour, quickly rising from small EW in the centre 20 arcsec to a larger constant EW value across the disc. Although NGC 3486 has a relatively small total SFR of just  $0.50 \pm 0.36 M_{\odot} \text{ yr}^{-1}$ , it has a large EW of  $38.2 \pm 3.3 \text{ \AA}$ , indicating that the current SFR is greater than the past average SFR.

The rotation curve decomposition analysis was done using estimates of the baryonic components from the stellar disc surface density and a combination of the HI and CO for the total gas mass surface density (Fig. 5). The baryonic contribution to the total observed rotation curve is stellar disc dominated at inner radii, while the gas contribution grows reaching a peak near 200 arcsec. The fixed  $M/L = 0.5$  decomposition requires a dark matter halo model rotation curve which is the dominant contributor to the observed rotation curve at most radii. The total best-fitting rotation curve does not follow the wiggles in the observed rotation curve, which is expected assuming the structure is influenced by forces other than the gravitational potential. The maximum disc assumption for this galaxy implies a much greater contribution from the stellar disc with a  $M/L$  of 1.0. This results in a baryon mass fraction at  $2.2h_R$  which differs by a factor of two between the fixed  $M/L$  and maximum disc decompositions methods.

### A2 NGC 3675

Archival VLA observations of this SAb galaxy shown in Fig. A2 reveal an HI disc 10 arcmin in diameter measured at  $10^{20} \text{ atoms cm}^{-2}$  with patchy diffuse emission that extends out to a diameter of 21.5 arcmin. There appears to be a gap between the main HI disc and this outer diffuse neutral gas ring. There is no obvious extended diffuse stellar light at  $3.6\mu\text{m}$  to match the extended component of the HI disc. The main HI disc features two dense clumps of HI emission directly north and south of the galaxy's nucleus. NGC 3675 was observed by Broeils & van Woerden (1994) with the WSRT, but the observations were low signal-to-noise and did not detect the diffuse HI ring. The HI mass surface density remains roughly constant in the inner 80 arcsec before slowly decreasing. The molecular gas distribution dominates over the HI gas within radii less than 100 arcsec, based on CO emission detected in four pointings out to a radius of 135 arcsec in the FCRAO survey.

The neutral gas kinematics in Fig. 4 show a flat rotation curve with a slight warp in the outer disc at a radius of  $\sim 120$  arcsec that can be modeled as a change in position angle. Although the diffuse outer ring appears to follow the rotation curve of the galaxy, it was not included in the mass decomposition analysis. The ionized gas rotation curve rises more steeply than the HI derived rotation curve in the centre 20 arcsec, an effect that can be attributed to beam smearing in the lower resolution HI data. The ionized gas rotation curve peaks at a velocity of  $193 \text{ km s}^{-1}$  at a radius of 25 arcsec before turning over and decreasing out to 40 arcsec, where it joins the HI rotation curve.

The distribution of stellar light in NGC 3675 is primarily disc-like with a small pseudo-bulge component with a radius of 8.5 arcsec (Fabricius et al. 2012). There is no strong colour gradient; the  $B - R$  colour remains fairly constant at about 1.44, which is normal for an intermediate type spiral galaxy (Jansen et al. 2000). NGC 3675 has a large roughly constant EW value within 80 arcsec which declines before leveling out again around 120 arcsec. The small star formation rate is consistent with the relatively little amount of H $\alpha$  emission visible in the narrowband image.

The stellar contribution to the total observed rotation curve was modeled using a disc only stellar light distribution with a  $M/L = 0.5$  as shown in Fig. 5. The model rotation curve for this stellar disc rises steeply in the inner 20 arcsec like the ionized gas rotation curve, but then the slope appears to flatten out slightly before reaching a peak velocity at 80 arcsec. This unusual feature could be attributed to dust extinction near the centre within NGC 3675 (Möllenhoff & Heidt 2001). The shape of the observed ionized and neutral gas rotation curve mimics the shape of the model stellar disc rotation curve, and is well-described by the maximum disc model with  $M/L = 0.7$ .

### A3 NGC 3726

NGC 3726 is an SABc galaxy in the Ursa Major cluster. HI synthesis data from the WHISP survey displayed in Fig. A3 shows that the neutral gas is distributed in a ring-like structure with decreasing column density towards the centre. There are hints of extended diffuse gas to the north (approaching side) and south (receding side) along the major



axis. The HI velocity field and isovelocity contours hint that the outer disc may be warped. This warp manifests itself as a dip in the rotation curve around 180 arcsec, which doesn't seem to be well-modeled by the baryonic contributions (Fig. 5). This can also be seen in the decompositions in Verheijen (1997) using WSRT observations. The kinematic signature of a bar can be observed in the S-shaped contours in the ionized gas velocity field from SparsePak (Fig. 3). The ionized gas rotation curve and full rotation curve decomposition agrees well with that presented in Spano et al. (2008) from Fabry-Perot H $\alpha$  observations.

The 3.6 $\mu$ m surface brightness profile of NGC 3726 shows that the bulge component is relatively small and does not contribute greatly to the total light distribution. The shape of the surface brightness profile at radii within  $\sim 50$  arcsec displays a dip in brightness, reflecting the presence of a ring-like structure in the stellar component (see the bottom left panel in Fig. A3). Beyond the ring, the disc light decreases exponentially with a corresponding flattening of the  $B - R$  colour and log(EW) profiles.

The observed ionized and neutral gas rotation curve was decomposed using a total gas contribution which includes CO observations for the molecular gas and a stellar disc M/L = 0.5 using the 3.6 $\mu$ m stellar disc distribution. In this case, CO observations from the FCRAO survey were used in place of the BIMA SONG map to better recover spatially extended flux. The maximum disc decomposition results in a disc M/L = 1.1 and a stellar disc model rotation curve which accounts for 95 per cent of the observed potential at 2.2 disc scale lengths versus 46 per cent for the fixed M/L = 0.5 model. This is one of the largest discrepancies between the fixed M/L and maximum disc models for this sample.

#### A4 NGC 3941

NGC 3941 is a barred S0 galaxy with a known counterrotating gas disc relative to the stellar rotation (Fisher 1997). The low velocity dispersion of this gas disc as measured by Fisher (1997) implies it has settled into an equilibrium distribution despite having a likely origin due to a merger event or accretion of gas with oppositely directed angular momentum. Indeed, the neutral gas appears to have settled in a disc, although it is not a cohesive structure (Fig. A4). NGC 3941 is known to have a complex inner structure involving an inner disc with spiral arms and bar with an oval distortion (Laurikainen et al. 2005). There is no HI detected in the central 40 arcsec, which is a common feature of barred galaxies in this sample. The ionized gas emission detected with SparsePak only fills the inner 25 arcsec. NGC 3941 was also observed with the WSRT as part of the ATLAS<sup>3D</sup> survey. Serra et al. (2012) found a similar distribution of neutral gas and velocity field.

The average rotation curve derived from the ionized gas velocity field agrees with that derived by Fisher (1997), reaching a peak velocity near 15 arcsec before falling back down to lower velocities. The neutral gas rotation curve picks up where the ionized gas left off and bends upwards out to the last measured point at 210 arcsec.

The stellar light in NGC 3941 is best modeled as a bulge-like distribution with a slight break at a radius of 132 arcsec where the high surface brightness component ends. The colour and EW radial trends are remarkably flat, with

only a slight increase in EW in the central  $\sim 20$  arcsec where there is the most ionized gas emission.

Given the unusual shape of its rotation curve, it is possible that the neutral gas in NGC 3941 is not tracing the gravitational potential. An attempt was made to decompose the rotation curve into separate mass components, anyways. Fig. 5 shows the decomposition assuming a bulge distribution for the stellar component with the bulge M/L fixed to 0.4. NGC 3941 is one of two cases in the present sample where the fixed M/L model over-estimates the observed rotation curve. The maximum M/L that the stellar bulge can have without over-shooting the peak ionized gas velocity is 0.3. In both cases, the model total rotation curve provides a poor fit to the observed rotation curve, particularly between 25-150 arcsec, causing the baryon mass fraction at  $2.2h_R$  to be  $>1$ . A distance of 12.2 Mpc estimated from surface brightness fluctuations (Tonry et al. 2001) is adopted for NGC 3941. It is difficult to compare this distance to the one estimated from the LTFR due to the lack of a suitable radial range to measure  $V_{\text{flat}}$ .

#### A5 NGC 3953

NGC 3953 is an SBbc galaxy in the Ursa Major cluster. Although, one of the most massive galaxies in the Ursa Major cluster and in the present sample, it is relatively deficient of HI. The neutral gas does not extend much beyond the stellar disc, and the surface density decreases towards the centre where there is a prominent bar visible in the H $\alpha$  image in Fig. A5. The archival VLA observations did not have a bandpass wide enough to include the full velocity range of NGC 3953, as is evident in the HI figures. The receding side of the galaxy is missing about 77 km s<sup>-1</sup>, or 15 channels at a velocity resolution of 5.2 km s<sup>-1</sup>. This corresponds to approximately 35 per cent of the velocity coverage of the receding side, assuming  $W_{20} = 441.9$  km s<sup>-1</sup> (Verheijen & Sancisi 2001). Despite this, the archival VLA data have significantly higher S/N than the WHISP data in which NGC 3953 was detected beyond WSRT's primary beam half-power width. Previous study of atomic gas in NGC 3953 by Verheijen & Sancisi (2001) shows that both the distribution and kinematics of the HI are symmetric. Therefore, we use the rotation curve and gas distribution derived from the approaching side only as indicative of the global rotation curve and HI mass surface density distribution. Values for the integrated HI flux density,  $W_{20}$ , diameter of the HI disc, dynamical centre and systemic velocity are all adopted from Verheijen & Sancisi (2001). A dashed ellipse indicating the full diameter of the HI disc is overlaid on the HI figures in Fig. A5 for reference.

Fig. 2 shows that the ionized gas emission observed in the SparsePak field of view for NGC 3953 is largely from a bar-like feature. The signature S-shaped isovelocity contours from the bar dynamics can be observed in the ionized gas velocity field in Fig. 3 and in the H $\alpha$  velocity field of Hernandez et al. (2005). The rotation curve derived from the ionized gas shows a steep inner rise followed by a plateau at 180 km s<sup>-1</sup> (Fig. 4). The rotation curve derived from the approaching side of the HI velocity field agrees well with Verheijen & Sancisi (2001).

The shape of the ionized gas rotation curve is somewhat reproduced in the model baryonic rotation curve compo-

nents (Fig. 5). The steep rise and plateau can be described by a combination of a broad bulge component and slowly rising disc model rotation curve both with fixed  $M/L = 0.5$ . An equally good fit to the observed rotation curve can be achieved by maximizing the disc contribution with a  $M/L = 0.7$ . The bulge contribution appears to be maximal at  $M/L = 0.5$ . The model rotation curve for the gas includes a contribution from molecular gas estimated from FCRAO observations. The mass at 2.2 disc scale lengths is baryon-dominated in both the fixed  $M/L$  and maximum disc/bulge decomposition models.

## A6 NGC 3972

NGC 3972 is an SAbc galaxy detected in the same field of view as NGC 3998 in new VLA HI observations. Although NGC 3972 lies beyond the primary beam half-power radius, the recovered integrated flux is comparable to that in Verheijen & Sancisi (2001). The HI morphology matches the stellar morphology and appears as a highly inclined disc (Fig. A6). The approaching (east) side has a higher column density of neutral gas as well as a higher density of star formation as seen in the narrowband  $H\alpha$  image. The straight isovelocity contours in the HI velocity field indicate solid body rotation, and the derived rotation curve in Fig. 4 shows as much.

Fig. 5 shows the rotation curve decomposition. The model baryonic rotational velocities turn over and begin to decrease at a radius of about 80 arcsec, whereas the observed rotation curve is still rising at the last measured point. The stellar disc is maximal at a  $M/L$  of 0.6 to avoid over-estimating the inner rotation velocities. It is possible that the slope of the inner rotation curve appears shallow due to the effect of beam smearing. In this case, the stellar disc could be maximized further. The estimated LTFR distance of 22.2 Mpc is in close agreement with the adopted SNIa distance of 25.2 Mpc (Maguire et al. 2012).

## A7 NGC 3992

NGC 3992 is a strongly barred Sbc galaxy with prominent spiral features visible in the stellar disc. The archival VLA HI observations reveal a complete absence of detectable neutral gas within the central 80 arcsec – about the length of the bar (Fig. A7). Even the narrowband  $H\alpha$  image shows little ionized gas emission around the bar. Likewise, Helfer et al. (2003) find a remarkable lack of molecular gas in the central region. Beyond the bar, the HI disc has approximately the same radial extent as the high surface brightness stellar disc observed at  $3.6\mu\text{m}$ . Three dwarf galaxies, UGC 06969, UGC 06940, and UGC 06923, are also detected in the HI data. Properties of these galaxies and other known companions to NGC 3992 are presented in Table A1.

The outer kinematics of the neutral gas disc in NGC 3992 are regular with only a slight warp at the outermost radii. The resultant HI rotation curve is relatively flat, but appears to decrease at radii greater than 220 arcsec. This same decrease was observed by Bottema & Verheijen (2002), although they trace the HI distribution out to larger radii than the present data. The inner kinematics as measured by the ionized gas emission are affected by the strong

bar (Fig. 3). The rotational velocities derived from the ionized gas shown in Fig. 4 increase from the centre up to the neutral gas rotational velocities, but display a kink between  $\sim 40$ – $60$  arcsec which can most likely be attributed to the bar. A similar structure can be seen in the  $H\alpha$  position velocity diagram of Hernandez et al. (2005).

The stellar distribution of NGC 3992 is disc dominated, but with contributions from bulge and bar components. Decomposition of the  $3.6\mu\text{m}$  image with DISKFIT (Spekkens & Sellwood 2007) revealed that the bulge contributes less than 5 per cent to the total luminosity. At larger radii, the  $3.6\mu\text{m}$  surface brightness profile shows a change in slope around  $\sim 250$  arcsec where the high surface brightness disc component ends. The colour gradient appears flat across radii within  $R_{25}$ , but then slowly increases out to larger radii. The EW distribution, on the other hand, shows a sharp increase beyond the bar at the start of the star forming disc near 80 arcsec.

The rotation curve decomposition analysis was carried out using neutral gas and stellar disc components for the baryonic contributions to the overall observed rotation curve and is presented in Fig. 5. The structure in the ionized gas rotational velocities is reproduced in the stellar disc contribution, likely due to the influence of the bar. The lack of detectable atomic or molecular gas in the centre results in negative rotational velocities within 140 arcsec for the gas component. We adopt the Type Ia supernova distance of 22.7 Mpc (Parodi et al. 2000) for this galaxy. The LTFR distance is considerably larger at 36.4 Mpc using a value for  $V_{\text{flat}}$  estimated from an intermediate radial range which avoids the downbending portion of the outer warped rotation curve. The dark matter halo model rises rapidly in the fixed  $M/L = 0.5$  decomposition resulting in a small transition radius and, therefore, mass distribution which is dark matter-dominated at nearly all measured radii. The decomposition presented here agrees well with the best-fitting stellar disc only decomposition presented in Bottema & Verheijen (2002). The maximum disc decomposition with  $M/L = 0.8$  provides an equally reasonable fit to the observed rotation curve. The mass distribution derived from the maximum disc model is quite different and does not become dark matter-dominated until over 6 disc scale lengths.

**Table A1.** Properties of Known Companions to NGC 3992

Galaxy	RA, Dec (J2000)	Systemic <sup>a</sup> Velocity (km s <sup>-1</sup> )	Angular Separation (arcmin)	Physical <sup>b</sup> Separation (kpc)	Size <sup>c</sup> (a×b) (arcsec×arcsec)	Position Angle (deg)	$m_B$	$m_R$	$m_{3.6}$	$(B - R)_0$	$M_B$ <sup>b</sup>	HI Flux (Jy km s <sup>-1</sup> )
UGC 06940	11:57:48.0,+53:14:03	1113(1)	8.58	56.7	70.0×35.6	-39.6	16.27±0.04	15.59±0.04	13.62±0.13	0.64±0.05	-15.61±0.04	2.5
SDSS J115834.34+532043.6	11:58:34.4,+53:20:44	1150(2)	8.88	58.6	101.2×62.2	76.3	17.27±0.11	16.05±0.11	13.97±0.15	1.17±0.16	-14.62±0.11	-
UGC 06969	11:58:46.8,+53:25:31	1115(1)	11.10	73.3	124.6×67.2	-34.1	15.07±0.03	14.23±0.03	12.13±0.06	0.80±0.05	-16.82±0.03	6.2
UGC 06923	11:56:49.7,+53:09:37	1069(1)	14.61	96.5	163.2×71.1	-13.2	13.90±0.02	12.96±0.02	10.78±0.04	0.90±0.03	-17.99±0.02	11.4

*Note.* – The apparent magnitudes are measured values and are not corrected for extinction.  $B - R$  and  $M_B$  are extinction corrected assuming  $A_B=0.106$  and  $A_R=0.063$  (Schlafly & Finkbeiner 2011). The extinction correction for the NIR is assumed to be negligible.

<sup>a</sup> Sources: (1) this work; (2) Sloan Digital Sky Survey Data Release 2.

<sup>b</sup> Assuming a distance of 22.7 Mpc.

<sup>c</sup> Sizes indicate the diameters in arcseconds of the apertures used to measure the reported magnitudes.

**A8 NGC 3998**

NGC 3998 is a non-barred S0 and well-studied low-ionization nuclear emission-line region (LINER) galaxy in a relatively populated group. In addition to NGC 3998, four other galaxies are detected in the new HI observations from the VLA including NGC 3972, NGC 3982, UGC 06919, and UGC 06988. Table A2 presents properties of the known companions to NGC 3998. The neutral gas in NGC 3998 is diffuse and not well organized. Fig. A8 shows that it lies in a roughly disc-like distribution with an apparent position angle that is perpendicular to the position angle of the stellar distribution. Serra et al. (2012) observed NGC 3998 with the WSRT as part of the ATLAS<sup>3D</sup> survey and noted the same lopsided and misaligned morphology of the HI. Their HI map displays a similar distribution of HI as we observed with the VLA, with two distinct HI emission components on the approaching side to the west and south of the primary HI disc. The ionized gas velocity field in Fig. 3 indicates that the ionized gas shares the same orientation as the HI. However, the ionized gas shows a steeper rise and greater peak rotational velocities than the neutral gas (see Fig. 4). In addition, the ionized gas emission lines in the SparsePak spectra display broad FWHM values and non-thermal emission line flux ratios. Fisher (1997) found that the velocity dispersion profiles of both the gas and stars in NGC 3998 rise sharply towards the centre, reaching values near  $320 \text{ km s}^{-1}$ .

Moving beyond the centre, we find a bulge-like stellar distribution in the  $3.6\mu\text{m}$  surface brightness profile. Therefore, a spherical distribution was adopted for the model stellar rotation curve. This model stellar bulge rotation curve falls off too quickly to accurately describe the observed ionized gas rotation curve in the decomposition analysis (Fig. 5). The decomposition does, however, adequately fit the outer HI rotation curve points. Model stellar rotation curves using a bulge and disc as well as disc only distributions were tried, but were unable to fit both the inner and outer observed rotational velocities concurrently. The stellar bulge rotation curve model requires a  $M/L = 1.4$  in order to match the large rotational velocities of the ionized gas in the inner 40 arcsec at the adopted distance of 14.1 Mpc derived from surface brightness fluctuations (Tonry et al. 2001). The LTFR distance estimate is more than double at 30.1 Mpc based on  $V_{\text{flat}}$  measured from the HI rotational velocities. A decomposition using a fixed bulge  $M/L = 0.6$  can adequately describe the HI rotation curve, but not the ionized gas. It is possible that the ionized gas is not in gravitational equilibrium and cannot be described by the model rotation curves.



**Table A2.** Properties of Known Companions to NGC 3998

Galaxy	RA, Dec (J2000)	Systemic <sup>a</sup> Velocity (km s <sup>-1</sup> )	Angular Separation (arcmin)	Physical <sup>b</sup> Separation (kpc)	Size <sup>c</sup> (a × b) (arcsec × arcsec)	Position Angle (deg)	$m_B$	$m_R$	$m_{3.6}$	$(B - R)_0$	$M_B$ <sup>b</sup>	HI Flux (Jy km s <sup>-1</sup> )
NGC3990	11:57:35.4,+55:27:33	696(1)	2.93	12.0	110.1×92.2	28.9	13.57±0.02	12.10±0.02	9.39±0.02	1.45±0.03	-17.24±0.02	-
SDSS J115813.68+552316.5	11:58:13.6,+55:23:18	966(2)	4.66	19.1	90.3×58.7	-48.5	16.61±0.06	15.41±0.06	13.03±0.10	1.18±0.09	-14.19±0.06	-
SDSS J115701.86+552511.1	11:57:01.6,+55:25:11	1215(2)	7.96	32.6	87.2×55.8	-85.5	16.53±0.05	15.37±0.05	13.19±0.10	1.14±0.08	-14.27±0.05	-
SDSS J115703.08+553612.3	11:57:03.0,+55:35:14	763(2)	10.97	45.0	62.4×38.7	-49.6	16.88±0.04	15.72±0.04	13.67±0.13	1.14±0.06	-13.92±0.04	-
SDSS J115849.17+551824.7	11:58:49.2,+55:18:25	939(2)	11.59	47.5	93.7×76.1	-43.7	16.91±0.10	15.69±0.10	13.41±0.11	1.19±0.15	-13.90±0.10	-
UGC06919	11:56:37.6,+55:37:58	1283(2)	15.49	63.5	137.4×50.3	85.8	15.19±0.02	13.85±0.02	—	1.32±0.04	-15.61±0.02	0.4
UGC 06988	11:59:51.7,+55:39:55	745(3)	20.70	84.9	—	—	—	—	—	—	—	3.2
NGC3982	11:56:28.1,+55:07:31	1102(3)	23.35	95.8	175.3×172.0	68.2	12.20±0.02	11.18±0.02	—	1.01±0.03	-18.60±0.02	30.9
SDSS J115356.95+551017.3	11:53:57.0,+55:10:16	1249(2)	38.01	155.9	38.2×29.6	9.2	17.79±0.04	16.65±0.04	—	1.11±0.06	-13.02±0.04	-

*Note.* – The apparent magnitudes are measured values and are not corrected for extinction.  $B - R$  and  $M_B$  are extinction corrected assuming  $A_B=0.059$  and  $A_R=0.036$  (Schlafly & Finkbeiner 2011). The extinction correction for the NIR is assumed to be negligible.

<sup>a</sup> Sources: (1) RC3 (de Vaucouleurs et al. 1991); (2) Sloan Digital Sky Survey Data Release 3; (3) this work.

<sup>b</sup> Assuming a distance of 14.1 Mpc.

<sup>c</sup> Sizes indicate the diameters in arcseconds of the apertures used to measure the reported magnitudes.

### A9 NGC 4051

NGC 4051 is an SABbc galaxy and well-studied AGN. HI synthesis observations from WHISP show gas distributed in a ring around a central hole where the active nucleus lies (Fig. A9). The neutral gas morphology is similar to the ionized gas seen in the narrowband H $\alpha$  image which displays a bright central nucleus and two star-forming spiral arms wrapped around the centre. The radial distribution of  $B-R$  colour reveals the central concentration to be redder than the star-forming disc. The EW gradient matches this interpretation with small values in the centre and higher in the disc. The ionized gas velocity field in Fig. 3 shows twisted isovelocity contours indicating that it is likely being influenced by the nuclear activity or possible presence of a bar. As a result, the ionized gas rotation curve is uncertain and displays structure that cannot be described by the model rotation curves in the decomposition. The HI rotation curve rises slowly and flattens out around 120 arcsec.

The rotation curve decomposition using a disc only stellar distribution is shown in Fig. 5. The total gas contribution to the observed rotation curve includes CO observations for the molecular gas from the FCRAO survey, which were used in place of the BIMA SONG map to better recover spatially extended flux. The stellar disc model rotation curve has an unusual shape with a sharp peak at 10 arcsec followed by a downwards dip before rising and then turning over again. The sharp peak is likely due to the bright central nucleus. The combination of the complex distribution of stellar light and ionized gas rotation curve makes it difficult to constrain the stellar M/L in the maximum disc scenario. However, it appears that a stellar disc M/L greater than 0.5 will over-estimate the first few HI rotation curve points beyond the errors. The mass distribution in NGC 4051 is baryon-dominated until at least the last measured point.

### A10 NGC 4138

NGC 4138 is an SA0 galaxy in the Ursa Major cluster. The kinematics and distribution of mass in NGC 4138 have been studied extensively using HI synthesis observations from both the WSRT (Verheijen & Sancisi 2001) and VLA (Jore et al. 1996). The HI observations presented in Fig. A10 are taken from Jore et al. (1996). In Jore et al. (1996), they derive two rotation curves: one which rapidly declines (more so than is typically observed) and one which they fix to be flat, which then implies a strong outer warp with a decreasing inclination angle. It's not possible to confirm which model is correct based on the velocity field, but the diffuse minor axis gas appears as if it has face-on orbits, which supports the possibility of a smaller inclination angle at large radii. In the present analysis, we did not fix the rotation curve to be flat, but we used the results of Jore et al. (1996) to force the inclination angle to decrease (see Fig. 4).

Jore et al. (1996) additionally acquired optical spectroscopic observations of NGC 4138 and discovered a counter-rotating stellar disc which appears to coincide with the ring of H $\alpha$  emission visible in Fig. A10. Ionized gas kinematics were additionally derived from the spectroscopic observations and used to constrain rotational velocities in the central 40 arcsec. The ionized gas velocity field (Fig. 3) and rotation curve presented here agree well with the results of

Jore et al. (1996) and appear to match the neutral gas rotational velocities (Fig. 4).

The flat rotation curve can be described easily by the baryonic and dark matter halo contributions as shown in Fig. 5. The gas model rotation curve includes an estimate of the molecular gas from a single pointing CO observation in the FCRAO survey. The stellar distribution measured at  $3.6\mu\text{m}$  is well-described by a disc only component. Assuming a fixed stellar disc M/L = 0.5 results in a distribution of mass that is dark matter-dominated beyond about one disc scale length. The flat rotation curve can be fit just as easily by maximizing the stellar disc contribution with M/L = 1.1. This pushes the transition radius out to almost 5 disc scale lengths. NGC 4138 is another case where the LTFR distance of 28.4 Mpc is significantly larger than the adopted surface brightness fluctuation distance of 13.8 (Tonry et al. 2001). The value of  $V_{\text{flat}}$  is uncertain in this case since it was essentially forced to the adopted value, so it is not necessarily surprising if the exact value is incorrect. The relative differences between the fixed M/L and maximum disc decomposition results are still valid.

### A11 NGC 4389

NGC 4389 is an SBbc galaxy in the Ursa Major cluster. The distribution of the H $\alpha$  emission and of the HI from new VLA observations shown in Fig. A11 suggests that the morphology is dominated by a bar. The rotation curves derived from the ionized and neutral gas suggest that the kinematics are also dominated by this bar (Fig. 4). Verheijen & Sancisi (2001) came to the same conclusion using WSRT observations of the HI. The observations presented here trace the neutral gas out to a larger radius than Verheijen & Sancisi (2001), but show a similar slowly rising rotation curve which only reaches maximum rotational velocities near  $100 \text{ km s}^{-1}$ .

A rotation curve for NGC 4389 has also been derived by Márquez et al. (2002) using the distribution of H II regions. They find a slowly rising rotation curve which has a peak velocity around  $90 \text{ km s}^{-1}$  at the last measured point near 60 arcsec. This is in excellent agreement with both the ionized and neutral gas rotation curves derived in the present study.

The stellar distribution in NGC 4389 displays a change in slope around 45 arcsec where the stellar light begins to drop off more quickly. This corresponds to the radius of the ring-like emission which emanates from the ends of the bar, as can be seen in the H $\alpha$  and high surface brightness  $3.6\mu\text{m}$  images. This sharp transition is reflected in the stellar contribution to the observed rotation curve in Fig. 5. The rotation curve derived from the distribution of the HI gas displays the same feature, indicating that the morphology of both the gas and stars is indeed dominated by the bar.

The structure in the distribution of the gas and stars caused by the prominent bar means the mass distribution in NGC 4389 would need to be dominated by dark matter at almost all radii in order to produce a smooth, slowly rising rotation curve. A M/L larger than 0.1 introduces too much structure into the total rotation curve to describe the observed one, as can be observed in the fixed M/L = 0.4 decomposition shown in Fig. 5. It is likely that the gas dynamics are being influenced by the presence of the bar. It is not straightforward to interpret the results of the rotation curve decomposition in the context of a bar potential.

### A12 UGC 07639

UGC 07639 is an irregular dwarf galaxy with very little HI detected in new VLA observations (Fig. A12). The HI is actually distributed off-centre and nearly perpendicular to the stellar distribution in the  $3.6\mu\text{m}$  image. Furthermore, the HI velocity field appears disorganized with only a hint of circular rotation. UGC 07639 was not targeted for SparsePak ionized gas observations due to the lack of visible  $\text{H}\alpha$  emission in the narrowband image. The stellar distribution at  $3.6\mu\text{m}$  is purely exponential, which is typical for dwarf galaxies. However, the integrated  $(B - R)_0$  colour of 0.86 is somewhat redder than for typical Im type galaxies (Jansen et al. 2000), which is consistent with the lack of recent star formation activity.

An attempt was made to extract a rotation curve from the velocity field and to decompose it into separate mass components. The rotation curve was found to be linearly rising out to 50 arcsec and only reaching a velocity of about  $20 \text{ km s}^{-1}$ . Such small rotational velocities could be described entirely by the total baryonic contribution alone without the need for dark matter. The addition of a dark matter halo model causes the total modeled rotation curve to over estimate the observed velocities at all inner radii. This results in an unexpected (and likely unreasonable) scenario where a dwarf galaxy is baryon-dominated at all measured radii.

To make matters worse, an unrealistically small stellar M/L must be assumed to prevent the total baryonic contribution from drastically over estimating the observed rotation curve, even without the presence of dark matter. We have adopted the distance of 7.1 Mpc estimated from surface brightness fluctuations (Rekola et al. 2005). Other literature distance estimates to UGC 07639 only vary by  $\lesssim 2$  Mpc (e.g. Makarova et al. 1998; Karachentsev & Makarov 1996), so it is not likely that the unphysical stellar M/L is due to incorrect normalization of the baryonic contributions caused by inaccurate distance estimates. Given the morphology of the gas and somewhat chaotic appearance of the velocity field, it is likely the gas is dynamically unstable and is not tracing the gravitational potential of the galaxy. For these reasons, we do not include UGC 07639 in the discussion of the results.

### A13 NGC 5033

NGC 5033 is a massive SAc galaxy whose kinematics have been well-studied in the literature. The HI data presented in Fig. A13 were processed from archival VLA observations which were originally published in Thean et al. (1997). Two dwarf companion galaxies, UGC 08314 and UGC 08303, are also detected in these observations (see Table A3). The distribution of HI in NGC 5033 displays a lot of structure. In general, regions of greater HI surface density correspond to regions with strong  $\text{H}\alpha$  emission, which is mostly in the centre and along the spiral arms. The HI velocity field of NGC 5033 is well-ordered with no signatures of barred or non-circular orbits in the centre. The outer isovelocity contours along the major axis deviate away from the line of nodes forming an S-shape which is the canonical sign of an outer disc warp. The smaller wiggles in the disc are likely due to streaming motions along the spiral arms.

van der Kruit & Bosma (1978) and Bosma (1981a) were the first to perform an in-depth study of the emission line and HI kinematics in NGC 5033. Bosma (1981a) was able to model the warped outer disc using a changing position angle. The results in Thean et al. (1997) and shown in Fig. 4 agree well with Bosma (1981a). The ionized gas velocity in Fig. 3 confirm the well-behaved central gas kinematics seen in the HI. The rotation curve derived from the ionized gas velocity field rises more steeply than the HI rotation curve and peaks near  $230 \text{ km s}^{-1}$  at 35 arcsec before coming back down. The shape of the ionized gas rotational velocities derived here are in agreement with those presented in Dicaire et al. (2008) within the central 60 arcsec.

The shape of the ionized and neutral gas rotation curves are well-described by the distributions of the baryonic components as demonstrated in Fig. 5. CO observations from BIMA SONG (Helfer et al. 2003) were included in the total gas estimate to account for the considerable amount of molecular gas in NGC 5033. The stellar distribution was decomposed into bulge and disc components using DISKFIT (Spekkens & Sellwood 2007). The contributions from both the stellar bulge and disc are maximal at M/L = 0.4. The mass distribution transitions from baryon-dominated to dark matter-dominated at  $2.2h_R$ .

**Table A3.** Properties of Known Companions to NGC 5033

Galaxy	RA, Dec (J2000)	Systemic <sup>a</sup> Velocity (km s <sup>-1</sup> )	Angular Separation (arcmin)	Physical <sup>b</sup> Separation (kpc)	Size <sup>c</sup> (a × b) (arcsec × arcsec)	Position Angle (deg)	$m_B$	$m_R$	$m_{3.6}$	$(B - R)_0$	$M_B$ <sup>b</sup>	HI Flux (Jy km s <sup>-1</sup> )
SDSS J131420.58+363407.9	13:14:20.8,+36:34:13	1737(1) <sup>d</sup>	10.77	58.9	66.9 × 48.4	22.7	17.08 ± 0.07	16.40 ± 0.07	14.32 ± 0.17	0.67 ± 0.10	-14.29 ± 0.07	0.6
UGC08314	13:14:00.6,+36:19:01	935(2)	17.83	97.5	106.0 × 82.0	52.1	15.93 ± 0.06	15.12 ± 0.06	13.13 ± 0.10	0.79 ± 0.08	-15.44 ± 0.06	2.9
SDSS J131152.03+362858.2	13:11:52.0,+36:28:58	—	20.31	111	—	—	—	—	—	—	—	2.5
UGC08303	13:13:18.3,+36:12:35	945(3)	22.67	124	183.4 × 155.0	-102.5	13.73 ± 0.03	12.96 ± 0.03	10.87 ± 0.04	0.76 ± 0.05	-17.64 ± 0.03	14.0

*Note.* — The apparent magnitudes are measured values and are not corrected for extinction.  $B - R$  and  $M_B$  are extinction corrected assuming  $A_B=0.042$  and  $A_R=0.025$  (Schlafly & Finkbeiner 2011). The extinction correction for the NIR is assumed to be negligible.

<sup>a</sup> Sources: (1) Sloan Digital Sky Survey Data Release 6; (2) Schneider et al. (1990); (3) this work.

<sup>b</sup> Assuming a distance of 18.8 Mpc.

<sup>c</sup> Sizes indicate the diameters in arcseconds of the apertures used to measure the reported magnitudes.

<sup>d</sup> SDSS DR12 provides an updated measurement of  $z=0.00405$  ( $v=1215$  km s<sup>-1</sup>), which is consistent with the velocity range in which this galaxy is detected in the HI data.



## A14 NGC 5055

NGC 5055 (M63) is a well-studied, massive SAbc galaxy. Archival VLA observations originally published in [Thornley & Mundy \(1997\)](#) are presented in Fig. A14. The distribution of neutral gas follows the distribution of the stellar light, but appears to change position angle slightly beyond the stellar disc. This is more apparent in the HI velocity field where the isovelocity contours become distorted in the outer disc, especially along the major axis. Deviations from circular motion within the stellar disc are likely due to streaming motions along the spiral arms ([Thornley & Mundy 1997](#)). The dwarf companion galaxy UGC 08313 to the northwest of NGC 5055 is detected in the  $3.6\mu\text{m}$  image and the HI observations (see Table A4). CO observations from BIMA SONG ([Helfer et al. 2003](#)) display a strong central concentration surrounded by more diffuse emission which closely follows the distribution of  $\text{H}\alpha$  emission.

The central ionized gas kinematics in the SparsePak velocity field (Fig. 3) do not show any clear deviations from circular motion. The derived ionized gas rotation curve peaks near  $200 \text{ km s}^{-1}$  at 60 arcsec, then shows about a  $20 \text{ km s}^{-1}$  drop at 70 arcsec before the HI rotation curve comes in and rises back near  $200 \text{ km s}^{-1}$ . The average  $\text{H}\alpha$  rotation curve from Fabry-Perot observations in [Blais-Ouellette et al. \(2004\)](#) shows a similar feature, and agrees well with our results. However, [Blais-Ouellette et al. \(2004\)](#) detected a separate velocity component in the inner 8 arcsec, which could be associated with a bipolar outflow or almost counter-rotating disc.

Fig. 4 shows the rotation curve derived from the HI velocity field. The inclination and position angles for the HI vary with radius. The warped outer HI disc can be modeled using an increasing position angle. The resulting HI rotation curve shows a drop in rotational velocities around 500 arcsec, in agreement with the results of [Bosma \(1981a\)](#) and [Thornley & Mundy \(1997\)](#).

The observed rotation curve in NGC 5055 is decomposed into stellar bulge and disc and total gas disc components for baryonic mass (Fig. 5). The stellar disc and bulge are near maximal at a fixed  $M/L = 0.4$ . The stellar disc  $M/L$  can go up to 0.5 without over-shooting the observed inner rotation curve. [de Blok et al. \(2008\)](#) also came up with  $M/L = 0.5$  at  $3.6\mu\text{m}$  for the outer stellar disc in NGC 5055. Like NGC 5033, the mass distribution in NGC 5055 transitions from baryon-dominated to dark matter-dominated near  $2.2h_R$ .

**Table A4.** Properties of Known Companions to NGC 5055

Galaxy	RA, Dec (J2000)	Systemic <sup>a</sup> Velocity (km s <sup>-1</sup> )	Angular Separation (arcmin)	Physical <sup>b</sup> Separation (kpc)	Size <sup>c</sup> (a×b) (arcsec×arcsec)	Position Angle (deg)	$m_B$	$m_R$	$m_{3.6}$	$(B - R)_0$	$M_B$ <sup>b</sup>	HI Flux (Jy km s <sup>-1</sup> )
UGC 8313	13:13:53.9,+42:12:34	632(1)	23.96	63.4	180.0×83.5	31.9	14.45±0.03	13.49±0.03	11.32±0.04	0.93±0.04	-15.35±0.03	5.5
LEDA 166159	13:13:40.0,+42:02:38	371(2)	24.08	63.7	60.7×55.8	-25.6	18.51±0.14	17.22±0.14	15.47±0.29	1.27±0.20	-11.29±0.14	–

*Note.* – The apparent magnitudes are measured values and are not corrected for extinction.  $B - R$  and  $M_B$  are extinction corrected assuming  $A_B=0.064$  and  $A_R=0.038$  (Schlafly & Finkbeiner 2011). The extinction correction for the NIR is assumed to be negligible.

<sup>a</sup> Sources: (1) this work; (2) Karachentsev et al. (1999).

<sup>b</sup> Assuming a distance of 9.1 Mpc.

<sup>c</sup> Sizes indicate the diameters in arcseconds of the apertures used to measure the reported magnitudes.

### A15 UGC 08839

UGC 08839 is a dwarf irregular galaxy with an extended HI disc ( $D_{\text{HI}}/D_{25} = 5$ ). The HI integrated intensity map in Fig. A15 from new VLA observations shows a slight central depression surrounded by two peaks in intensity. Very little  $\text{H}\alpha$  emission was detected in the narrowband image, so UGC 08839 was not targeted for SparsePak observations. The velocity field of UGC 08839 shows solid body rotation in with a slight warp at the outer edges where the isovelocity contours turn over. This warp is modeled as a decrease in inclination angle beyond a radius of 130 arcsec. The resulting rotation curve rises slowly in the central  $\sim 150$  arcsec after which it flattens out to a radius of 210 arcsec (Fig. 4).

The rotation curve decomposition analysis was done using estimates of the baryonic components from the stellar disc surface density and the atomic HI gas surface density distributions. The baryonic contributions to the total observed rotation curve shown in Fig. 5 assuming a fixed  $M/L = 0.5$  are less than the dark matter halo model contribution at all measured radii. The contribution from gas overtakes the stellar disc contribution at about 70 arcsec in the fixed  $M/L$  model. This is not unexpected given the visible dominance of the HI over the stars in terms of radial extent. However, the stellar disc contribution can be maximized with a  $M/L$  up to 3.0 to describe the observed rotation at inner radii. In this maximum disc model, the stellar contribution is greater than or equal to the gas contribution at all measured radii. The distribution of mass in this context seems much less astrophysically plausible, but it provides an upper limit on the total baryon content in UGC 08839. The maximum baryon mass fraction at  $2.2h_{\text{R}}$  derived from the maximum disc decomposition is 0.59, compared to the fixed  $M/L$  decomposition which is only 0.18.

### A16 NGC 5608

NGC 5608 is a dwarf irregular galaxy for which we acquired new VLA HI observations. The new data reveal an HI disc with a smooth, featureless morphology similar to the stellar disc at  $3.6\mu\text{m}$  (Fig. A16). The highest density of HI gas additionally appears to coincide with location of the strongest  $\text{H}\alpha$  observed in the narrowband image. NGC 5608 was not targeted for ionized gas kinematics from SparsePak observations due to the limited spatial extent of the  $\text{H}\alpha$  emission. The distribution of HI is slightly asymmetric, which can best be seen in the velocity field where the receding (east) side of the galaxy appears to extend farther than the approaching (west) side.

Similar to UGC 08839, Fig. 4 demonstrates that the rotation curve in NGC 5608 is solid body in the inner parts and then turns over and remains flat beyond 60 arcsec. The decomposition of the observed HI rotation curve was performed assuming disc potentials for both the gas and star rotation curve models. Like UGC 08839, the decomposition for NGC 5608 using fixed  $M/L = 0.5$  results in a total mass distribution that is dark matter-dominated at all radii and has a significant contribution from gas at large radii. The maximum stellar disc contribution requires a  $M/L = 1.8$  and gives a baryon mass fraction at  $2.2h_{\text{R}}$  of 0.59, which is the same as was found for UGC 08839.

This paper has been typeset from a  $\text{T}_{\text{E}}\text{X}/\text{L}^{\text{A}}\text{T}_{\text{E}}\text{X}$  file prepared by the author.

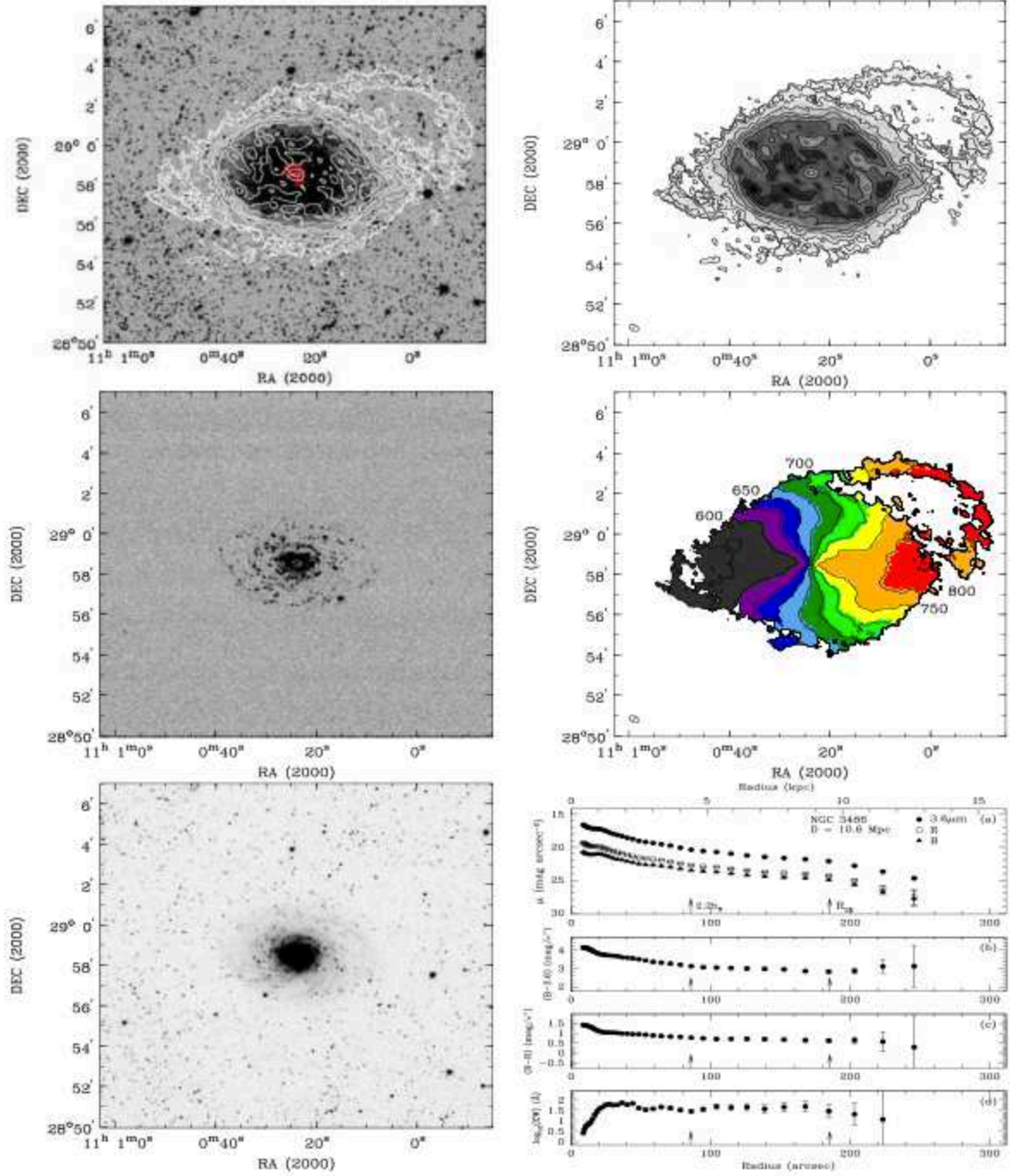


**Figure A1.** NGC 3486: (*top left*) Low spatial resolution HI integrated intensity contours from new VLA data (*white*) and CO intensity contours (*red*) from CARMA STING (Wong et al. 2013) overlaid on the *Spitzer* 3.6μm image. (*top right*) Low spatial resolution HI intensity contours overlaid on the low spatial resolution HI intensity image. The first low resolution HI contour represents a column density of  $4 \times 10^{19}$  atoms  $\text{cm}^{-2}$ . (*middle left*) Narrowband Hα image from the WIYN 0.9 m telescope. (*middle right*) HI velocity field with isovelocity contours derived from the low spatial resolution HI data. The isovelocity contours are spaced every 25  $\text{km s}^{-1}$ . (*bottom left*) *Spitzer* 3.6μm image with a high surface brightness stretch. (*bottom right*) Ellipse photometry results (see Sections 2.5 and 2.6) showing radial profiles of surface brightness,  $B - 3.6$  colour,  $B - R$  colour, and equivalent width (EW).



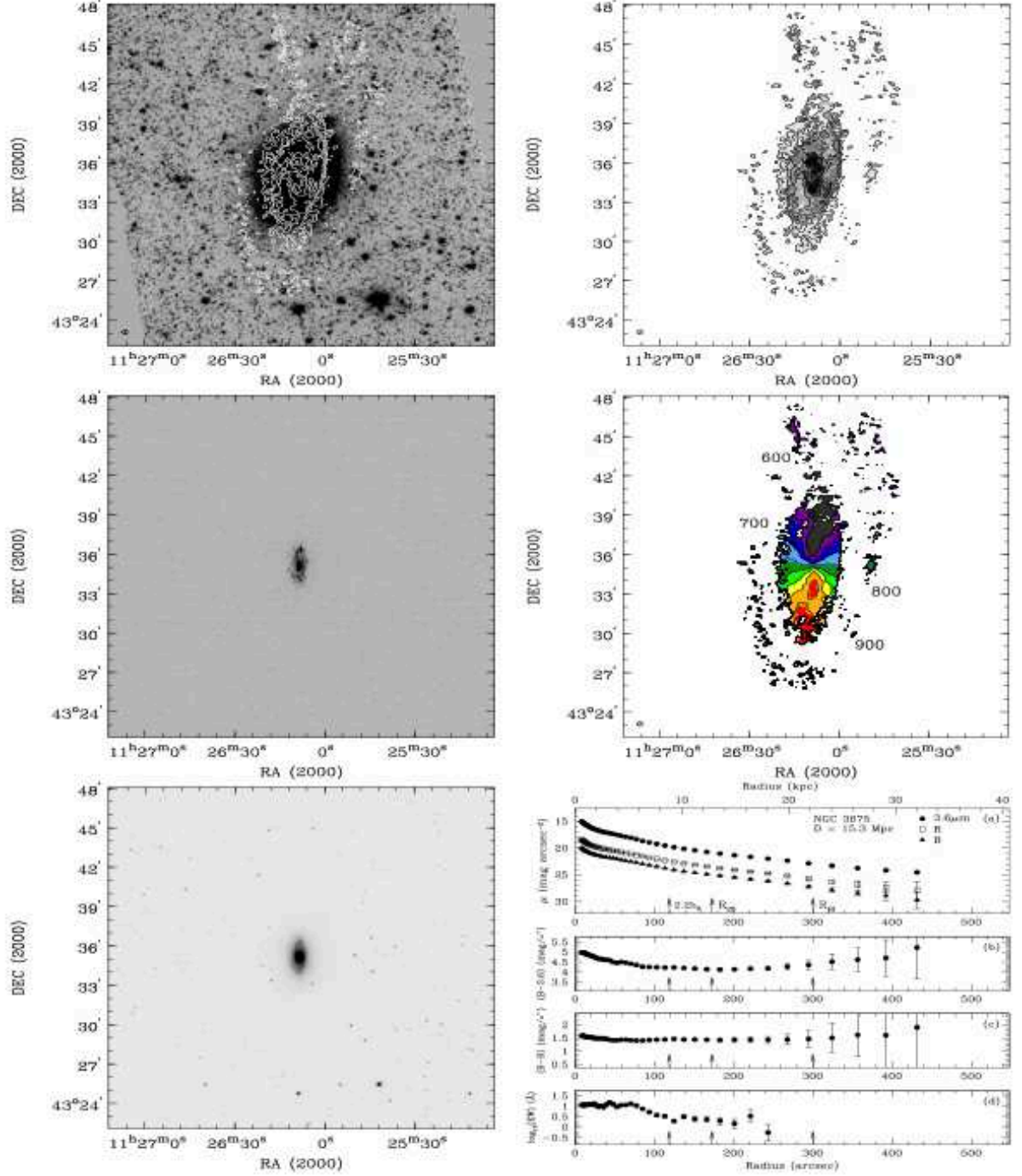


**Figure A2. NGC 3675:** (*top left*) Medium spatial resolution HI integrated intensity contours from archival VLA data overlaid on the *Spitzer* 3.6μm image. (*top right*) Medium spatial resolution HI intensity contours overlaid on the medium spatial resolution HI intensity image. The first medium resolution HI contour represents a column density of  $6 \times 10^{19}$  atoms  $\text{cm}^{-2}$ . (*middle left*) Narrowband Hα image from the WIYN 0.9 m telescope. (*middle right*) HI velocity field with isovelocity contours derived from the medium spatial resolution HI data. The isovelocity contours are spaced every 50  $\text{km s}^{-1}$ . (*bottom left*) *Spitzer* 3.6μm image with a high surface brightness stretch. (*bottom right*) Ellipse photometry results (see Sections 2.5 and 2.6) showing radial profiles of surface brightness,  $B - 3.6$  colour,  $B - R$  colour, and equivalent width (EW).

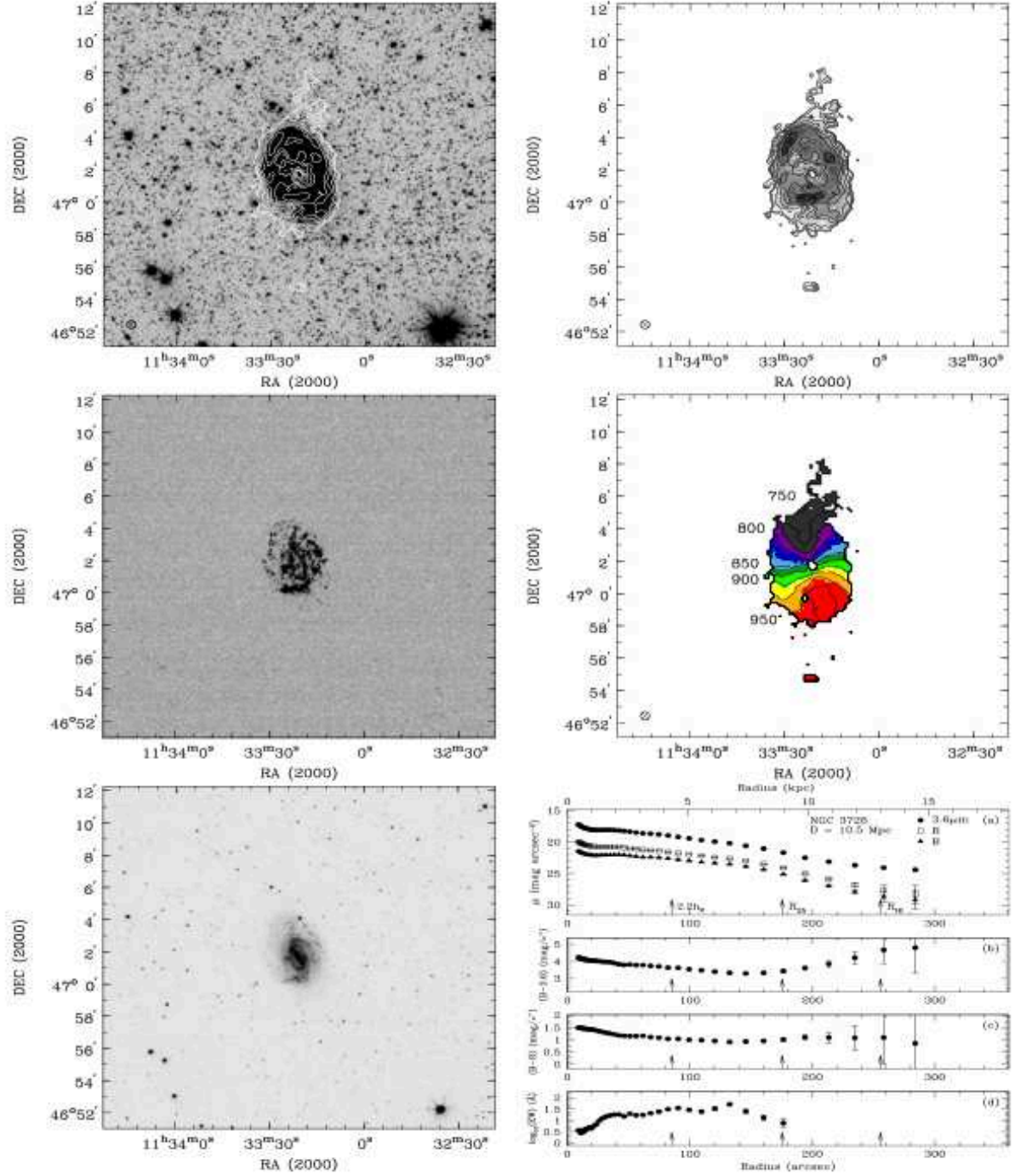


**Figure A3.** NGC 3726: (*top left*) 30'' spatial resolution HI integrated intensity contours from the WSRT overlaid on the *Spitzer* 3.6μm image. (*top right*) 30'' spatial resolution HI intensity contours overlaid on the same spatial resolution HI intensity image. The first HI contour represents a column density of  $6 \times 10^{19}$  atoms cm $^{-2}$ . (*middle left*) Narrowband H $\alpha$  image from the WIYN 0.9 m telescope. (*middle right*) HI velocity field with isovelocity contours derived from the 30'' spatial resolution HI data. The isovelocity contours are spaced every 25 km s $^{-1}$ . (*bottom left*) *Spitzer* 3.6μm image with a high surface brightness stretch. (*bottom right*) Ellipse photometry results (see Sections 2.5 and 2.6) showing radial profiles of surface brightness,  $B - 3.6$  colour,  $B - R$  colour, and equivalent width (EW).

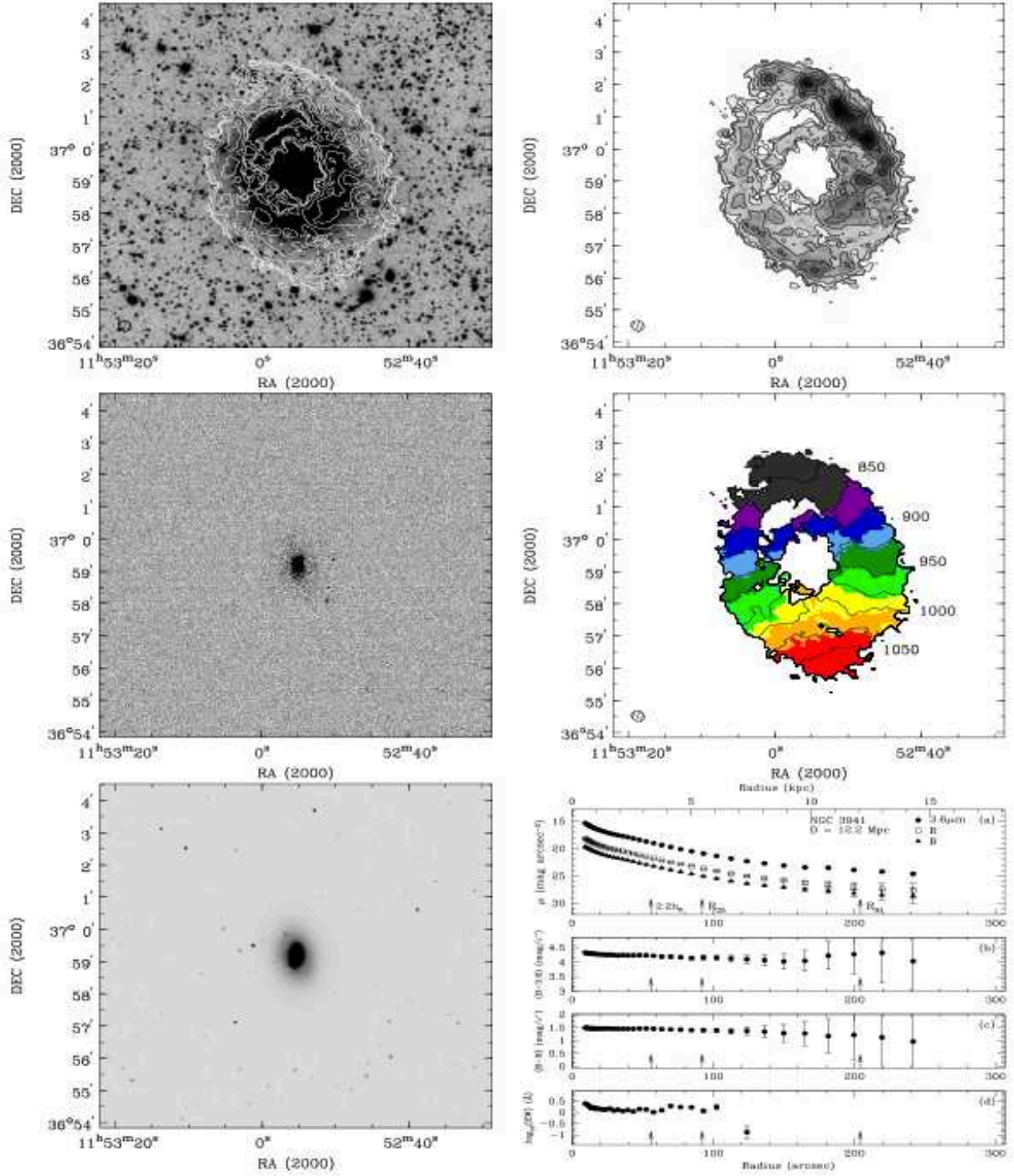


**Figure A4. NGC 3941:** (*top left*) Low spatial resolution HI integrated intensity contours from new VLA data overlaid on the *Spitzer* 3.6μm image. (*top right*) Low spatial resolution HI intensity contours overlaid on the low spatial resolution HI intensity image. The first low resolution HI contour represents a column density of  $2 \times 10^{19}$  atoms cm<sup>-2</sup>. (*middle left*) Narrowband Hα image from the WIYN 0.9 m telescope. (*middle right*) HI velocity field with isovelocity contours derived from the low spatial resolution HI data. The isovelocity contours are spaced every 25 km s<sup>-1</sup>. (*bottom left*) *Spitzer* 3.6μm image with a high surface brightness stretch. (*bottom right*) Ellipse photometry results (see Sections 2.5 and 2.6) showing radial profiles of surface brightness,  $B - 3.6$  colour,  $B - R$  colour, and equivalent width (EW).



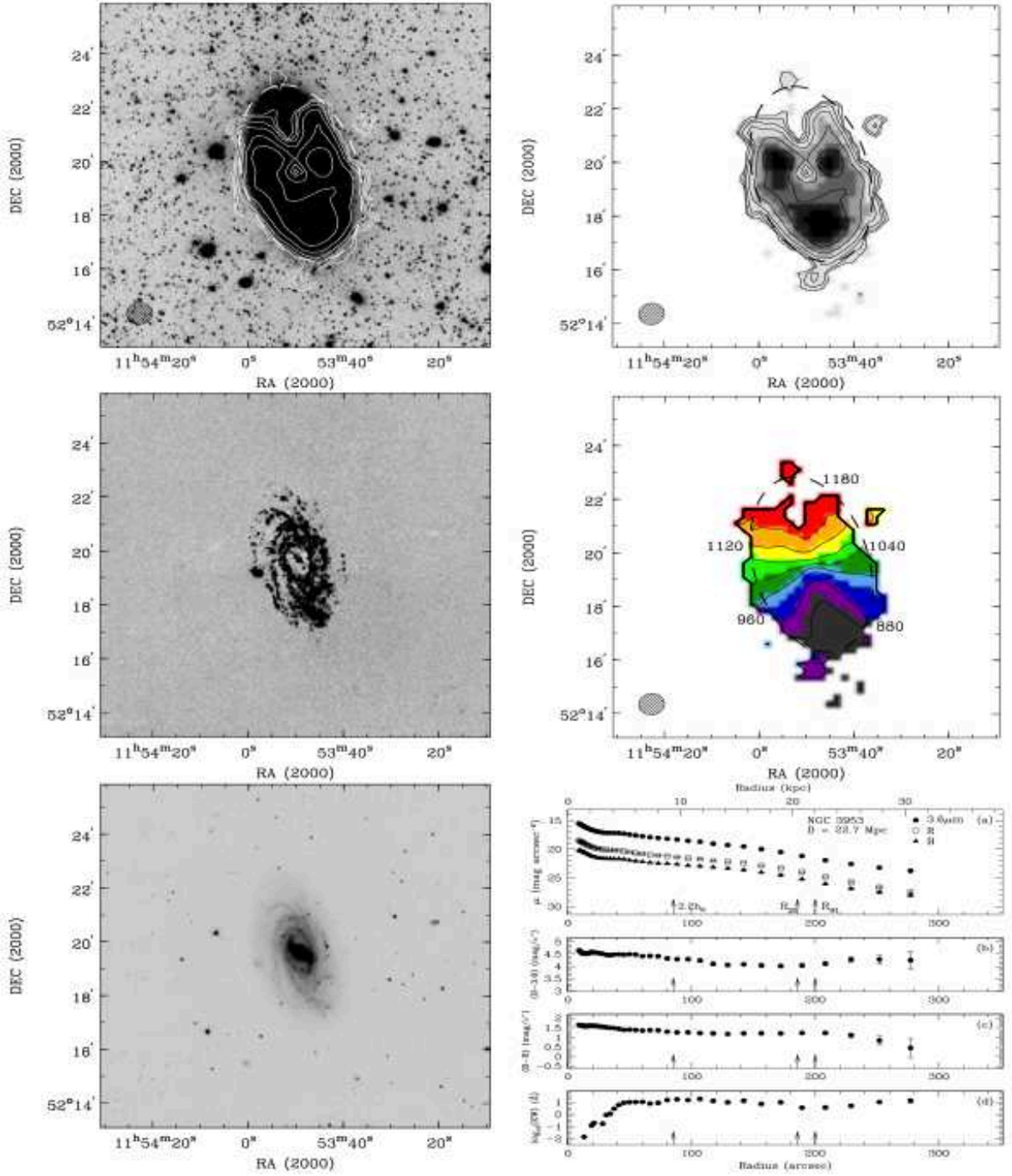


**Figure A5. NGC 3953:** (top left) 30'' spatial resolution HI integrated intensity contours from the WSRT and CO intensity contours (red) from BIMA SONG (Helfer et al. 2003) overlaid on the *Spitzer* 3.6μm image. (top right) 30'' spatial resolution HI intensity contours overlaid on the same spatial resolution HI intensity image. The first HI contour represents a column density of  $2 \times 10^{20}$  atoms  $\text{cm}^{-2}$ . (middle left) Narrowband Hα image from the WIYN 0.9 m telescope. (middle right) HI velocity field with isovelocity contours derived from the 30'' spatial resolution HI data. The isovelocity contours are spaced every 50  $\text{km s}^{-1}$ . (bottom left) *Spitzer* 3.6μm image with a high surface brightness stretch. (bottom right) Ellipse photometry results (see Sections 2.5 and 2.6) showing radial profiles of surface brightness,  $B - 3.6$  colour,  $B - R$  colour, and equivalent width (EW).



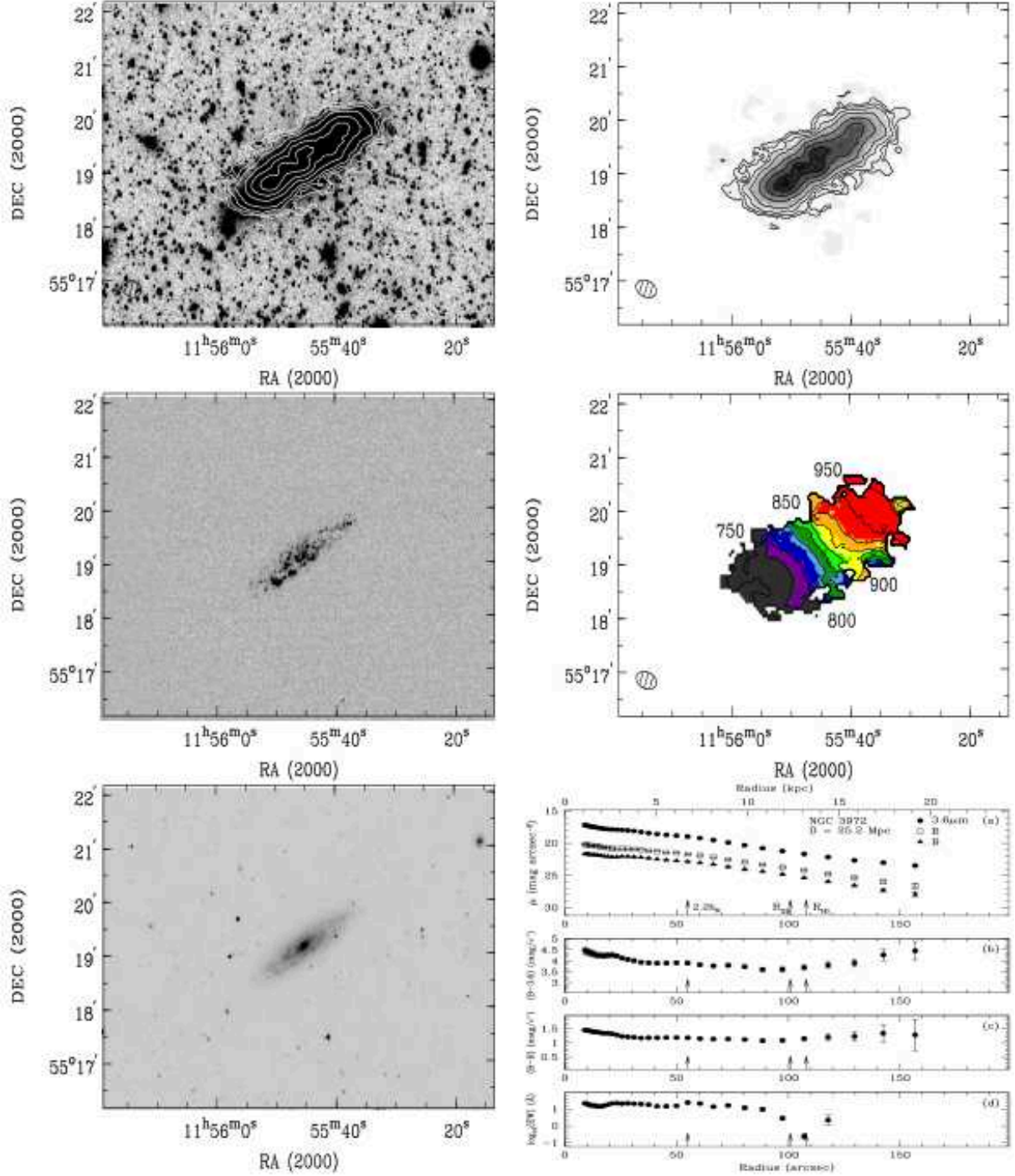


**Figure A6.** NGC 3972: (top left) Low spatial resolution HI integrated intensity contours from new VLA data overlaid on the *Spitzer* 3.6μm image. (top right) Low spatial resolution HI intensity contours overlaid on the same spatial resolution HI intensity image. The first HI contour represents a column density of  $2 \times 10^{19}$  atoms  $\text{cm}^{-2}$ . (middle left) Narrowband Hα image from the WIYN 0.9 m telescope. (middle right) HI velocity field with isovelocity contours derived from the low spatial resolution HI data. The isovelocity contours are spaced every 25  $\text{km s}^{-1}$ . (bottom left) *Spitzer* 3.6μm image with a high surface brightness stretch. (bottom right) Ellipse photometry results (see Sections 2.5 and 2.6) showing radial profiles of surface brightness,  $B - 3.6$  colour,  $B - R$  colour, and equivalent width (EW).

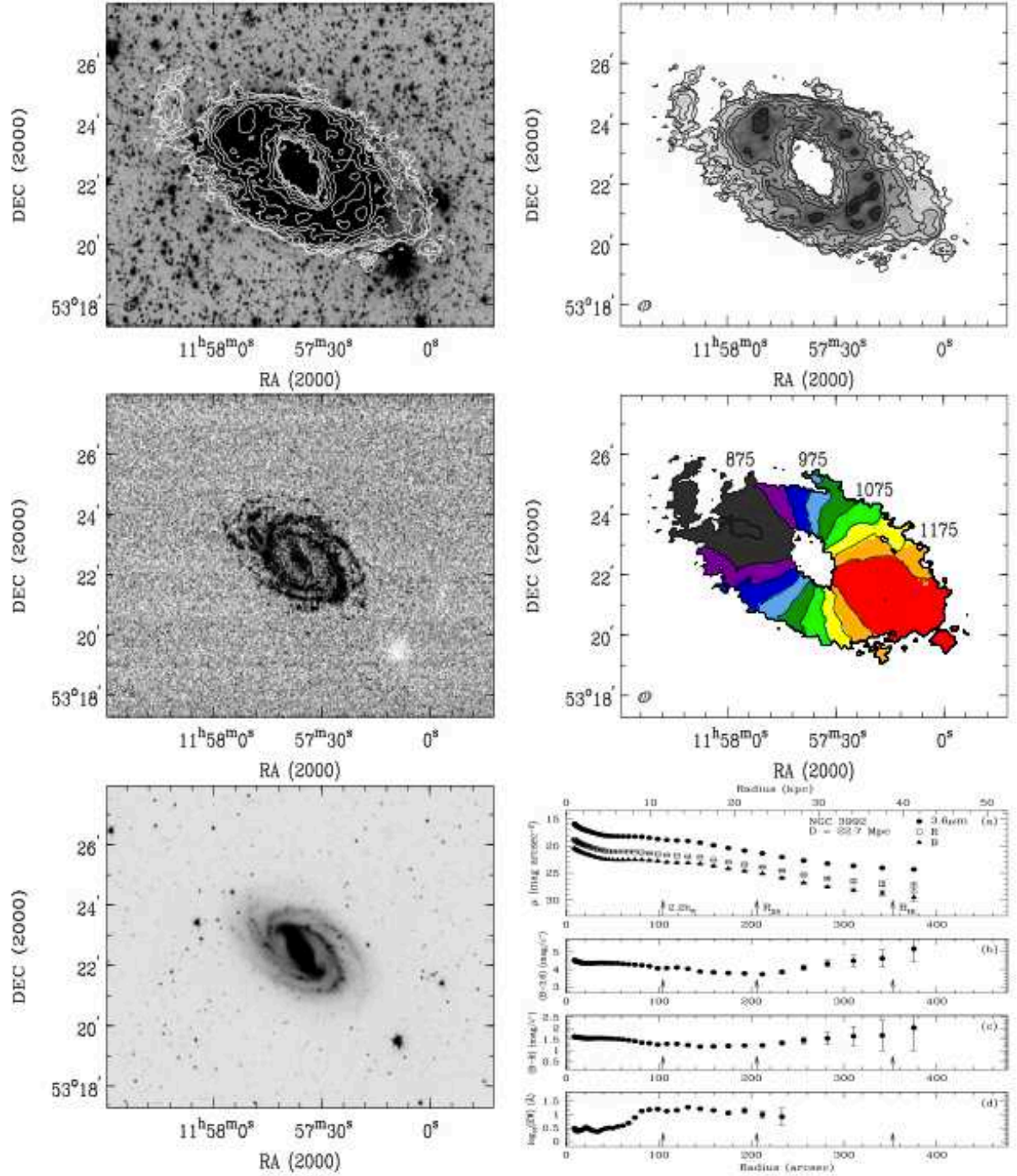


**Figure A7. NGC 3992:** (*top left*) Low spatial resolution HI integrated intensity contours from archival VLA data overlaid on the *Spitzer* 3.6 $\mu$ m image. (*top right*) Low spatial resolution HI intensity contours overlaid on the low spatial resolution HI intensity image. The first low resolution HI contour represents a column density of  $4 \times 10^{19}$  atoms  $\text{cm}^{-2}$ . (*middle left*) Narrowband H $\alpha$  image from the WIYN 0.9 m telescope. (*middle right*) HI velocity field with isovelocity contours derived from the low spatial resolution HI data. The isovelocity contours are spaced every 50  $\text{km s}^{-1}$ . (*bottom left*) *Spitzer* 3.6 $\mu$ m image with a high surface brightness stretch. (*bottom right*) Ellipse photometry results (see Sections 2.5 and 2.6) showing radial profiles of surface brightness,  $B - 3.6$  colour,  $B - R$  colour, and equivalent width (EW).

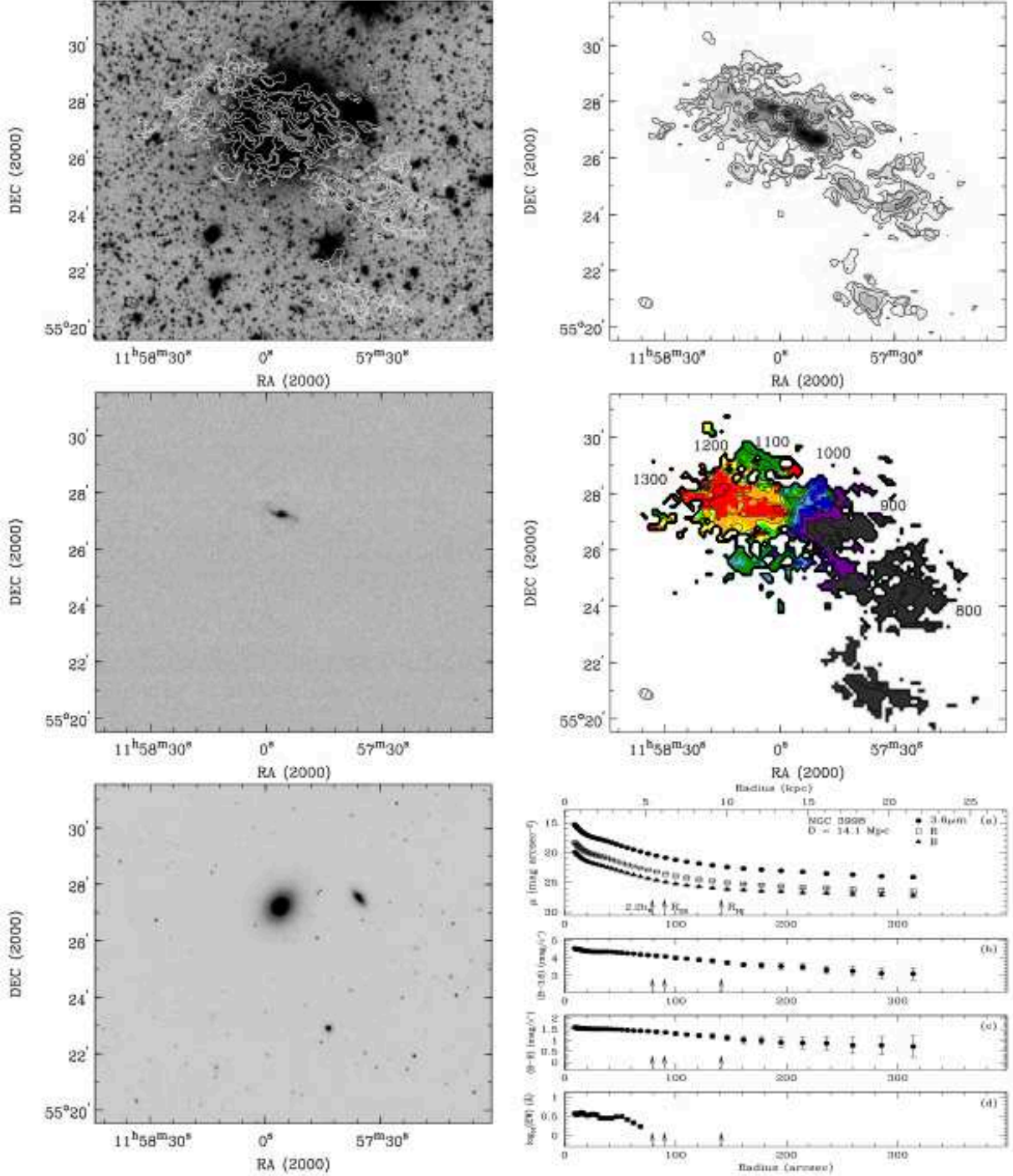


**Figure A8. NGC 3998:** (*top left*) Spectral binned low spatial resolution HI integrated intensity contours from new VLA data overlaid on the *Spitzer* 3.6 $\mu$ m image. (*top right*) Spectral binned low spatial resolution HI intensity contours overlaid on the spectral binned low spatial resolution HI intensity image. The first low resolution HI contour represents a column density of  $2 \times 10^{19}$  atoms  $\text{cm}^{-2}$ . (*middle left*) Narrowband H $\alpha$  image from the WIYN 0.9 m telescope. (*middle right*) HI velocity field with isovelocity contours derived from the spectral binned low spatial resolution HI data. The isovelocity contours are spaced every 50  $\text{km s}^{-1}$ . (*bottom left*) *Spitzer* 3.6 $\mu$ m image with a high surface brightness stretch. (*bottom right*) Ellipse photometry results (see Sections 2.5 and 2.6) showing radial profiles of surface brightness,  $B - 3.6$  colour,  $B - R$  colour, and equivalent width (EW).



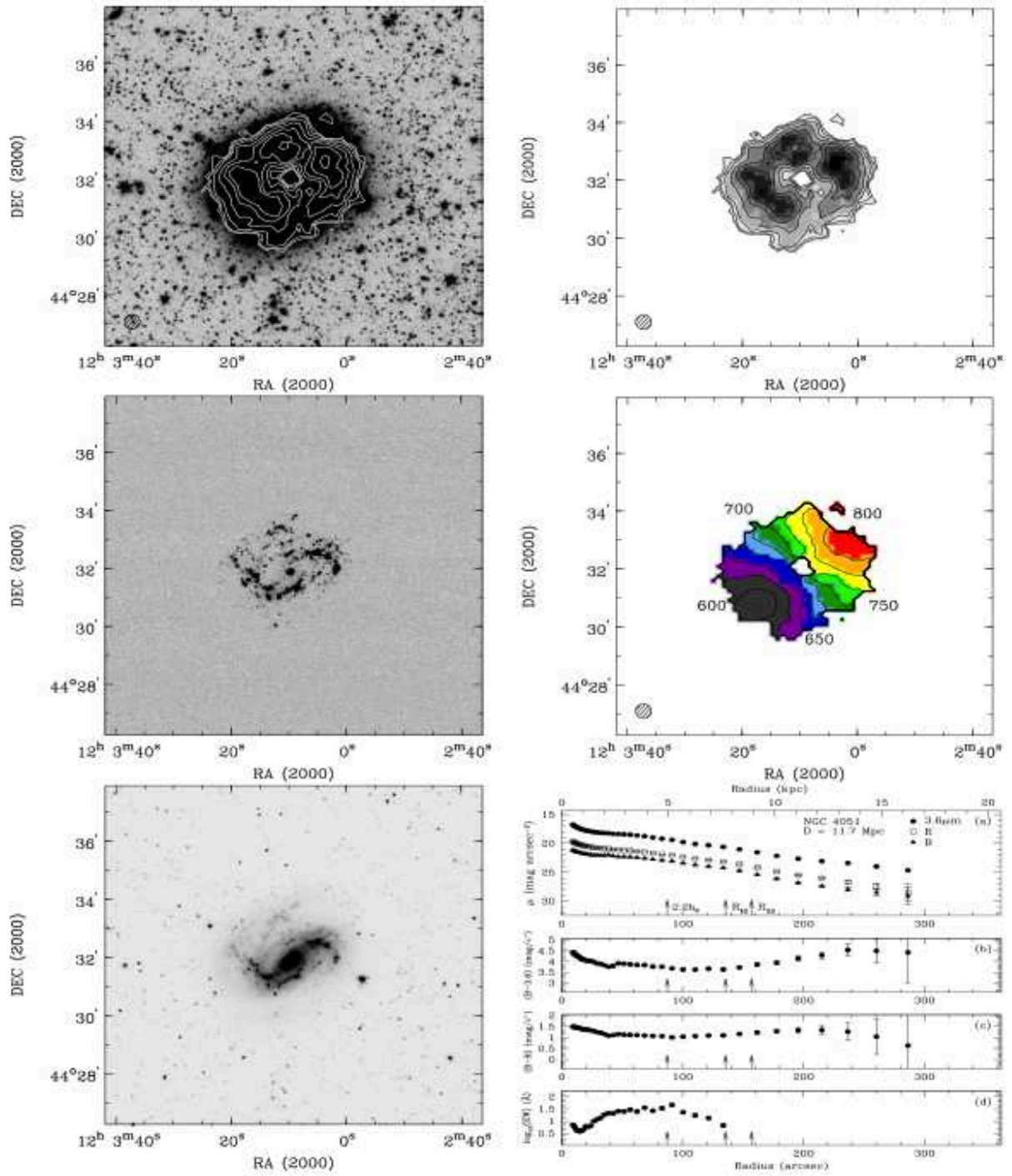


**Figure A9.** NGC 4051: (*top left*) 30'' spatial resolution HI integrated intensity contours from the WSRT overlaid on the *Spitzer* 3.6μm image. (*top right*) 30'' spatial resolution HI intensity contours overlaid on the same spatial resolution HI intensity image. The first HI contour represents a column density of  $6 \times 10^{19}$  atoms  $\text{cm}^{-2}$ . (*middle left*) Narrowband Hα image from the WIYN 0.9 m telescope. (*middle right*) HI velocity field with isovelocity contours derived from the 30'' spatial resolution HI data. The isovelocity contours are spaced every 25  $\text{km s}^{-1}$ . (*bottom left*) *Spitzer* 3.6μm image with a high surface brightness stretch. (*bottom right*) Ellipse photometry results (see Sections 2.5 and 2.6) showing radial profiles of surface brightness,  $B - 3.6$  colour,  $B - R$  colour, and equivalent width (EW).



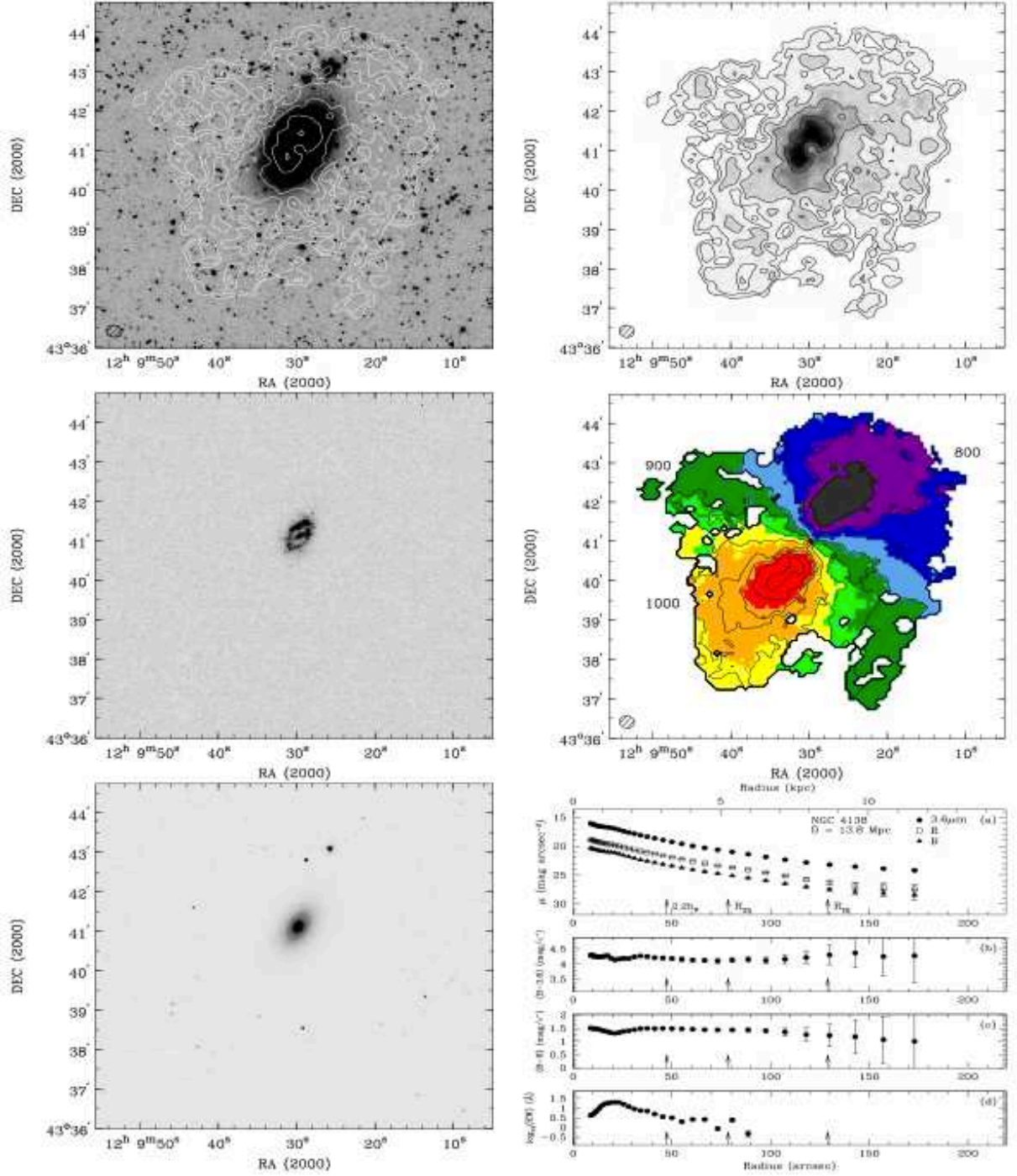


**Figure A10.** NGC 4138: (top left) Low spatial resolution HI integrated intensity contours from archival VLA data overlaid on the *Spitzer* 3.6 $\mu$ m image. (top right) Low spatial resolution HI intensity contours overlaid on the low spatial resolution HI intensity image. The first low resolution HI contour represents a column density of  $3.4 \times 10^{19}$  atoms  $\text{cm}^{-2}$ . (middle left) Narrowband H $\alpha$  image from the WIYN 0.9 m telescope. (middle right) HI velocity field with isovelocity contours derived from the low spatial resolution HI data. The isovelocity contours are spaced every 30  $\text{km s}^{-1}$ . (bottom left) *Spitzer* 3.6 $\mu$ m image with a high surface brightness stretch. (bottom right) Ellipse photometry results (see Sections 2.5 and 2.6) showing radial profiles of surface brightness,  $B - 3.6$  colour,  $B - R$  colour, and equivalent width (EW).

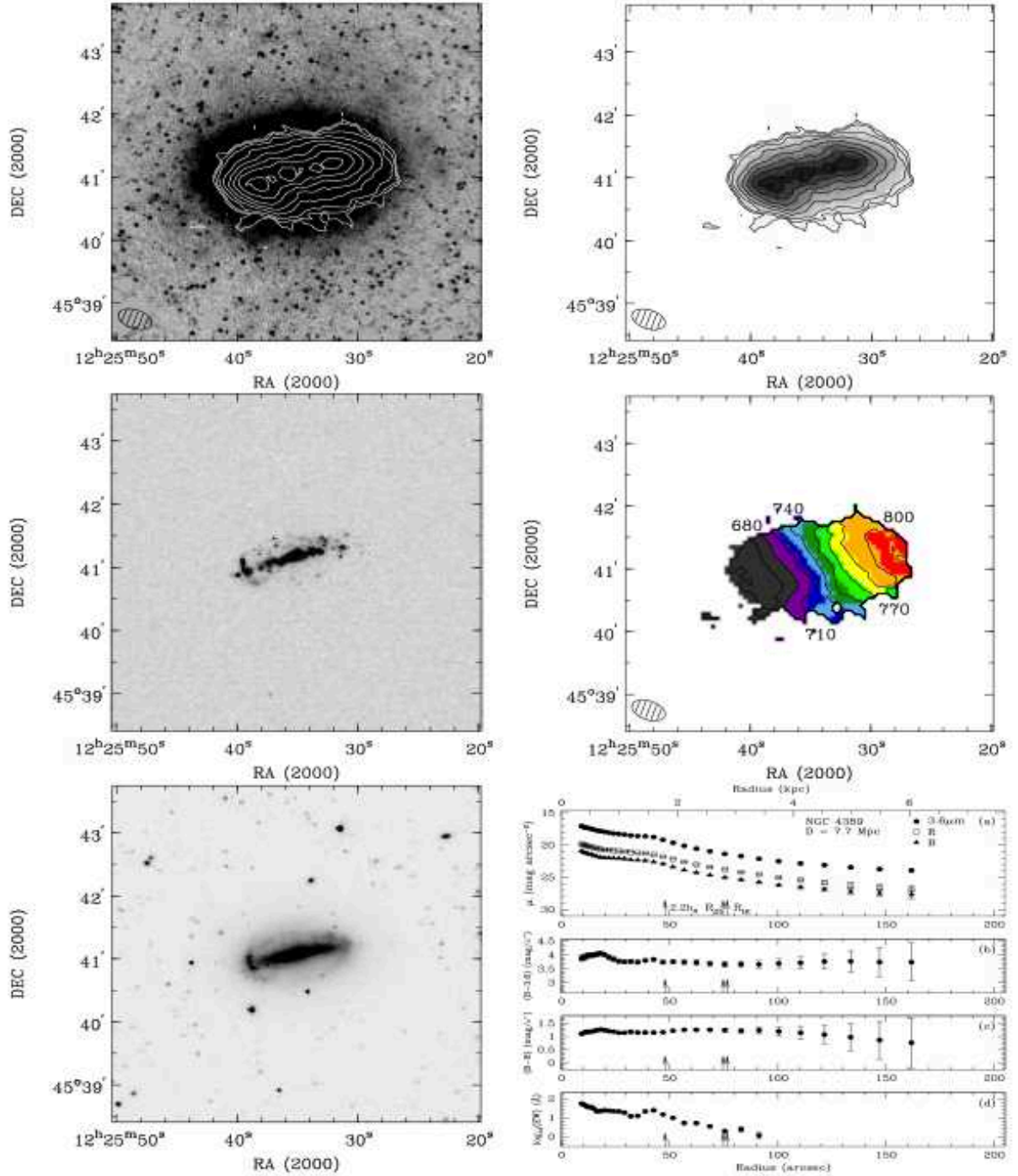


**Figure A11. NGC 4389:** (*top left*) Low spatial resolution HI integrated intensity contours from new VLA data overlaid on the *Spitzer*  $3.6\mu\text{m}$  image. (*top right*) Low spatial resolution HI intensity contours overlaid on the low spatial resolution HI intensity image. The first low resolution HI contour represents a column density of  $4 \times 10^{19} \text{ atoms cm}^{-2}$ . (*middle left*) Narrowband  $\text{H}\alpha$  image from the WIYN 0.9 m telescope. (*middle right*) HI velocity field with isovelocity contours derived from the low spatial resolution HI data. The isovelocity contours are spaced every  $15 \text{ km s}^{-1}$ . (*bottom left*) *Spitzer*  $3.6\mu\text{m}$  image with a high surface brightness stretch. (*bottom right*) Ellipse photometry results (see Sections 2.5 and 2.6) showing radial profiles of surface brightness,  $B - 3.6$  colour,  $B - R$  colour, and equivalent width (EW).

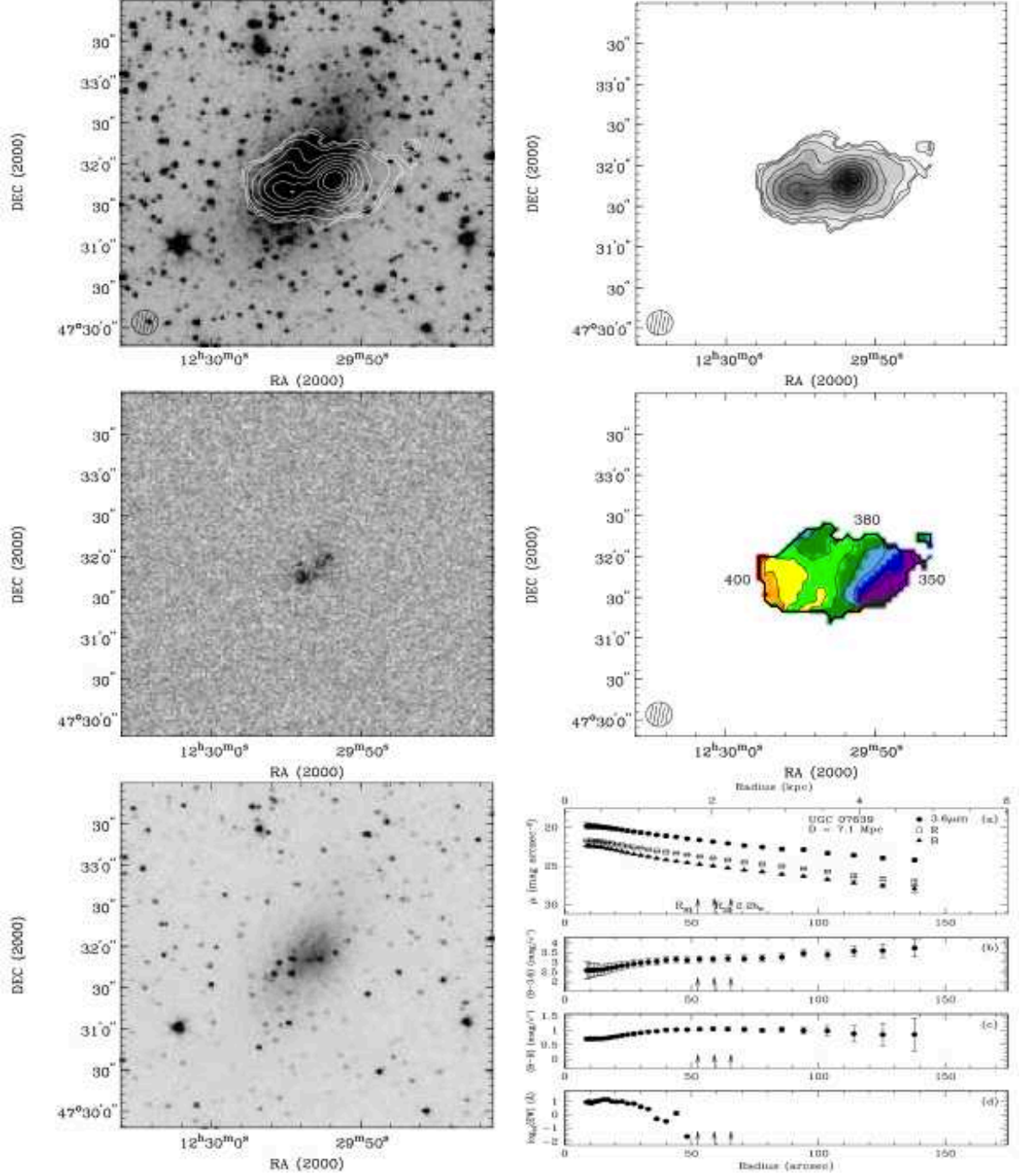


**Figure A12. UGC 07639:** (top left) Low spatial resolution HI integrated intensity contours from new VLA data overlaid on the *Spitzer* 3.6μm image. (top right) Low spatial resolution HI intensity contours overlaid on the low spatial resolution HI intensity image. The first low resolution HI contour represents a column density of  $4 \times 10^{19}$  atoms  $\text{cm}^{-2}$ . (middle left) Narrowband Hα image from the WIYN 0.9 m telescope. (middle right) HI velocity field with isovelocity contours derived from the low spatial resolution HI data. The isovelocity contours are spaced every 5  $\text{km s}^{-1}$ . (bottom left) *Spitzer* 3.6μm image with a high surface brightness stretch. (bottom right) Ellipse photometry results (see Sections 2.5 and 2.6) showing radial profiles of surface brightness,  $B - 3.6$  colour,  $B - R$  colour, and equivalent width (EW).



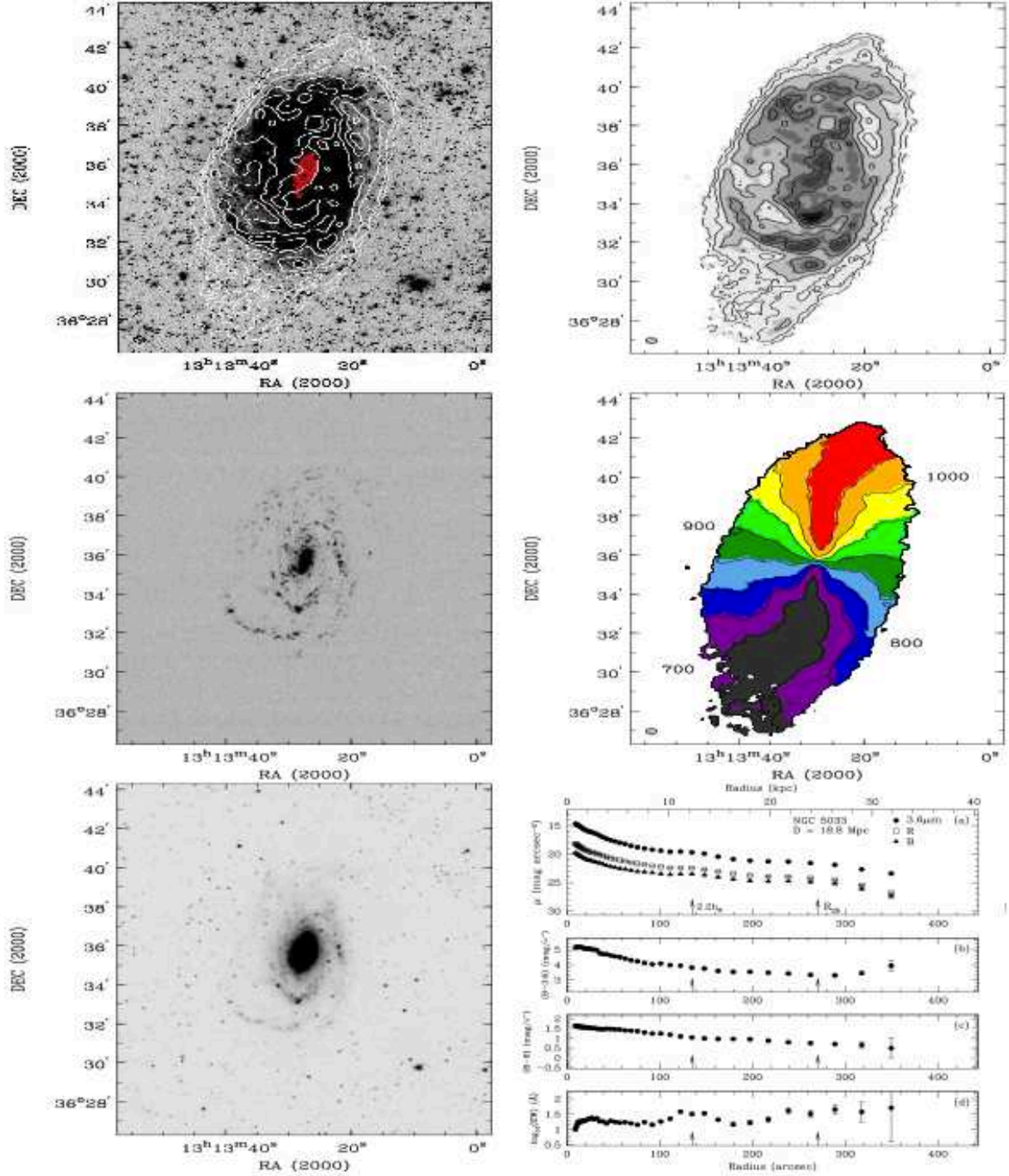


**Figure A13. NGC 5033:** (*top left*) Medium spatial resolution HI integrated intensity contours from archival VLA data (*white*) and CO intensity contours (*red*) from BIMA SONG (Helfer et al. 2003) overlaid on the *Spitzer* 3.6 $\mu$ m image. (*top right*) Medium spatial resolution HI intensity contours overlaid on the medium spatial resolution HI intensity image. The first low resolution HI contour represents a column density of  $4 \times 10^{19}$  atoms  $\text{cm}^{-2}$ . (*middle left*) Narrowband H $\alpha$  image from the WIYN 0.9 m telescope. (*middle right*) HI velocity field with isovelocity contours derived from the medium spatial resolution HI data. The isovelocity contours are spaced every 50  $\text{km s}^{-1}$ . (*bottom left*) *Spitzer* 3.6 $\mu$ m image with a high surface brightness stretch. (*bottom right*) Ellipse photometry results (see Sections 2.5 and 2.6) showing radial profiles of surface brightness,  $B - 3.6$  colour,  $B - R$  colour, and equivalent width (EW).

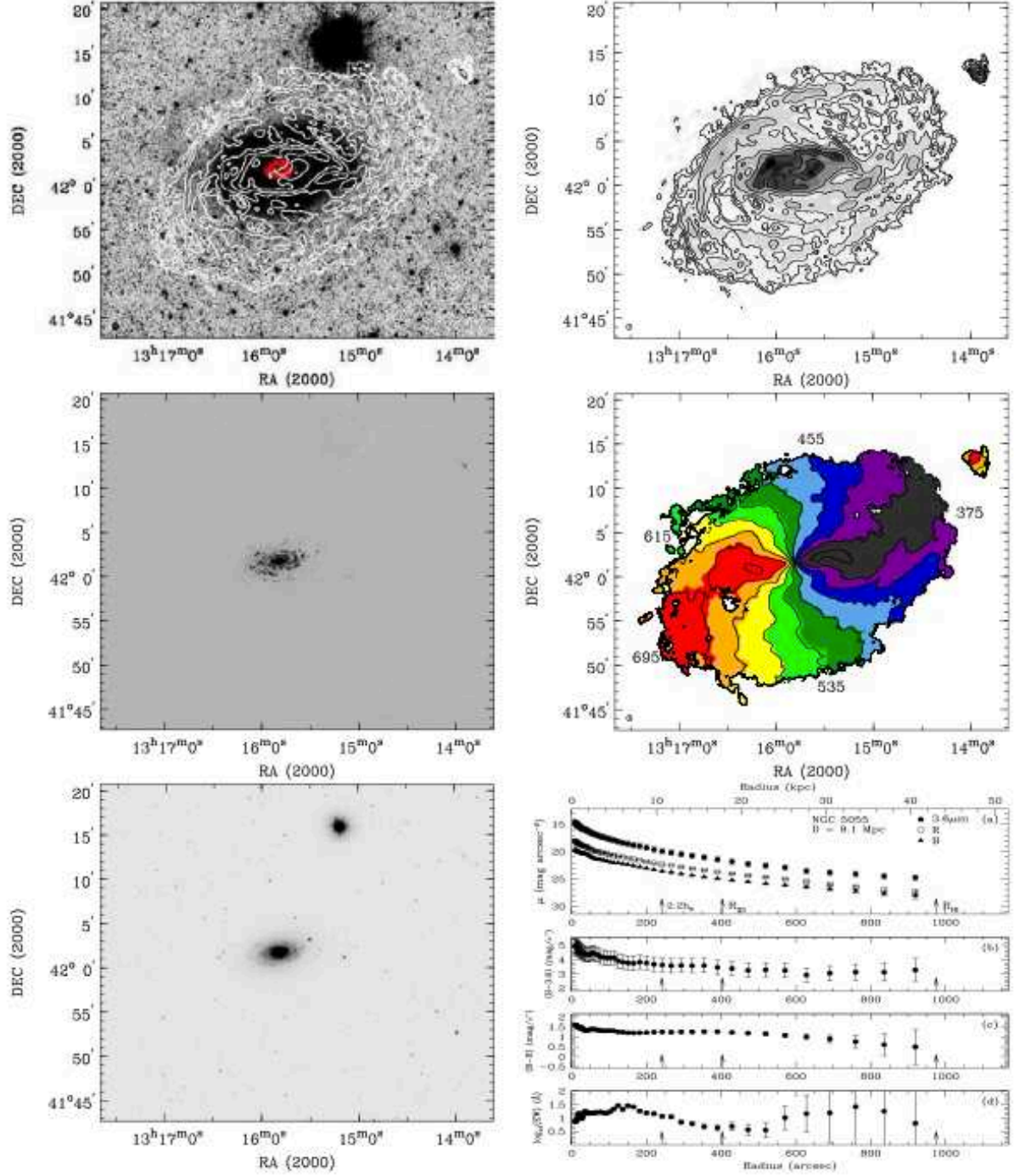


**Figure A14.** NGC 5055: (top left) HI integrated intensity contours from the tapered image from archival VLA data (white) and CO intensity contours (red) from BIMA SONG (Helfer et al. 2003) overlaid on the *Spitzer* 3.6μm image. (top right) HI intensity contours from the tapered image overlaid on the medium spatial resolution HI intensity image. The first low resolution HI contour represents a column density of  $4 \times 10^{19}$  atoms  $\text{cm}^{-2}$ . (middle left) Narrowband Hα image from the WIYN 0.9 m telescope. (middle right) HI velocity field with isovelocity contours derived from the tapered spatial resolution HI data. The isovelocity contours are spaced every 40  $\text{km s}^{-1}$ . (bottom left) *Spitzer* 3.6μm image with a high surface brightness stretch. (bottom right) Ellipse photometry results (see Sections 2.5 and 2.6) showing radial profiles of surface brightness,  $B - 3.6$  colour,  $B - R$  colour, and equivalent width (EW).



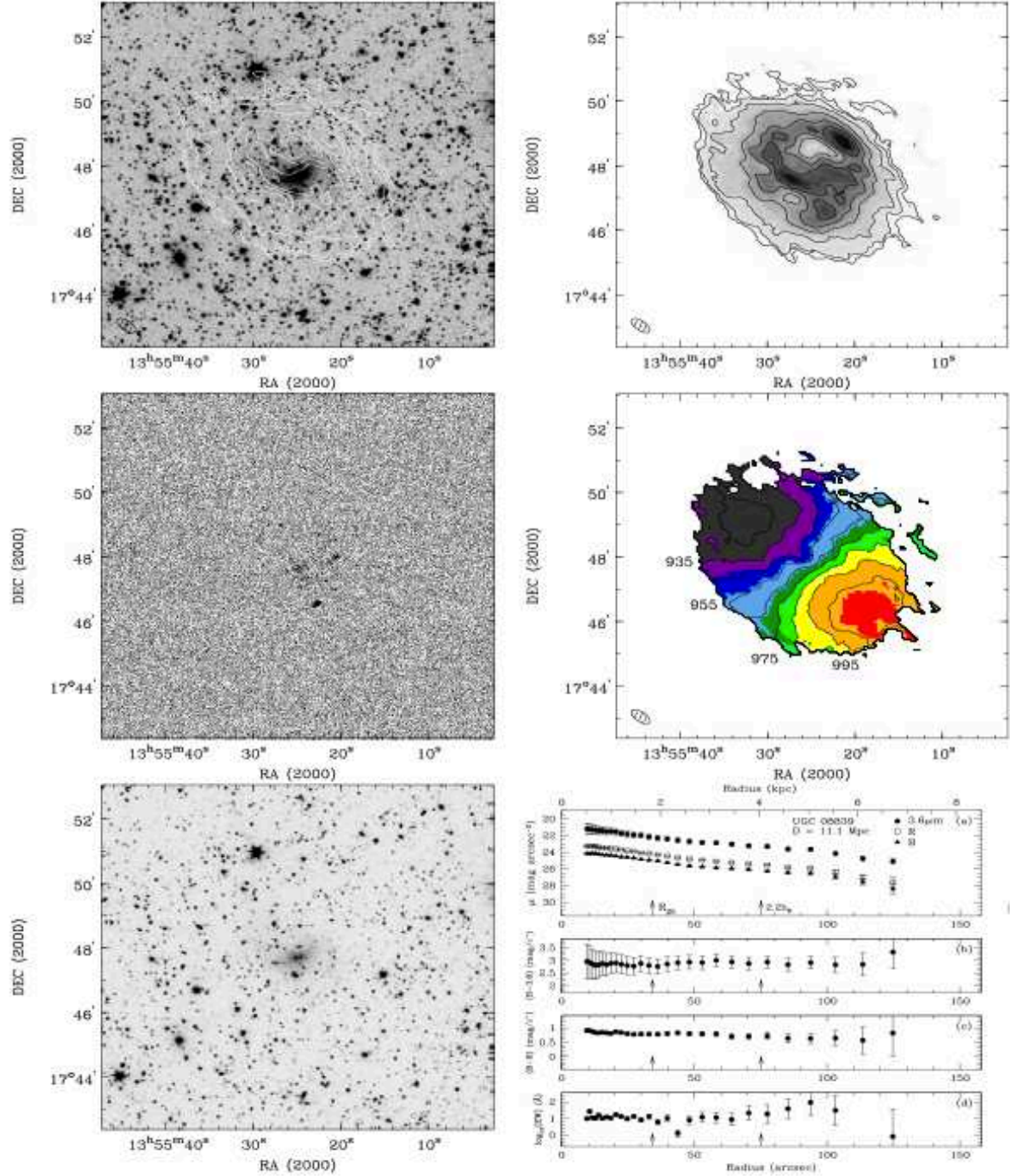


**Figure A15. UGC 08839:** (top left) Low spatial resolution HI integrated intensity contours from new VLA data overlaid on the *Spitzer* 3.6μm image. (top right) Low spatial resolution HI intensity contours overlaid on the low spatial resolution HI intensity image. The first low resolution HI contour represents a column density of  $4 \times 10^{19}$  atoms  $\text{cm}^{-2}$ . (middle left) Narrowband Hα image from the WIYN 0.9 m telescope. (middle right) HI velocity field with isovelocity contours derived from the low spatial resolution HI data. The isovelocity contours are spaced every 10  $\text{km s}^{-1}$ . (bottom left) *Spitzer* 3.6μm image with a high surface brightness stretch. (bottom right) Ellipse photometry results (see Sections 2.5 and 2.6) showing radial profiles of surface brightness,  $B - 3.6$  colour,  $B - R$  colour, and equivalent width (EW).

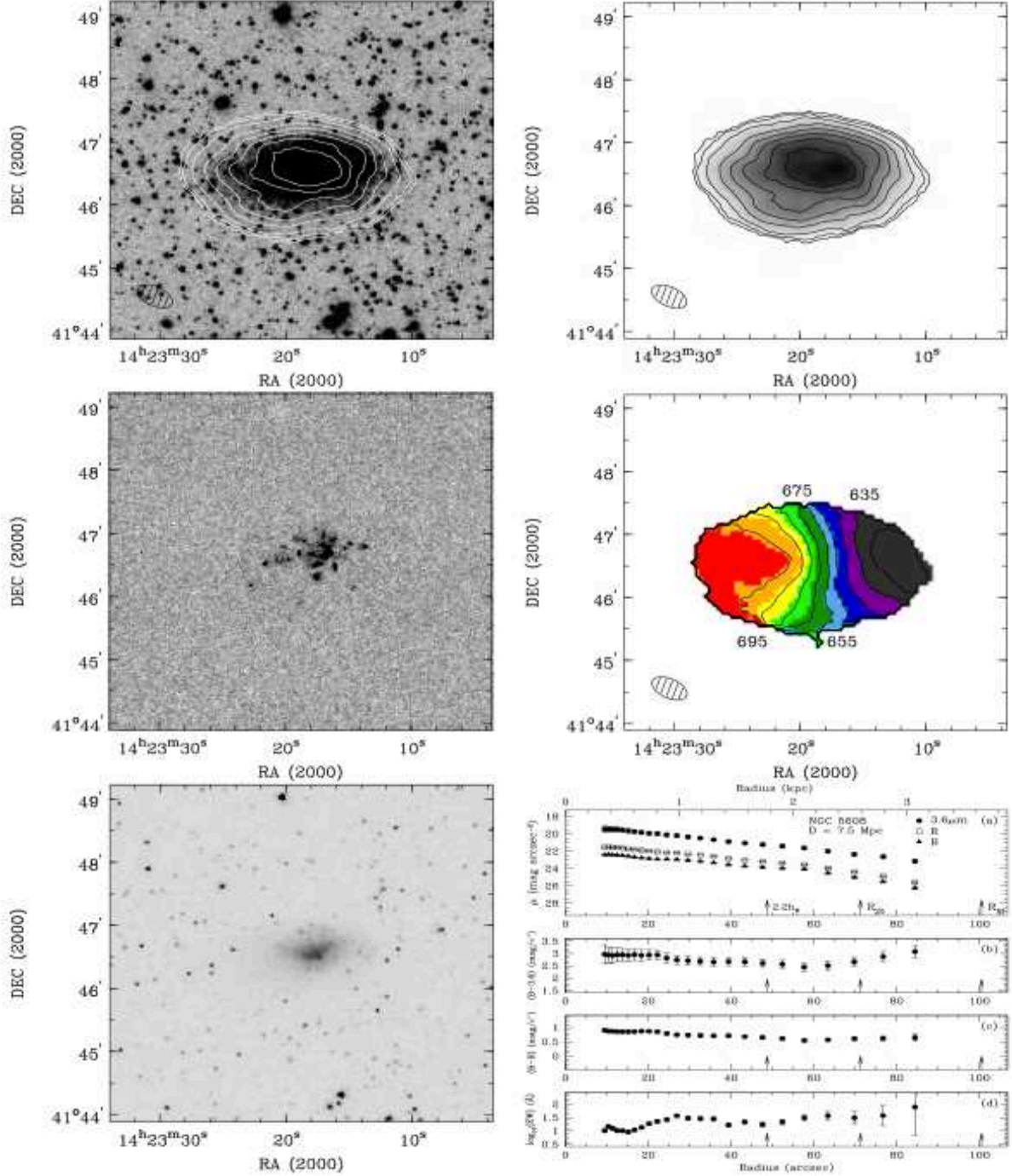


**Figure A16. NGC 5608:** (*top left*) Low spatial resolution HI integrated intensity contours from new VLA data overlaid on the *Spitzer* 3.6μm image. (*top right*) Low spatial resolution HI intensity contours overlaid on the low spatial resolution HI intensity image. The first low resolution HI contour represents a column density of  $4 \times 10^{19}$  atoms  $\text{cm}^{-2}$ . (*middle left*) Narrowband Hα image from the WIYN 0.9 m telescope. (*middle right*) HI velocity field with isovelocity contours derived from the low spatial resolution HI data. The isovelocity contours are spaced every 10  $\text{km s}^{-1}$ . (*bottom left*) *Spitzer* 3.6μm image with a high surface brightness stretch. (*bottom right*) Ellipse photometry results (see Sections 2.5 and 2.6) showing radial profiles of surface brightness,  $B - 3.6$  colour,  $B - R$  colour, and equivalent width (EW).